

Full wavefield migration: Seismic imaging using multiple scattering effects

Davydenko, Mikhail

DOI

[10.4233/uuid:1cda75d5-8998-49fe-997e-b38c9b7f8b8b](https://doi.org/10.4233/uuid:1cda75d5-8998-49fe-997e-b38c9b7f8b8b)

Publication date

2016

Document Version

Final published version

Citation (APA)

Davydenko, M. (2016). *Full wavefield migration: Seismic imaging using multiple scattering effects*. [Dissertation (TU Delft), Delft University of Technology]. <https://doi.org/10.4233/uuid:1cda75d5-8998-49fe-997e-b38c9b7f8b8b>

Important note

To cite this publication, please use the final published version (if applicable). Please check the document version above.

Copyright

Other than for strictly personal use, it is not permitted to download, forward or distribute the text or part of it, without the consent of the author(s) and/or copyright holder(s), unless the work is under an open content license such as Creative Commons.

Takedown policy

Please contact us and provide details if you believe this document breaches copyrights. We will remove access to the work immediately and investigate your claim.

Full wavefield migration: Seismic imaging using multiple scattering effects

PROEFSCHRIFT

ter verkrijging van de graad van doctor
aan de Technische Universiteit Delft,
op gezag van de Rector Magnificus prof. ir. K.C.A.M. Luyben,
voorzitter van het College voor Promoties,
in het openbaar te verdedigen
op DINSDAG 6 DECEMBER 2016 om 12:30 uur

door

Mikhail DAVYDENKO

Master of Science in de geologie
Staatsuniversiteit van Novosibirsk, Rusland
geboren te Novosibirsk, Sovjet-Unie

Dit proefschrift is goedgekeurd door de promotor:
Prof. dr. ir. L.J. van Vliet

en de copromotor:
Dr. ir. D.J. Verschuur

Samenstelling promotiecommissie:

Rector Magnificus,	voorzitter
Prof. dr. ir. L.J van Vliet,	promotor, Technische Universiteit Delft
Dr. ir. D.J. Verschuur,	copromotor, Technische Universiteit Delft

Onafhankelijke leden:

Prof. dr. ir. C.P.A. Wapenaar,	Technische Universiteit Delft
Prof. dr. ir. C.Vuik,	Technische Universiteit Delft
Prof. dr. S.A. Shapiro,	Freie Universitaet Berlin
Prof. dr. A. Ramirez,	Universidad Industrial de Santader
Dr. G. Eisenberg-Klein,	TEECware GmbH

ISBN 987-94-6186-768-1

Copyright ©2016, by M. Davydenko. All rights reserved. No part of this publication may be reproduced, stored in a retrieval system or transmitted in any form or by any means, electronic, mechanical, photocopying, recording or otherwise, without the prior written permission of the author.

SUPPORT

The research for this thesis was financially supported by the DELPHI consortium.

Typesetting system: L^AT_EX.

Printed in The Netherlands by Gildeprint.

*Посвящаю семье
To my family*

Contents

1	Introduction	1
1.1	Seismic imaging	1
1.2	Brief historical overview of seismic imaging	2
1.3	Imaging using surface and internal multiples	4
1.4	Closed-loop approach	8
1.5	Thesis objectives	10
1.6	Thesis outline	11
2	Forward model	13
2.1	Introduction	13
2.2	Notation	14
2.2.1	Propagation operator \mathbf{W}	15
2.2.2	Reflectivity operator \mathbf{R}	16
2.3	Wavefield relationship	18
2.4	Round trips	20
2.5	Numerical examples	21
2.5.1	Modelling of primaries and its internal multiples	21
2.5.2	Modelling of the total wavefield	25
2.5.3	Separate modelling of the surface multiples	26
2.5.4	Modelling of blended wavefields	27
2.6	Adjoint modelling	28
2.7	Discussion	30
2.8	Conclusions	32
3	Imaging	35
3.1	Introduction	35
3.2	Imaging and gradient computation	36
3.2.1	Gradient for upward reflectivity and transmission	38
3.2.2	Gradient for downward reflectivity and transmission	40
3.2.3	Remarks on parameter selection	41
3.3	Parameterisation	42
3.3.1	Angle-independent mode	42
3.3.2	Angle-dependent mode	43
3.4	Reflectivity updating	46
3.5	Scaling	46

3.6	Wavefield options in FWM	47
3.7	Numerical examples	48
3.7.1	FWM applied to total data	49
3.7.2	FWM applied to primaries and internal multiples	51
3.7.3	FWM applied to surface multiples only	53
3.7.4	Imaging of internal multiples with FWM	55
3.7.5	3D extension of FWM	56
3.8	Discussion	59
3.9	Conclusions	60
4	Omnidirectional extension	61
4.1	Omnidirectional modeling	62
4.2	Omnidirectional imaging	63
4.3	Examples	64
4.3.1	Dipping structure example	64
4.3.2	Vertical anomaly example	65
4.3.3	Duplex waves imaging by horizontal modeling	65
4.3.4	Salt model example	68
4.4	Discussion	68
4.5	Conclusions	69
5	Applications	71
5.1	Introduction	71
5.2	Imaging surface multiples	71
5.3	Joint primaries and surface multiples imaging	73
5.4	Ocean bottom node imaging	76
5.5	Source estimation	79
5.6	Interpolation using Full Wavefield Modelling	82
5.7	Separated primaries and multiples prediction	85
5.8	Deblending	86
5.9	Discussion	87
5.10	Conclusions	89
6	Field data examples	91
6.1	Introduction	91
6.2	Imaging of surface multiples	91
6.2.1	Deep water scenario	92
6.2.2	Shallow water scenario	94
6.2.3	3D ocean bottom node data	97
6.3	Impact of internal multiples	100
6.4	Pre-processing and events prediction	103
6.5	Discussion	104
6.6	Conclusions	105

7	Conclusions and Recommendations	107
7.1	Conclusions	107
7.2	Recommendations for further research	108
7.2.1	Using the estimated wavefields	108
7.2.2	More accurate and complete FWMod	109
7.2.3	Geometrical spreading in 2D FWM	109
7.2.4	Complex-valued angle-dependent reflectivity	109
7.2.5	Extension to 3D	110
7.2.6	Transmission effects	110
7.2.7	Elastic case and other effects	110
	Appendices	113
A	Practical observations	115
A.1	Model sampling	115
A.2	Transmission effects	116
A.3	Starting model	118
A.4	Complex-valued angle-dependent reflectivity estimation	120
B	Theoretical observations	123
B.1	Link with one-way wave equation	123
B.2	Including geometrical spreading	125
C	3D implementation	129
C.1	Propagation operators in 3D	131
C.2	Reflectivity operator	131
C.3	Numerical example	132
	Bibliography	137
	Summary	143
	Samenvatting	145
	Acknowledgements	147
	Curriculum Vitae	151
	Publications	153

1

Introduction

1.1 Seismic imaging

Seismic imaging plays a key role in the geophysical exploration for hydrocarbons. Reservoirs containing oil and gas might be located along very complex subsurface geological structures that should be revealed in the best possible way for further geological interpretation, geological model building, drilling and production. Due to the high production costs and risks there is an increasing demand on the quality of such information as a seismic image. Figure 1.1 shows as an example the complexity of such structures that can be observed in so-called outcrops. Different rock materials, characterised by different physical properties, can be easily distinguished

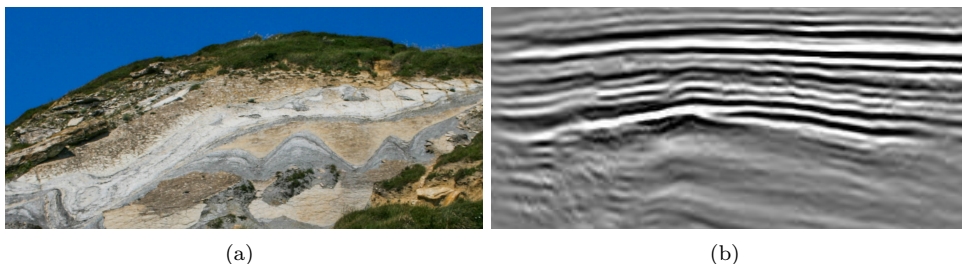


Figure 1.1: a) Example of geological structures observed in an outcrop. b) Example of a seismic image using the data obtained at the surface.

visually. To put it very simply, seismic imaging aims at almost taking a picture of the geological structures but located several hundred to thousands of meters beneath the surface.

In a seismic reflection experiment, acoustic impedance (propagation velocity times density) variations of the rock material causes a reflection of the incident signal that can be registered by an array of sensors, usually located at the surface. However, the measured signal that has to be translated to the image is very complex, because it contains a reflection response that is made up of various events. Figure 1.2 shows this classification in detail. Figure 1.2a depicts the total wavefield that occurs in the subsurface initiated by the source (shown as a red star). The **primaries** are shown in Figure 1.2b – those events occur due to a single scattering of the incident wavefield. Next, every primary event generates a sequence of **surface-related multiples** (shown in Figure 1.2c), which can be also referred to briefly as **surface multiples**. This happens when a primary reaches the surface that acts as a mirror. Every secondary source at the surface again generates a reflection at any of the subsurface reflectors. Note that surface multiples are also reflected at the surface and thereby generate a next order of scattering. Finally, Figure 1.2d depicts another type of events – **interbed** or **internal multiples**. These events are generated by the scattering that takes place at the lower side of each reflector inside the medium. Again, each downward reflected wave creates a sequence of events with reflectors below this downward scatterer and, after upward propagation, such waves can create a next order of internal multiples or surface multiples. Note that internal multiples can be generated not only also by primaries, but also by any of the surface-related multiples.

Over the years, only primaries (due to their simplicity) have been used in the seismic imaging algorithms. Therefore, all other events used to be considered as noise. In the next section a brief history on seismic imaging will be given.

1.2 Brief historical overview of seismic imaging

Seismic imaging algorithms have been evolving over almost a century since the first reflection seismic surveys appeared in the first decades of the 20th century. As mentioned in Bednar (2005) in the early days the "images" were purely interpreted by looking at the measured data. At some time, there were attempts to automate it by applying a kind of geometrical construction to the measured data (Robinson, 1958). Probably, Hagedoorn (1954) was the first who introduced the term migration as "the procedure of determining the true reflecting surface from a surface determined by a number of vertically plotted points".

Next, such geometrical approaches – using the Huygens' principle – led to Kirchhoff migration algorithms that operated in common mid points (between source and receivers) domain. After moveout correction CMP gathers were stacked and this result was transformed to the image domain using diffraction stacking. This approach can be referred to as a post-stack migration.

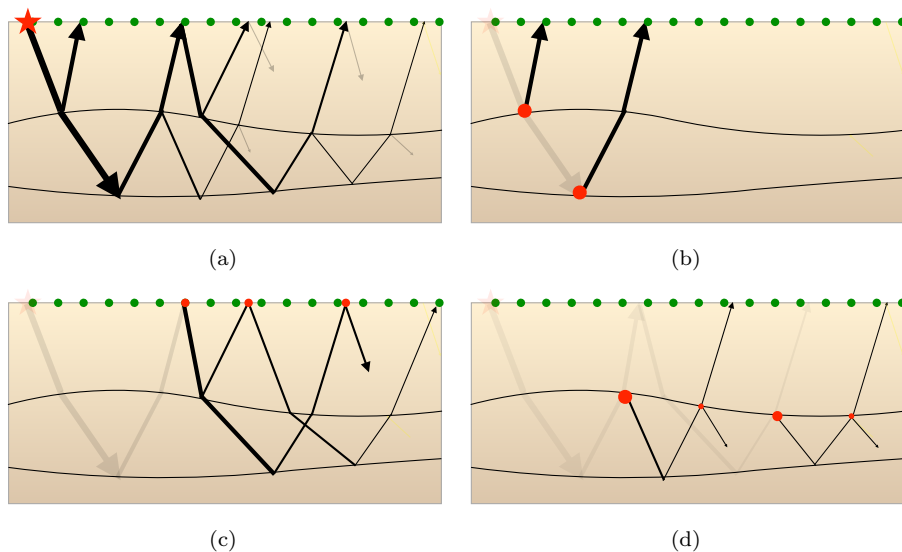


Figure 1.2: Events classification. (a) Total data, (b) primaries, (c) surface multiples and (d) internal multiples.)

The next major step was taken in the seventies – wave equation principles were introduced in seismic imaging by Claerbout (1971) and by Stolt (1978). At the same time magnetic tapes had been replaced by digital devices.

Another attribute of the "digital era" was applying the so-called pre-stack migration. Operating with pre-stack data allowed to consider complex velocity models with lateral and vertical variations and so-called depth migration algorithms appeared. The amplitudes were computed directly at the depth domain meaning that it already became an imaging procedure, rather than migration. Although the former is commonly used as a synonym to the latter. At the same time a new method has been introduced – Reverse-time migration – that involves the two-way wave equation for propagating wavefields and allowed to image steep dips (Baysal et al., 1983; Whitmore et al., 1983).

In the 1990's-2000's inversion-based imaging algorithms arose (Schuster et al., 1993; Nemeth et al., 1999; Wang and Sacchi, 2007) that allowed to improve the image quality, mainly in terms of resolution and signal to noise ratio (S/N). Nowadays we observe combinations of inversion-based imaging with full waveform inversion (FWI) – method that estimates elastic layer properties (density, velocities) using diving (refracted) waves - in order to perform reflection waveform inversion for layer properties jointly with the imaging process (Virieux and Operto, 2009; Wang et al., 2013; Staal et al., 2014).

Nevertheless, most of the imaging methods still do not distinguish between multiples and primaries, and every event is treated as a primary. Consequently, the

resulted images contain plenty of spurious reflectors (artefacts) that are also called crosstalk in the literature. The conventional approach to get the correct image is to separate primary reflections (i.e. eliminate multiples) and feed the imaging algorithm by the "correct" input, being only the primaries. Therefore, the algorithms that separate primaries (eliminate multiples) have been evolving as intense as imaging methods.

Elimination of surface multiples (Robinson, 1957; Berryhill and Kim, 1986; Verschuur et al., 1992; Verschuur and Berkhout, 1997; Weglein et al., 1997; Guitton and Cambois, 1999) and elimination of interbed multiples (Araujo et al., 1994; Jakubowicz, 1998; Berkhout and Verschuur, 2005) are done by separate methods. Surface multiples are usually more strong than internal multiples because they originate from the upgoing energy reflected at the strong and well-known reflector – the surface (see Figure 1.2c).

Internal multiples can be important when generated between strong reflectors located in the subsurface (see Figure 1.2d). Elimination of internal multiples is more difficult because the geometry of those multiples-generating structures is unknown.

Due to the fact that imaging condition (usually being either cross-correlation or deconvolution of the source-side and receiver-side wavefield) considers only one order of scattering, events of different scattering orders that match in time and space are considered as false primaries and, therefore, create false structures in the resulted image. Current multiple elimination algorithms allow to perform a good separation of primaries and surface multiples and, therefore, provide crosstalk free images using primaries. However, multiples are not noise in the sense that they do contain additional information about the subsurface. This will be more extensively discussed in the next section.

1.3 Imaging using surface and internal multiples

An appealing feature of multiples is that for a given single shot experiment, multiples increase illumination and therefore the area of the resulting image. It happens because strong reflectors in the medium serve in a way as additional sources that illuminate the subsurface via the multiple scattering. For a given source-receiver pair multiples will propagate at the surface at different (usually more vertical) angles that will also enhance the angle-coverage. The more vertical ray – due to the longer path of the multiple event – will increase vertical resolution. Moreover, for the same reason multiples also bring an extra sensitivity to velocity errors, which allows to use this fact for velocity estimation.

Note, however, that multiples are weaker than primaries and their information can be overshadowed by information from the latter. Therefore, multiples can be extremely useful in situations when there is lack of primary illumination – in the so-called shadow zones. For instance, in current acquisition designs, source sam-

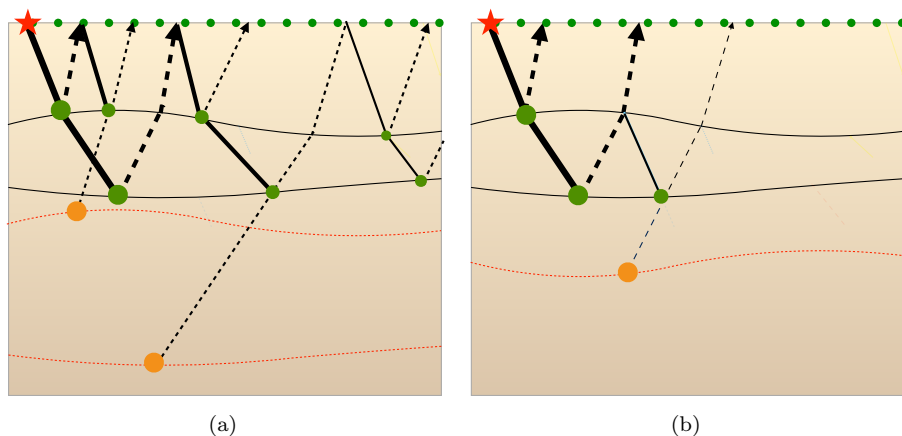


Figure 1.3: a) Using surface multiples in imaging. Note the extension of the illumination, as receivers act as additional sources (indicated by yellow dots). b) Reflectors also act as additional sources that generate internal multiples, thus providing additional illumination.

pling is usually coarser than receiver sampling, which especially applies for the cross-line direction, where source sampling can be 5-10 times coarser than that of receivers.

Over the last two decades efforts have been taken to perform imaging with incorporating surface multiples (Verschuur and Berkhout, 1994; Guitton, 2002; Brown and Guitton, 2005; Whitmore et al., 2010). One critical issue is the involved generation of crosstalk during imaging. This led to the development of methods that use inversion-based approaches in order to deal with crosstalk (Zhang and Schuster, 2013; Lu et al., 2014a; Wong et al., 2014; Tu and Herrmann, 2015). It has been shown that incorporating surface multiples tremendously extended illumination especially in the shallow shadow zones.

Only few works relate to using internal multiples in imaging (Malcolm et al., 2009; Fleury and Snieder, 2012; Brogгинi et al., 2013; Wapenaar et al., 2013). Comparison with those methods will be done later on in this thesis.

Figure 1.3 shows the advantage of using surface and internal multiples respectively. If the total measured data at the surface is re-injected as an additional source wavefield it can drastically increase the illumination when imaging is performed (Figure 1.3a). It also improves the resolution because the ray path of a surface multiple is usually more vertical than that of primaries for a given imaging point (Lu et al., 2014b). However, the deeper the imaging point the smaller the difference between the imaging of primaries and surface multiples. Therefore, at some depth angle coverage of surface multiples becomes very close to the angle coverage of primary illumination.

For deep locations, internal multiples become very interesting for imaging as they

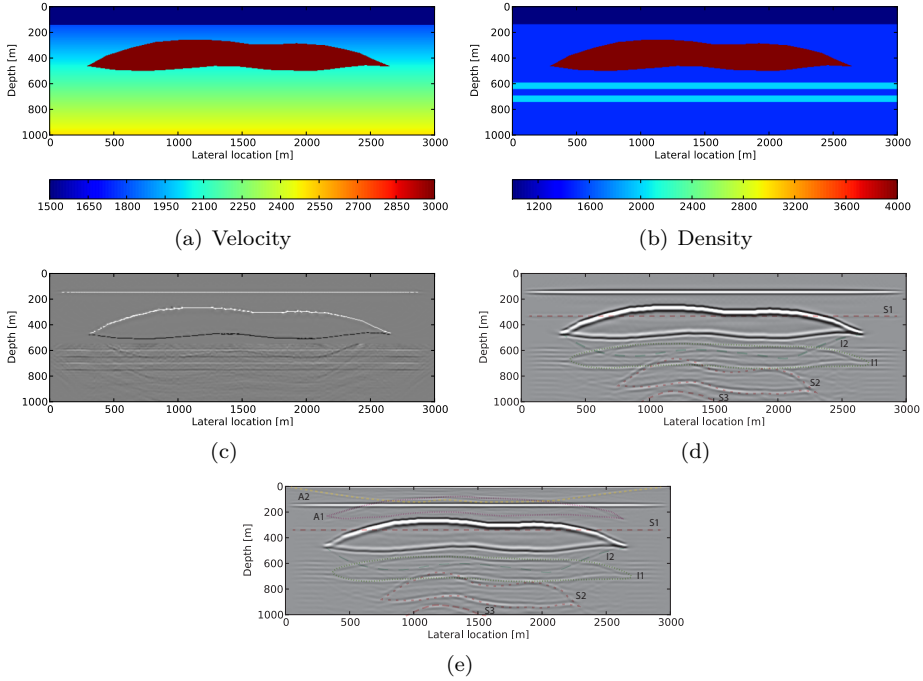


Figure 1.4: a) Velocity model. b) Density model. c) True reflectivity. d) Image when the wavelet was used as a source-side wavefield (Figure 1.5a). e) Image when the total data was used as a source-side wavefield (Figure 1.5b).

are generated inside the medium and yield illumination with parameters completely different from the (primary and secondary) sources at the surface. Figure 1.3b shows that every grid point in the subsurface serves as a potential secondary source that can generate internal multiples. In case primary illumination is lacking to image specific areas (shadow zones) the information coming from those secondary sources can also be used to enhance the illumination.

In most cases, a pre-stack shot record-based imaging algorithm can be described in three simple steps. The first step is based on extrapolating the source wavefield downwards through the subsurface and forward in time (schematically shown as a solid line in Figure 1.3). The second step is also based on extrapolating the wavefield, but received at the surface and propagating through the subsurface backward in time (shown as dashed lines in Figure 1.3). Finally, at every grid-point of the subsurface an imaging condition is applied. Usually, the imaging condition involves a linear operation with the source-side wavefield and the receiver-side wavefield at that grid-point. Such operation usually is a cross-correlation or deconvolution (Leveille et al., 2011). This procedure is basically an event matching (in space and in time) criterion at the imaging point: if events from both the source-side and the receiver-side wavefields coincide, then this point is a reflector. However, this criterion applies

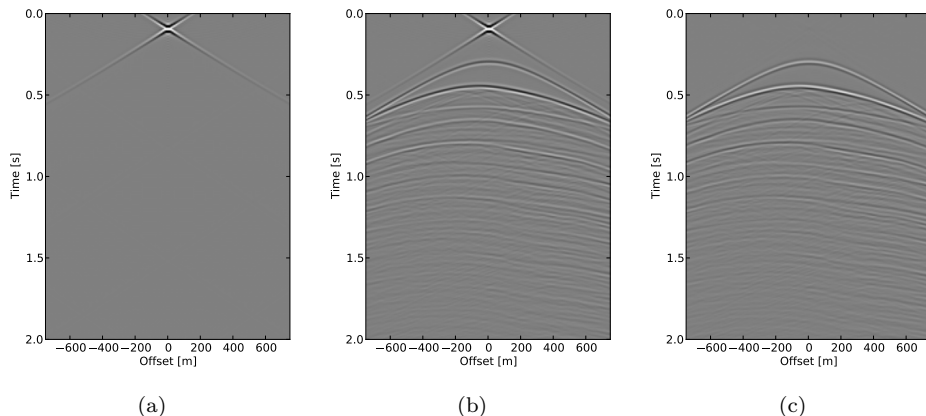


Figure 1.5: Source-sides: only source wavefield (a), source wavefield and re-injected measured data (b); Receiver-side: measured total data (c).

to events that are related to the same order of scattering. Matching of events with different order of scattering generates the cross talk. It is also indicated in Figure 1.3 – a back propagated multiple at some point can also match with a non-related event in the forward propagated source-side wavefield and, therefore, produce false matching criteria called **cross talk**, shown as an orange point. Hence, such points can create an entire false reflector (indicated by red dashed curves in Figure 1.3) that can be misinterpreted as a real geological structure.

As a brief example we consider the imaging of the data that comes from the velocity and density model shown in Figures 1.4a,b respectively. In this thesis this model will be extensively used in various examples. First, imaging is accomplished with a wavelet only as a source-side wavefield and the total data (including all multiples) as a receiver-side wavefield. Figure 1.4d shows the result of such imaging process. It contains a lot of spurious events: **S1** is crosstalk caused by imaging of the first-order surface multiple coming from the upper horizontal reflector, **I1** is crosstalk obtained via imaging of internal multiples generated in-between the high contrast layer, **I2** is crosstalk due to the imaging of an internal multiple generated between the horizontal boundary and the top of the anomaly, **S2** and **S3** are crosstalk from the first and the second-order multiples of the high velocity anomaly, respectively. Such crosstalk might be classified as causal, because lower-order scattering events at the source-side interfere with higher-order scattering events at the receiver-side. Causal crosstalk always appears deeper than the corresponding imaged primary event.

Next, the source-side wavefield is modified such that we can also image surface multiples (Figure 1.5b). Note that in this case the wavelet (shown separately in Figure 1.5a) allows to image the primaries whereas the measured total data (Figure 1.5c) is being re-injected (multiplied by -1) and allows to image the next order of

scattering – surface multiples. The result is shown in Figure 1.4e. It is visible that additional artefacts are created (**A1** and **A2**) if the image is obtained in the conventional way. Those artefacts are created due to surface multiples that appeared at the source-side and that are matching with the primaries or lower-order multiples at the receiver-side. Therefore, such crosstalk can be classified as anti-causal as the higher-order scattering events from the source-side interfere with the lower order of scattering at the receiver-side.

This simple example with three major reflectors already produces quite a number of crosstalk artifacts. For real data or complex numerical examples, such analysis becomes even more complex. In the next section an approach is discussed that allows to handle the crosstalk in an automatic way.

1.4 Closed-loop approach

In the previous section it was demonstrated that imaging of non-corresponding orders of scattering leads to the formation of artefacts in the image. One of the solutions that would come to mind is to separate orders of scattering and image them separately. However, that is not possible in a straightforward manner and also might be a computationally demanding task. In this section, it will be discussed how to resolve the crosstalk via an inversion approach.

Figure 1.6 shows the general block diagram of an inversion scheme that is already an accepted approach in solving various physical problems and was pioneered by Tarantola (1987). It can be characterised by the following common four steps:

1. **Data comparison:** In this step the modelled data are compared to the measured data. Various matching criteria might be applied such as minimum difference or maximum correlation.

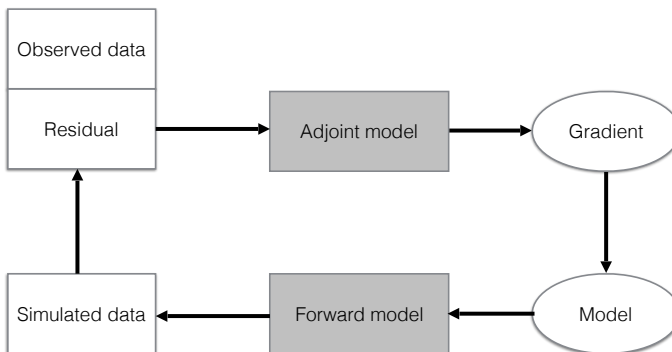


Figure 1.6: A general inversion scheme

2. **Adjoint of the forward model:** This process maps the residual in the data domain into the model domain and provides the model update. Note that this model update still needs to be scaled properly.
3. **Model update:** The model space is renewed by scaling the update calculated at the previous step and adding it to the current model. The involved scaling factor should be estimated.
4. **Forward operator:** The forward model calculates the new data from the updated model space such that it can be used for the next data comparison iteration.

Such procedure can be also seen as a closed-loop or feedback loop. It will suppress noise if the correct forward model is applied. For instance, blending noise can be resolved during migration for simultaneous shots if the correct source encoding is taken into account (Tang et al., 2009). In the same way, the crosstalk from multiples during imaging can be removed. Actually, multiple scattering might be even considered as natural blending (Verschuur and Berkhout, 2011). Therefore, in order to explain crosstalk from surface multiples it is necessary to include it in the forward model. The simplest way to include surface multiples is to re-inject the measured data at the surface with a negative sign.

Figure 1.7a shows the closed-loop procedure for a conventional inversion-based imaging approach, which is also known as least-squares migration. Its forward model basically uses the Born approximation, where at each grid point an incident wavefield is multiplied by the reflectivity at the same point and forward extrapolated to the surface. The superposition of these diffraction responses will produce the simulated primaries. This process is also called "de-migration" because it allows to recreate the data from the reflectivity estimated during the imaging process. The simulated data is again imaged, thereby producing an update for the reflectivity for the next iteration. The imaging condition is linear and uses the incident wavefield as a source-side wavefield and the

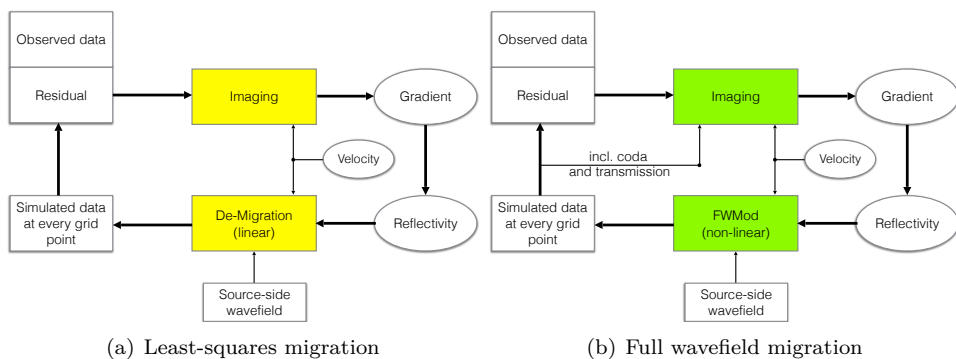


Figure 1.7: The general scheme of the PWM or least-squares migration (a) and FWM (b) inversion processes (i.e. closed-loop approaches).

back-propagated data residual as a receiver-side wavefield. Note, that this approach also allows to handle surface multiples by simply changing the source-side wavefield, as discussed above. The crosstalk caused by surface multiples can be sufficiently suppressed as the right physics describes the scattering at the surface. However, in the least-squares migration implementation internal multiples are not properly described. Therefore, the crosstalk caused by internal multiples will be updated as well as other real reflectors, in order to explain the data given the linear modelling. Therefore, this procedure will be referred to as a **Primary Wavefield Imaging (PWM)**, where the surface multiples are considered just as a complex incident ('primary') wavefield.

Figure 1.7b shows the aforementioned closed-loop process for the method being studied in this thesis – **Full Wavefield Migration (FWM)**. The main feature of FWM is its forward model – **Full Wavefield Modelling (FWMod)** – that generates the total reflection data (Berkhout, 2014a). In this case multiple scattering (surface-related and interbed) and also transmission effects are automatically included. Its forward model generates the total reflection wavefield driven by the same inputs as in PWM – estimated reflectivities (controlling the amplitudes of the simulated data) and a given migration velocity model that controls the phase of the modeled events. The modeled data is also compared with the observed data and the resulted residual is imaged again. Note that FWM uses a different source-side wavefield for the imaging condition – it uses the simulated wavefields provided by FWMod, which allows transmission effects and the internal multiple coda to contribute to the reflectivity estimation. Therefore, FWM not only suppresses the crosstalk but also uses the complex scattering effects in imaging. In fact, the reflectivity image shown in Figure 1.4c is the result of FWM, as we will see later in this thesis.

1.5 Thesis objectives

This study aims at developing an imaging algorithm that:

- **Provides a true-amplitude, angle-dependent reflection coefficient image:**

The imaging will benefit from the inversion-based approach. Moreover, its forward model will be based on a realistic forward model that takes into account effects as transmission and (interbed and surface-related) multiple reflections.

- **Takes all multiples into the account:**

Including of correct physics will result into the suppression of the cross-talk caused by multiples.

- **Uses multiples to illuminate shadow zones**

The aim is not only removing the crosstalk from multiples, but using the additional information from multiples in order to recover areas weakly illuminated

by primaries.

- **Is suitable within current acquisition geometries**

The algorithm should be suitable for coarse source (or receiver) sampling. Such requirement is very important for current three-dimensional surveys.

- **Does not require ‘multiple generators’ to be provided in advance**

Internal multiples generating boundaries are not pre-defined in advance as a-priori information (model-driven), but automatically incorporated from the imaged reflectivity (data-driven).

1.6 Thesis outline

In this section a further outline of this thesis is given.

Chapter 2:

This chapter describes the forward model (Full Wavefield Modelling) that is used in the proposed methodology. Firstly, the reflectivity and propagation operators used in the modelling are described followed by the wavefield relationships forming the basis of the modelling scheme. Next, the main principles of generating the scattering are described by introducing the so-called roundtrip. Various numerical examples demonstrate modelling of primaries and their internal multiples, as well as surface multiples. At the end it is briefly shown how it is possible to use this scheme in the adjoint mode, as an introduction to the following chapters.

Chapter 3:

This chapter focuses on the imaging block and the inversion aspects of the proposed algorithm. Some derivations show that the gradient computation in (steepest) descent methods is basically a process of data-misfit imaging. Next, it is shown that parameters from the resulting gradient can be extracted in different ways. Two main parameterisations are introduced: structural and angle-dependent. The first one characterises the subsurface grid-point by one angle-independent scalar (aiming at estimating the structural image), whereas the latter describes each subsurface grid-point by an angle-dependent vector of parameters, and therefore angle gathers are estimated. Next, it is shown that imaging can be performed by two imaging conditions: from above and from below. The second option is interesting, because it exploits information coming directly from internal multiples. Various numerical examples demonstrate the FWM process, with specific focus on effective cross-talk suppression.

Chapter 4:

This chapter investigates a possibility to extend the FWM method such that imaging steep dips can be handled. The involved propagation operator (discussed in the previous chapter) is based on the one-way wave equation and, therefore, it has a preferred direction (depth) and hence horizontal propagation is limited. As a result, imaging of the boundaries close to the vertical (orthogonal to the preferred wavefield continuation direction) becomes very difficult. In this chapter we perform modelling and imaging not only in vertical depth directions, but additionally operate in the horizontal direction. Horizontal reflectivity parameters are introduced. Numerical examples demonstrate the potential of this omnidirectional imaging approach.

Chapter 5:

Various extensions of the FWM methodology are described in this chapter. Firstly, advantages and disadvantages of different imaging options (total data, separated primaries and separated surface multiples) are discussed. Then, the joint imaging of separated primaries and separated multiples is introduced. This allows to take the best of each approach individually and avoid their downsides. Next, the specific case of imaging ocean bottom node data is introduced (based on the surface multiples imaging). It is also shown how the source wavelet required for imaging primaries can be estimated from imaging surface multiples. Next, the 3D implementation of the method is discussed. After that it is shown that the output of the forward model can be used for missing data reconstruction that, again, can be used for a next application of FWM, thus providing a better image. After that it is shown that the output of the modelling tool can also be used for prediction of multiples as well as de-blending simultaneous source data.

Chapter 6:

In this chapter the application of FWM on several marine field datasets is demonstrated. Most of the aspects discussed in the previous chapters are verified on both 2D field and 3D field data.

Chapter 7:

In this chapter the main conclusions of this thesis are described, followed by some discussions and recommendations for further research.

2

Forward model

2.1 Introduction

As was discussed earlier, the choice of forward model is one of the main components of any closed-loop procedure. It is used to generate the data that is compared with the observed one in order to calculate the residual for the next iteration of the inversion. The main idea of the forward model of FWM - full wavefield modeling (FWMod) - is based on generating the data by a data-driven approach (Berkhout, 2014a). The observed seismic data is a result of the impedance variations (product of density and propagation velocity) that occur in the subsurface. Hence, FWMod attempts to model the total data, and thereby explain the measured one, with reflectivity-driven scattering. Thus, the scattering is generated only from the reflectivity (seismic image) whereas the propagation effects are controlled by a given migration velocity model. In this case, the reflectivity controls mainly the amplitude of the reflection event whereas the phase is separately controlled by the velocity model. Such approach is also very beneficial for simultaneous estimation of reflectivity and velocity and allows to avoid local minima during the inversion (the so-called Joint Migration Inversion or JMI process, see Berkhout (2014c)). However, in this thesis we will restrict ourselves to the estimation of reflectivity only. In this section the main aspects of the FWMod will be described, illustrated by various examples.

2.2 Notation

This section briefly introduces the notation used in this thesis. It mainly follows the matrix notation from Berkhout (1982).

In this notation the subsurface is considered to be located on a rectangular grid. The monochromatic component of the pressure wavefield registered at any j^{th} grid-point at any depth level z_m and emitted at depth level z_n by the k^{th} source can be written as $P_{jk}(z_m, z_n)$. The wavefield at a depth level is described as a column-vector $\vec{P}(z_m, z_n)$, the elements of which contain monochromatic values of the wavefield at the grid-points belonging to that level. In the case of a multi-shot experiment, the matrix $\mathbf{P}(z_m, z_n)$ is formed by combining the introduced column-vectors for all sources. Note that for the sake of simplification, the source-depth level might not be indicated, assuming that the source is located at the surface (unless a different location is specified).

Various operations might be applied to the shot-experiments. In this thesis propagation operator \mathbf{W} and reflection operator \mathbf{R} will be commonly used. The one-way propagation operator $\mathbf{W}(z_m, z_n)$ extrapolates the wavefield from depth level z_n to depth level z_m . Finally, reflectivity operator $\mathbf{R}(z_n)$ is applied to the wavefield in order to simulate reflection at arbitrary depth level z_n .

Although the 2D matrix notation is described as a default, the method works equally well for the 3D case, where a similar matrix notation can be used. It means that one column vector now contains concatenation of the wavefield values along a two-dimensional grid of (x, y) values. Thus, a shot record is still represented by a column vector and operators are still matrices. For a more thorough explanation of the 3D matrix notation, the reader is referred to Kinnegeing et al. (1989).

Table 2.1 collects the aforementioned objects that will be used in this thesis. The so-called **WRW** notation describes the propagation and reflection of seismic data. It was proposed by Berkhout (1982). The concept has been initially proposed for

Table 2.1: Matrix notation.

Indices:

\hat{j}	grid-point index
k	shot-record index

Wavefields:

P_{jk}	wavefield from shot k at the current grid-point
$\vec{P}_k(z_m)$	wavefield from shot k at the current depth-level
$\mathbf{P}(z_m)$	wavefields from many shots at that depth-level
$*^{+,-}$	wavefield direction ('+' is downgoing, '-' is upgoing)

Operators:

$\mathbf{R}(z_m)$	reflectivity matrix
$\mathbf{W}(z_m, z_n)$	one-way propagation operator

primaries. Therefore, primary reflection data (neglecting the transmission effects) can be written as:

$$\mathbf{P}^-(z_0) = \sum_{n>0} \mathbf{W}^-(z_0, z_n) \mathbf{R}(z_n) \mathbf{W}^+(z_n, z_0) \mathbf{S}^+(z_0). \quad (2.1)$$

Equation 2.1 basically says that the primary data at the surface is a superposition of the following round-trip: the source wavefield $\mathbf{S}(z_0)$ at the surface is propagated downwards via $\mathbf{W}^+(z_n, z_0)$ to the arbitrary depth level z_n , reflected there with the aid of the reflectivity operator $\mathbf{R}(z_n)$ and forward propagated upwards by operator $\mathbf{W}^-(z_0, z_n)$ to the surface depth level z_0 .

In the following subsections the propagation and reflectivity operators will be further explained.

2.2.1 Propagation operator \mathbf{W}

Propagation is described by the $\mathbf{W}^\pm(z_m, z_n)$ operator from horizontal depth level z_n to depth level z_m . The sign \pm indicates the propagation direction ('+' for downgoing and '-' for upgoing). For laterally inhomogeneous media the wavefield extrapolation in the wavenumber-frequency domain is described by a phase-shift:

$$P(k_x, z_n + \Delta z) = P(k_x, z_n) \exp(ik_z \Delta z), \quad (2.2)$$

where Δz is the difference between z_m and z_n . In the space-frequency domain Equation 2.2 is represented by a spatial convolution that can be described by a convolution operator W :

$$P(x, z_n + \Delta z) = \int P(x - h, z_n) W(h) dh, \quad (2.3)$$

where $W(h)$ is a Fourier-transformed version of the exponential term in Equation 2.2 and h represents a spatial lag or local offset.

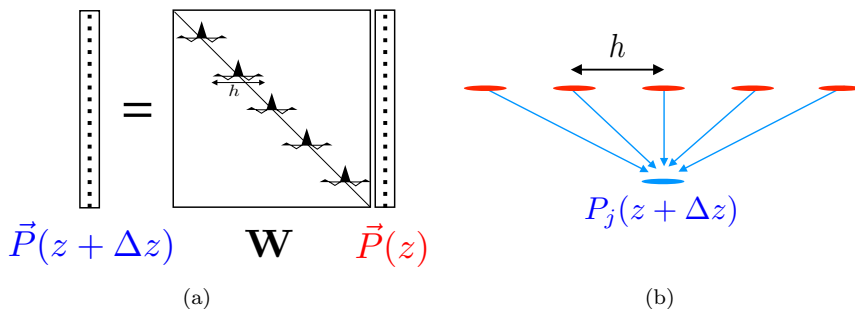


Figure 2.1: Propagation operator.

In the discrete form the integral becomes a discrete summation (see Figure 2.1b) and it can be written as a vector inner product:

$$P_j(z_m) = [\vec{W}(z_m, z_n)]^T \vec{P}(z_n). \quad (2.4)$$

For all locations j of the depth level z_m this becomes (see Figure 2.1a):

$$\vec{P}(z_m) = \mathbf{W}(z_m, z_n) \vec{P}(z_n). \quad (2.5)$$

In case of lateral inhomogeneities, the \mathbf{W} has no longer a Toeplitz structure, but every row contains a local convolution operator. Usually, we make the assumption of a local homogeneous medium within some area (i.e. the operator length) around each lateral location, because then we can easily calculate this operator from the phase shift-operator in the wavenumber domain by a spatial Fourier transform. The shorter this operator, the more accurate lateral inhomogeneities can be handled. However, short operators might create numerical errors during the propagation. An elegant way to optimize such short operator is discussed in Thorbecke et al. (2004). Moreover, these propagation operator can also be extended for the anisotropic case (Zhang and Wapenaar, 2002; Alshuhail et al., 2014) and may also contain attenuation effects.

Note that there are also different ways to arrive at such one-way wavefield propagation. An alternative approach to handle lateral inhomogeneities would be extrapolation using a selection of homogeneous reference velocities followed by interpolation of the result at each location depending on the local velocity. Such approach is called phase-shift-plus-interpolation (PSPI) (Gazdag and Sguazzero, 1984). It can be more applicable for 3D problem, as for that case the convolution operator becomes two dimensional for each frequency, which also increases computational costs, while PSPI might be more efficient.

2.2.2 Reflectivity operator \mathbf{R}

This section introduces the reflectivity operator that describes reflection of the wavefields. Basically, the reflectivity operator $\mathbf{R}(z_m)$ connects the reflected wavefields $\vec{P}^\pm(z_m \pm \epsilon)$ and the incident ones $\vec{P}^\pm(z_m \mp \epsilon)$:

$$\begin{aligned} \vec{P}^-(z_m - \epsilon) &= \mathbf{R}^\cup(z_m) \vec{P}^+(z_m - \epsilon) \\ \vec{P}^+(z_m + \epsilon) &= \mathbf{R}^\cap(z_m) \vec{P}^-(z_m + \epsilon), \end{aligned} \quad (2.6)$$

where ϵ is a small number indicating whether the wavefields are considered either above or below the depth level z_m and superscripts \cup and \cap of the reflectivity operator stand for the case of upward or downward reflection respectively. Note that in the remainder of this thesis we will omit the epsilon in our wavefield notation. Furthermore, note that \vec{P}^+ refers to downgoing wavefield and \vec{P}^- denotes upgoing wavefields (see also Table 2.1).

Figure 2.2a shows the structure of the reflectivity matrix. In analogy to the propagation operator \mathbf{W} , in the case of homogeneous horizontal reflector, this operator

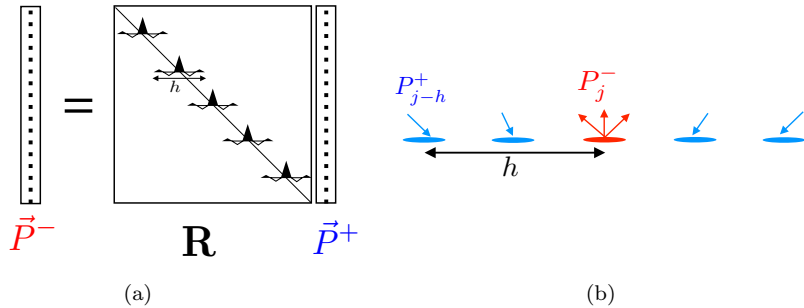


Figure 2.2: Reflectivity operator.

also represents a stationary convolution process. However, if lateral variations are present, we change the rows of this matrix according to the lateral reflectivity values. Therefore, the reflected wavefield at spatial gridpoint j at depth level z_m (let's say P_j^-) is a sum of multiplications of the downgoing wavefield P_{j-h}^+ at the $(j-h)^{th}$ location with the reflectivity function $R(h)$ as a function of the local offset h (or lateral lag). Such convolutional operation is identical to multiplication of the j^{th} row of the reflectivity matrix with the data column-vector \vec{P}^+ (see Figure 2.2b).

This spatial lag links the angle of reflection and it's amplitude. In this thesis we consider two different descriptions of the reflectivity: angle-independent and angle-dependent. In the first approach only the zero lag during reflection is considered. It means that the reflectivity matrix has a diagonal structure and matrix multiplication, therefore, means simple scaling of the wavefield P_j^+ (at every location j) by the reflectivity at this point R_j . Thus, this approach does not simulate amplitude versus offset (AVO) variations in the resulted reflection data (except for geometrical spreading effects). The more complex approach involves angle-dependent parameterisation. Rows of the reflectivity matrix contain reflection coefficients that serve as weights. The weighted sum calculates the wavefield at the certain point not only using the reflection of the incident wavefield at this point but also including the contribution from various grid points around the considered one. Figure 2.2a illustrates this approach. If the angle-dependent reflectivity operator is transformed to the wavenumber domain, the angle-dependent reflection coefficients are obtained. From that point of view the angle-independent description via a spike in the spatial domain corresponds in the wavenumber domain to a constant reflection coefficient for each angle. For more information about angle-dependent reflectivity the reader is referred to de Bruin et al. (1990); Berkhout (1997).

2.3 Wavefield relationship

The forward model of our wavefields considers a regularly gridded volume of the subsurface (Figure 2.3a). By taking one horizontal slice the depth level z_m is selected (Figure 2.3b). Each depth level contains grid-points with arbitrary index j (Figure 2.3c).

At every subsurface grid-point the full wavefield relationship is considered. As it is shown in Figure 2.4, every depth level z_m (set of all grid-points belonging to that level) can be illuminated from above by downgoing wavefield $\vec{P}^+(z_m)$ and from below by upgoing wavefield $\vec{P}^-(z_m)$ all related to one specific physical experiment. At the same time the total wavefields \vec{Q}^\pm leave this depth level in both directions and include the potential scattering.

Following Berkhout (2014a), the total outgoing wavefield can be represented as a sum of the transmitted (by the \mathbf{T} operator) incoming wavefield in the same propagation direction and the reflected (by the \mathbf{R} operator) wavefield coming from the opposite direction:

$$\begin{aligned}\vec{Q}^+(z_m) &= \mathbf{T}^+(z_m)\vec{P}^+(z_m) + \mathbf{R}^\cap(z_m)\vec{P}^-(z_m) \\ \vec{Q}^-(z_m) &= \mathbf{T}^-(z_m)\vec{P}^-(z_m) + \mathbf{R}^\cup(z_m)\vec{P}^+(z_m),\end{aligned}\quad (2.7)$$

where \mathbf{T}^\pm can be represented as sum of unity matrix \mathbf{I} and additional term $\delta\mathbf{T}^\pm$ ($\mathbf{T}^\pm = \mathbf{I} + \delta\mathbf{T}^\pm$):

$$\begin{aligned}\vec{Q}^+(z_m) &= \vec{P}^+(z_m) + \delta\mathbf{T}^+(z_m)\vec{P}^+(z_m) + \mathbf{R}^\cap(z_m)\vec{P}^-(z_m) \\ \vec{Q}^-(z_m) &= \vec{P}^-(z_m) + \mathbf{R}^\cup(z_m)\vec{P}^+(z_m) + \delta\mathbf{T}^-(z_m)\vec{P}^-(z_m).\end{aligned}\quad (2.8)$$

The two additional extra terms can be considered as secondary sources:

$$\begin{aligned}\delta\vec{S}^+(z_m) &= \delta\mathbf{T}^+(z_m)\vec{P}^+(z_m) + \mathbf{R}^\cap(z_m)\vec{P}^-(z_m) \\ \delta\vec{S}^-(z_m) &= \mathbf{R}^\cup(z_m)\vec{P}^+(z_m) + \delta\mathbf{T}^-(z_m)\vec{P}^-(z_m).\end{aligned}\quad (2.9)$$

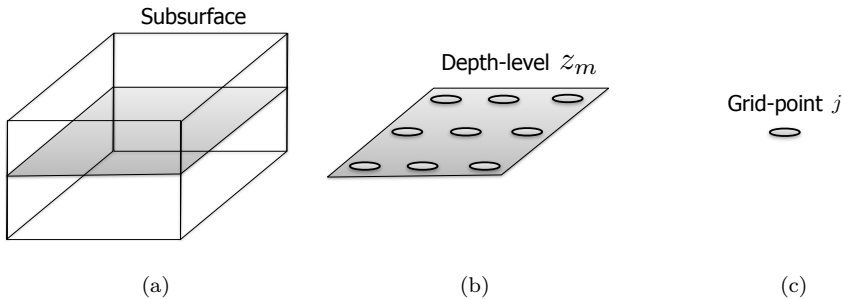


Figure 2.3: Subsurface definitions in FWMod.

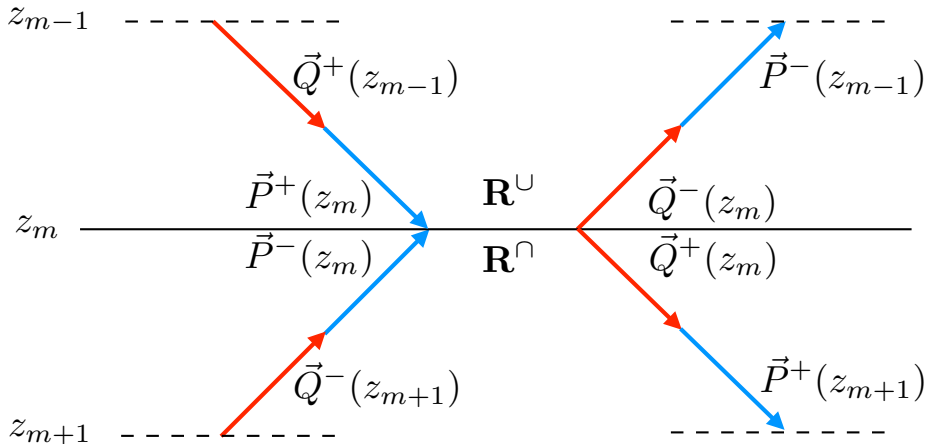


Figure 2.4: Full wavefield relationship at depth level z_m .

Thus, we have the relationships:

$$\begin{aligned}\vec{Q}^+(z_m) &= \vec{P}^+(z_m) + \delta\vec{S}^+(z_m) \\ \vec{Q}^-(z_m) &= \vec{P}^-(z_m) + \delta\vec{S}^-(z_m).\end{aligned}\quad (2.10)$$

If we assume small contrasts for shear wave propagation velocity, $\delta\mathbf{T}^+$ and $\delta\mathbf{T}^-$ can be approximated as \mathbf{R}^U and \mathbf{R}^N respectively, and Equations 2.8 are transformed to:

$$\vec{Q}^\pm(z_m) = \vec{P}^\pm(z_m) + \delta\vec{S}(z_m), \quad (2.11)$$

where:

$$\delta\vec{S}(z_m) = \mathbf{R}^U(z_m)\vec{P}^+(z_m) + \mathbf{R}^N(z_m)\vec{P}^-(z_m) \quad (2.12)$$

is a two-way secondary source field.

The second wavefield relationship (Figure 2.4) says that after propagation, the total outgoing wavefields \vec{Q}^\pm become approaching wavefields at the neighboring depth level $z_{m\pm 1}$:

$$\begin{aligned}\vec{P}^+(z_{m+1}) &= \mathbf{W}^+(z_{m+1}, z_m)\vec{Q}^+(z_m) \\ \vec{P}^-(z_{m-1}) &= \mathbf{W}^-(z_{m-1}, z_m)\vec{Q}^-(z_m),\end{aligned}\quad (2.13)$$

where $\mathbf{W}^\pm(z_{m\pm 1}, z_m)$ is a propagation operator from depth level z_m to the neighboring depth level $z_{m\pm 1}$. As mentioned in Section 2.2.1 for each frequency slice applying this operator can be considered as a spatial convolution with local phase-shift operators (also including lateral variations). As mentioned before, \mathbf{W}^\pm may also include attenuation effects as well as anisotropic propagation behaviour.

Note that the above description is not limited to purely acoustic wave propagation, but describes the P-wave reflection events in an elastic medium. The reflectivity operators contains the elastic R_{pp} , although Equations 2.11 and 2.12 are then

approximations. In principle the forward model can also be extended to include converted waves (see also Berkhout (2014a)). Some further remarks on this can be found in Chapter 7.

2.4 Round trips

By looking at Equations 2.11 and 2.12 we see that these equations are interdependent: computation of the wavefield (Equation 2.11) requires the scattering term (Equation 2.12), while the scattering term is also a function of the modeled wavefields. Therefore, the modeling is done in a recursive manner. Usually, we start with the wavefield at the surface that may include the source wavelet and/or the re-injected reflection data to simulate surface multiples as well as any combination with simultaneous/blended sources. This wavefield is extrapolated downwards with accumulation of all secondary sources and also possible physical sources:

$$\vec{P}^+(z_m) = \sum_{n < m} \mathbf{W}(z_m, z_n) [\vec{S}^+(z_n) + \delta \vec{S}(z_n)]. \quad (2.14)$$

Therefore, after calculations via Equation 2.14, the incident field with transmission effects included, is computed. Then, this downgoing wavefield can be substituted into Equation 2.12 to update the scattering term. Next, the upgoing wavefield can be computed in a similar manner:

$$\vec{P}^-(z_m) = \sum_{n > m} \mathbf{W}(z_m, z_n) [\vec{S}^-(z_n) + \delta \vec{S}(z_n)]. \quad (2.15)$$

In these equations $\vec{S}^+(z_n)$ and $\vec{S}^-(z_n)$ represent possible physical source fields at level z_n . For traditional surface data, all $\vec{S}^\pm(z_n)$ are zero except $\vec{S}^+(z_0)$. In that case the data modeled at the surface is an upgoing wavefield that can be written as follows:

$$\vec{P}^-(z_0) = \sum_{n > 0} \mathbf{W}(z_0, z_n) \delta \vec{S}(z_n). \quad (2.16)$$

After one iteration, the resulting upgoing wavefields include the primary reflections. Next, if the scattering term is updated by the upgoing wavefield via Equation 2.15, the new modeled downgoing wavefield by Equation 2.14 will contain not only the incident wavefield but also first-order downgoing multiples. Therefore, each round-trip – meaning applying Equations 2.14 and 2.15 and substituting the results into Equation 2.12 – will add a new order of multiple scattering. This process is schematically illustrated in Figure 2.5.

Note that this way of recursively modeling wavefields is similar to the Bremmer series (Bremmer, 1951; Gray, 1983; de Hoop et al., 2000). Coupling of Equations 2.11 and 2.12 shows similarities to the generalized Bremmer series (Corones, 1975; Wapenaar, 1996).

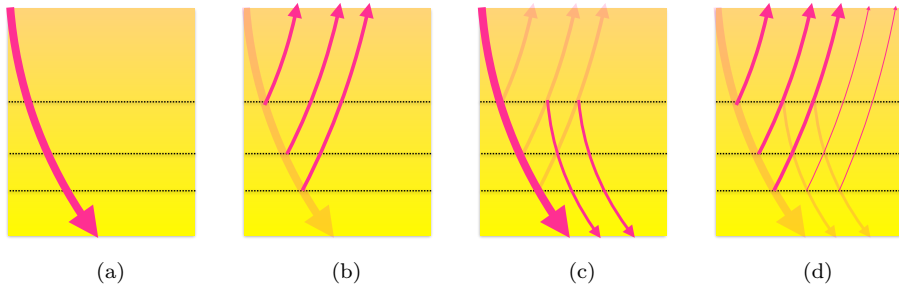


Figure 2.5: Illustration of how Bremmer series work. a) Firstly, the downgoing wavefield is computed. b) Next, an upgoing wavefield is constructed as a reflected incident wavefield using (a). c) Next, a new version of downgoing wavefield is computed using (a) and (b). d) Then, upgoing wavefield is updated basing on (b) and (c)

2.5 Numerical examples

The following numerical examples will demonstrate FWMod and compare it with finite-difference modelling. It will be shown that the method is able to model various datasets depending on the source-side wavefield: primaries and/or surface multiples or any blended shot-records.

2.5.1 Modelling of primaries and its internal multiples

Figure 2.6 demonstrates comparison of finite-difference modelling with FWMod based on a realistic self-estimated reflectivity model (FWM image). The finite-difference modeling solves the two-way acoustic wave equation by approximation of partial derivatives by differences of the wavefield at neighboring grid-points (Carcione et al., 2002). Therefore, the velocity and density models (Figures 2.6a,b respectively) are required to perform the modeling. All reflections will be generated by sharp variations of the velocity and/or the density (impedance variation). In the case of seismic imaging, the actual velocity model is not always known and an approximated model (the migration or macro velocity model) is used that usually contains the smoothed variations of the medium. The FWM modeling tool (FWMod) allows to generate the scattering by using the macro model (Figure 2.6d) and reflectivity distribution of the subsurface (i.e. the estimated image, see Figure 2.6e). Next, the iterative wavefield construction is shown. Note that the data contains all transmission effects and all kinds of multiples: Figures 2.6 f-i show the two-way wavefield (sum of two one-way upgoing and downgoing wavefields) constructed from the first and the second iteration respectively: the wavefield is constructed iteration by iteration, where every iteration contributes an additional order of scattering. Note that transmission effects are automatically included as well. Figure 2.7 shows the modelling from the zero-offset pseudo VSP point of view where at $x=1500\text{m}$ the wavefield is extracted at all depth levels. It is clearly visible how internal multiples

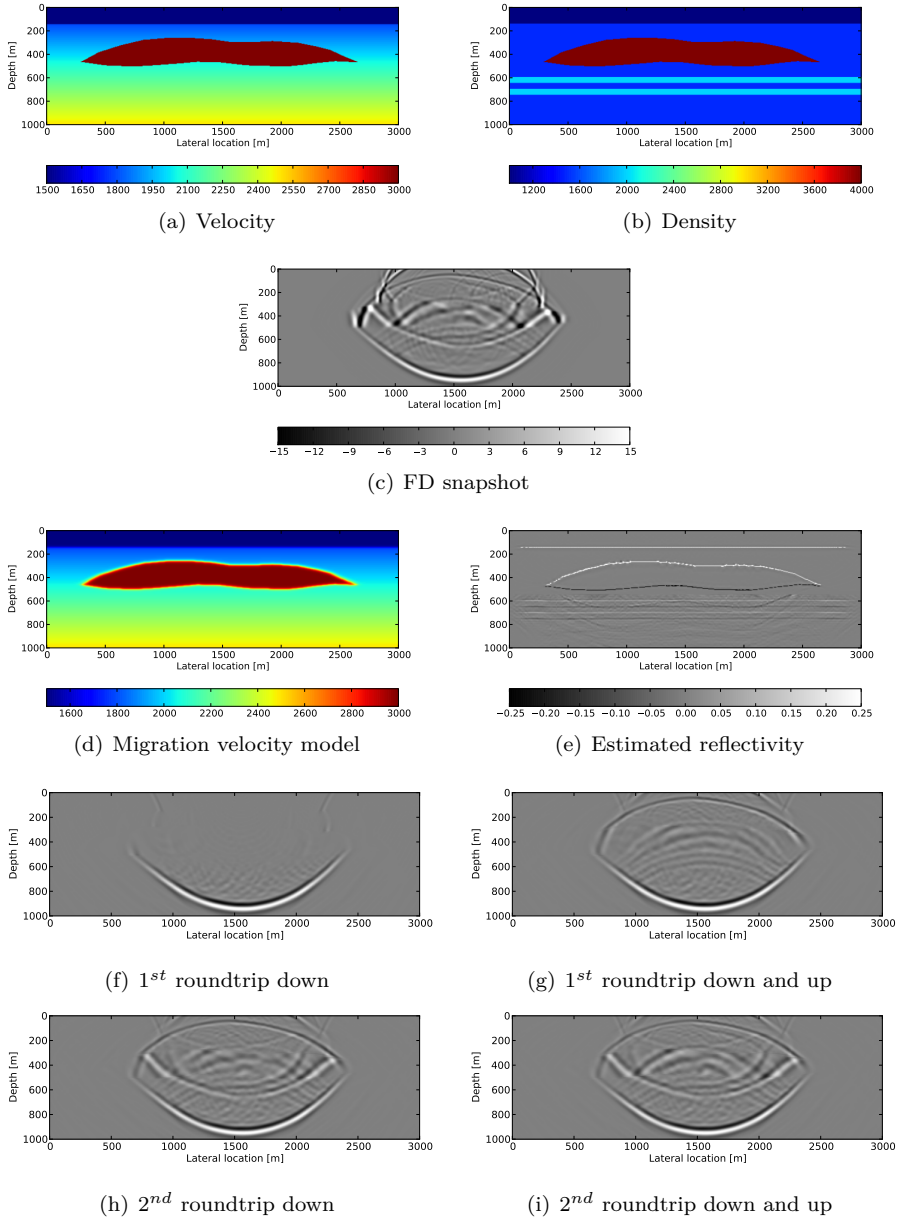


Figure 2.6: Comparison of finite-difference modelling (FD) and full wavefield modelling (FWM). a) Velocity model; b) Density model containing weak reflectors located below the salt body; c) Two-way wavefield obtained by finite-difference modelling; d) Migration velocity model; e) Reflectivity model estimated by FWM; f-i) Total (upgoing + downgoing) FWM wavefields at the first and second modelling iterations, respectively.

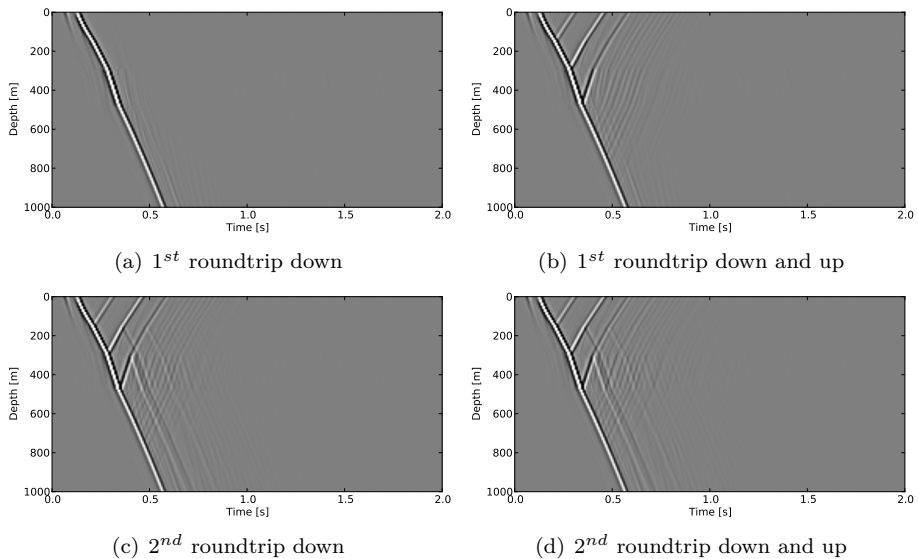


Figure 2.7: Pseudo VSP zero-offset section extracted at $x = 1500\text{m}$ during FWMod. a) 1st iteration down only; b) 1st iteration down and up; c) 2nd iteration down only; d) 2nd iteration down and up.

are generated mostly within the salt body and the water bottom horizon (the first horizontal reflector) and the wavefield becomes more complex after each modelling step. Figure 2.8 shows how orders of multiples are also accumulated at the surface as an upgoing wavefield. The complex upgoing wavefield at the surface is also very important as it is used in the inversion as the difference between modeled and the observed wavefield, which should be minimized. Figure 2.9 shows the downgoing wavefield at one of the last depth levels of the subsurface. It also visible that the illuminating wavefield becomes more complex due to the coda of all multiples. Note, that conventional imaging does not take into the account internal multiples and transmission effects and, therefore, the downgoing wavefield that is used in such migration process will be similar to the result of FWMod at the first iteration.

However, modeling using the reflectivity close to normal incidence for angle-independent modelling can not be accurate in terms of AVO. Figure 2.10a shows the surface data computed by the finite-difference algorithm. Data modeled by the angle-independent FWM approach and angle-dependent FWM approach are shown in Figures 2.10b,c, respectively. Figure 2.10d shows the difference between the finite-difference data and the data modeled by angle-independent FWMod. Figure 2.10e shows a much smaller different in a case of angle-dependent FWMod.

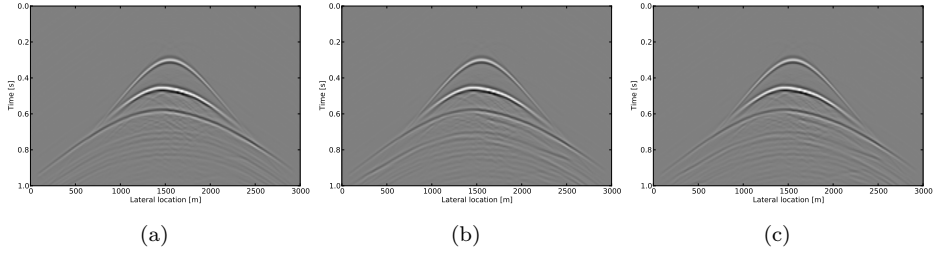


Figure 2.8: Upgoing wavefield at the surface depth level, modeled after: a) first iteration; b) second iteration; c) third iteration.

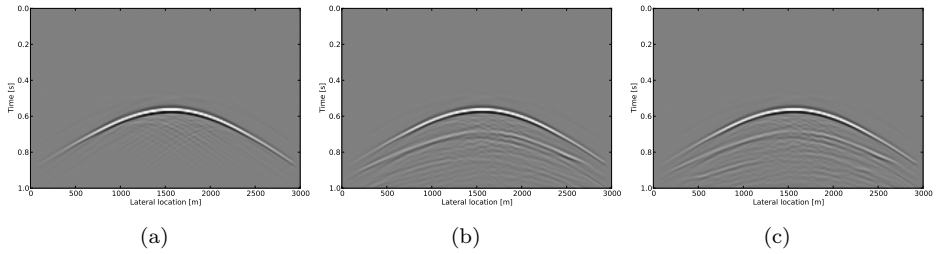


Figure 2.9: Downgoing wavefield modeled at depth level 950m after the: a) first iteration; b) second iteration; c) third iteration.

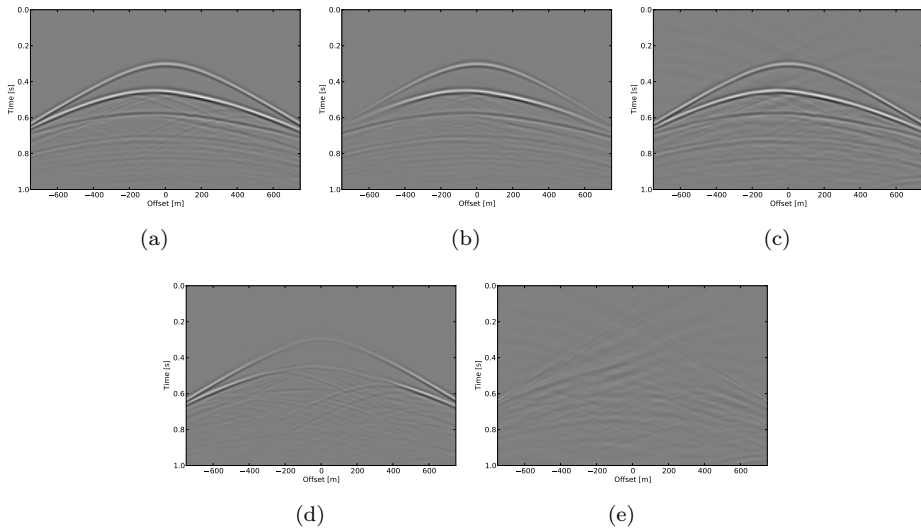


Figure 2.10: Comparison of angle-independent and angle-dependent version of FWMod. a) Finite-difference modelled data; b) Angle-independent FWMod; c) Angle-dependent FWMod; d) Difference between a) and b); e) Difference between a) and c).

2.5.2 Modelling of the total wavefield

Modelling of the 'total wavefield' refers to simulating all reflection events including surface multiples and their internal multiples in addition to the previous experiments. Adding of surface multiples can be done in two ways. In the first way we address the free-surface boundary condition by representing the total downgoing wavefield at the surface as:

$$\vec{Q}^+(z_0) = \vec{S}^+(z_0) + \mathbf{R}^\cap(z_0)\vec{P}_{obs}^-(z_0), \quad (2.17)$$

where \mathbf{R}^\cap is a free-surface reflectivity and $\vec{P}_{obs}^-(z_0)$ is an observed total reflection wavefield. Since Equation 2.17 is applied, the reflectivity at the surface in FWMod is set as zero.

The second way to model surface multiples is to set $\mathbf{R}^\cap(z_0)$ as a free surface reflectivity operator and to calculate the total wavefield accordingly to the FWMod scheme:

$$\vec{Q}^+(z_0) = \vec{S}^+(z_0) + \mathbf{R}^\cap(z_0)\vec{P}_{mod}^-(z_0). \quad (2.18)$$

In the first scenario (Equation 2.17) the propagation and reflectivity will have a linear effect – all orders of surface multiples will have the same roundtrip as primaries but with corresponding traveltimes. In the second scenario (Equation 2.18) surface multiples are modeled from the upgoing modeled wavefield in a non-linear manner, meaning that they will finally be modeled originally from the source wavelet $\vec{S}(z_0)$ that is going back and forth each modelling roundtrip. Therefore, the reflectivity and propagation operators will affect each order of surface scattering differently, and, thus, this modeling of surface multiples can be referred to as non-linear.

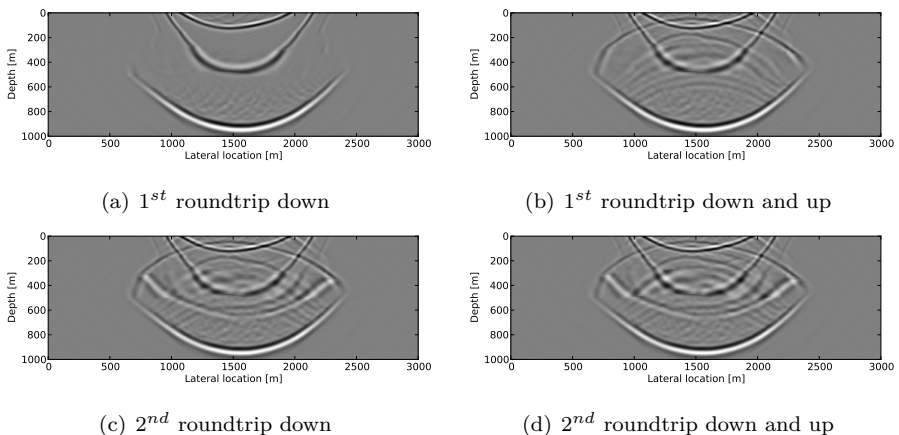


Figure 2.11: Snapshots of the FWMod of modeling total data by re-injecting the 'observed' wavefields at the surface together with the original source wavelet. a-d) Total (upgoing + downgoing) FWMod wavefields at the first and second modelling iterations, respectively.

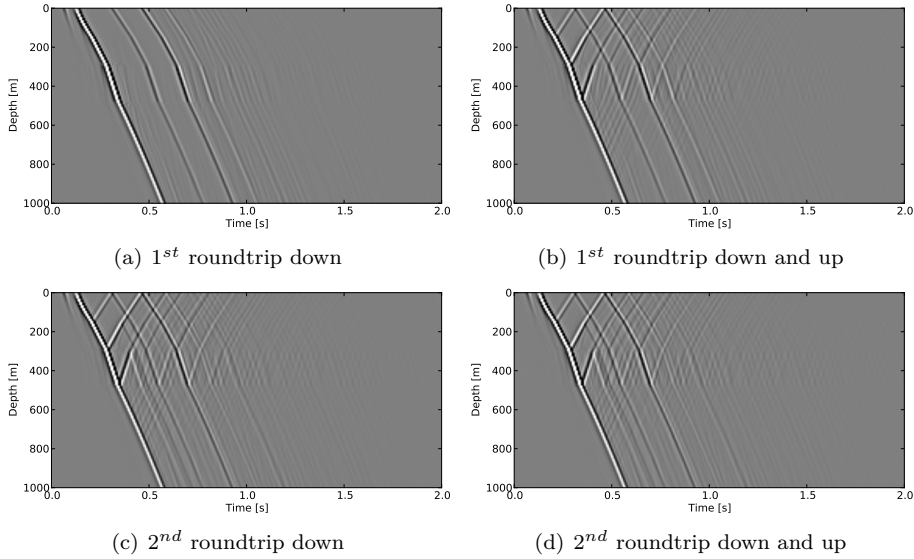


Figure 2.12: VSP zero-offset section of modeling total data by re-injecting the 'measured' wavefield at the surface together with the original source wavelet. a) 1st iteration down only; b) 1st iteration down and up; c) 2nd iteration down only; d) 2nd iteration down and up.

In our numerical example, by simple changing the so-called source-side (input source wavefield) from the source wavelet to the source wavelet combined with re-injected 'observed' data (i.e. the finite-difference data) it is possible to model the full reflection data in the first option as described above. Figure 2.11 shows the snapshots obtained after different roundtrip steps. Corresponding VSP plots are shown in Figure 2.12.

In the second option the surface multiples are modeled directly from the wavelet, and orders of surface of multiples appear after each modelling iteration. This approach can also be very interesting for the velocity model estimation as this case is more sensitive to velocity errors, while the first approach of modelling surface multiples has the same sensitivity as that for primaries.

Note, finally, that modeling of internal multiples is always non-linear: the modeled data is 're-injected' downward at each subsurface grid-point.

2.5.3 Separate modelling of the surface multiples

Surface multiples can also be modelled separately. In this case we simply neglect the source term in Equation 2.17. Note that again the two re-injecting options are possible: the 'observed' data or modelling all orders of surface multiples by applying \mathbf{R}^\cap at the surface. Figure 2.13 shows the snapshot of the modeled surface multiples

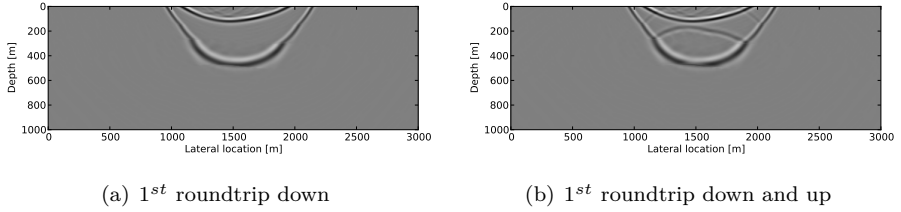


Figure 2.13: Snapshots of the FWMod of the surface multiples modeled by re-injecting the 'measured' wavefields at the surface. a-b) Total (upgoing + downgoing) FWMod wavefield after the downward trip and after the upward trip respectively.

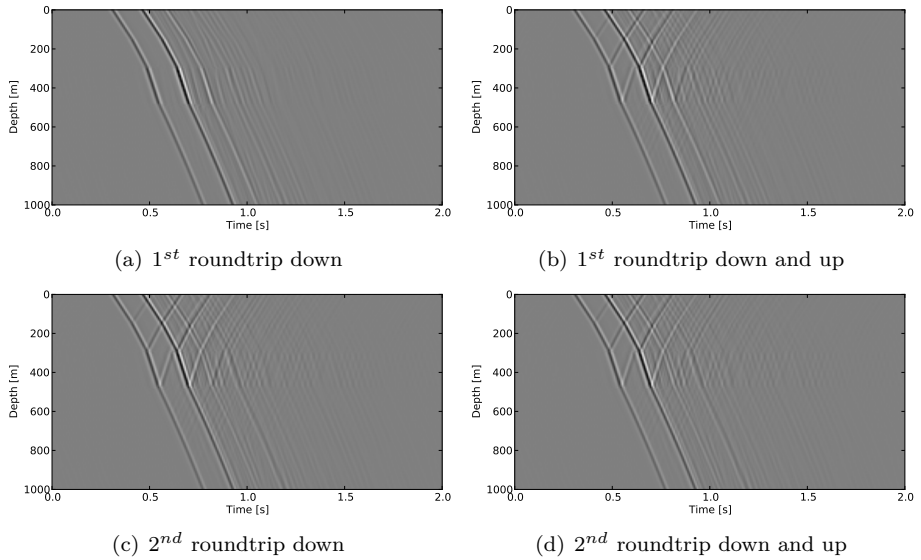


Figure 2.14: VSP zero-offset section of the modeled surface multiples by re-injecting 'measured' data. a) 1st iteration down only; b) 1st iteration down and up; c) 2nd iteration down only; d) 2nd iteration down and up.

and figure 2.14 shows the pseudo VSP plots. In both cases we used the 'observed' data for the re-injection at the surface.

2.5.4 Modelling of blended wavefields

It is also possible to simulate the blended (simultaneous) sources that should be necessary for closed-loop imaging of blended data. In this way the total downgoing wavefield at the surface will be as follows:

$$\vec{Q}_{bl}^+(z_0) = \mathbf{Q}^+(z_0)\vec{\Gamma}_{bl}, \quad (2.19)$$

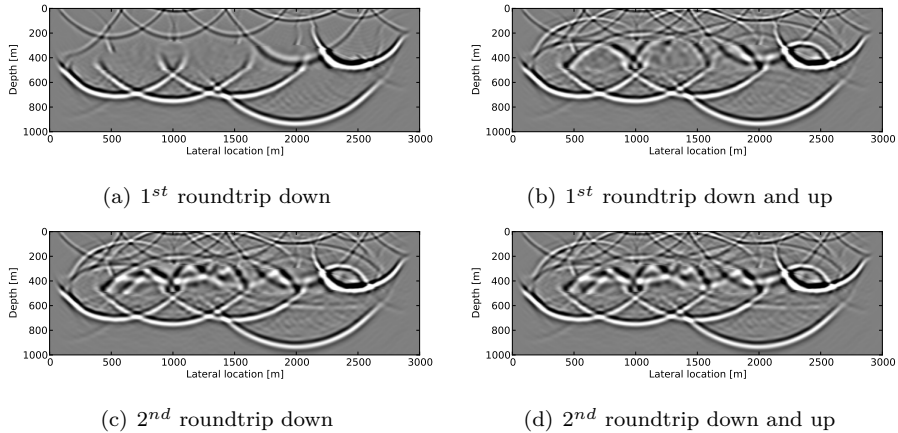


Figure 2.15: Snapshots of the FWMod of a blended source experiment; a-d) Total (upgoing + downgoing) FWMod wavefield at the first and second modelling iterations, respectively

where $\vec{\Gamma}_{bl}$ is one column of the so-called blending matrix (Berkhout, 2008) and \mathbf{Q}^+ represent all total downgoing wavefields in a multi-shot seismic experiment ($\mathbf{Q}^+ = \mathbf{R} \cap \mathbf{P}^-$).

Snapshots of the modeled wavefields as well as VSP zero-offset sections are shown in Figures 2.15 and 2.16 respectively.

It is visible that this is a very complex wavefield, however FWMod simply models any combination of surface and internal multiples.

2.6 Adjoint modelling

In this section we start moving towards the inversion part of the algorithm. FWM, as a member of the inversion-based imaging algorithms family, uses an iterative approach to estimate the solution, being the reflectivity, that explains the input data. An adjoint modelling can be used in order to calculate the gradient for the parameter (reflectivity) updating. In this section the implementation of such modelling is discussed and demonstrated.

In the previous sections a causal propagation operator \mathbf{W} was used for the forward modelling: after each propagation step the wavefield was extrapolated forward in time. By applying the time-reversed mode we can perform the extrapolation that is inverse in time (simply by using \mathbf{W}^H). In this case the so-called back-propagation of the wavefield is applied. Furthermore, using the equations of FWMod, an inverse extrapolation can also be done in a two-way manner.

In principle, the adjoint modelling is performed by equations similar to 2.15 and 2.14 using the adjoint (conjugate transpose) \mathbf{W}^H operator:

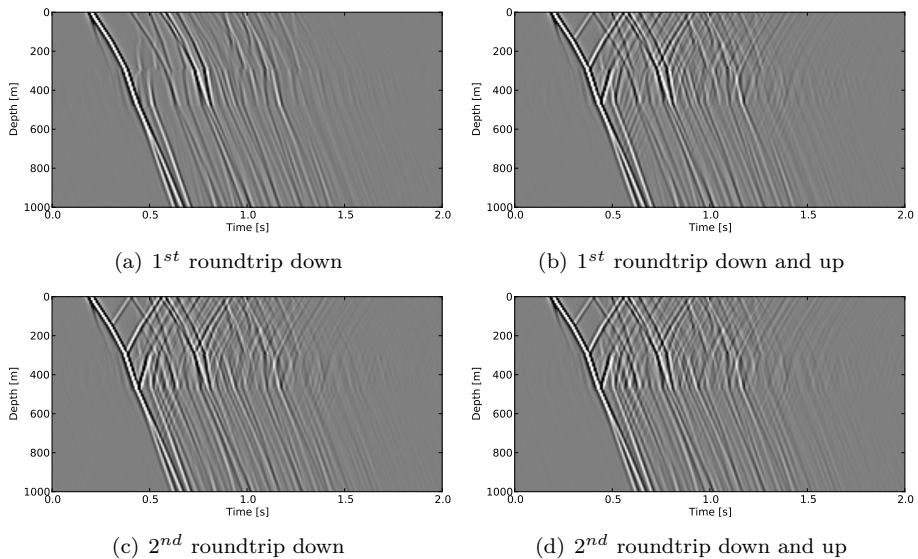


Figure 2.16: Pseudo VSP zero-offset section for FWMod in a blended source experiment. a) 1st iteration down only; b) 1st iteration down and up; c) 2nd iteration down only; d) 2nd iteration down and up.

$$\begin{aligned}
 \vec{P}_a^-(z_m) &= \sum \mathbf{W}^H(z_m, z_n) [\vec{P}_a^-(z_n) + \delta \vec{S}_a(z_n)] \\
 \vec{P}_a^+(z_m) &= \sum_{\substack{n < m \\ n > m}} \mathbf{W}^H(z_m, z_n) [\vec{P}_a^+(z_n) + \delta \vec{S}_a(z_n)],
 \end{aligned} \tag{2.20}$$

where $\delta \vec{S}_a$ connects the back-propagated (modeled in adjoint way) wavefields \vec{P}_a^- and \vec{P}_a^+ :

$$\delta \vec{S}_a = \mathbf{R}^\cup(z_m) \vec{P}_a^+(z_m) + \mathbf{R}^\cap(z_m) \vec{P}_a^-(z_m). \tag{2.21}$$

It is important to note that this modelling is not complete in terms of the scattering, as in the inverse version of FWMod the scattering should be removed while propagating the wavefield forward in depth (Berkhout, 2014a). But such two-way back-propagation approach is used for estimating the reflectivity from below, \mathbf{R}^\cap , and estimating the source properties where two-way back-propagation of the data is required. Both applications will be discussed later on in this thesis.

The adjoint modelling is done in the following manner. Using Equation 2.20, firstly the upgoing wavefield \vec{P}_a^- is back-propagated downwards into the subsurface and stored at every depth level, like we do for the \vec{P}^+ in the forward modelling. Then, the stored wavefield is multiplied by the (potential) reflectivity and is used for the computation of the back-propagated upgoing wavefield \vec{P}_a^+ , which due to this reflection has now become downgoing.

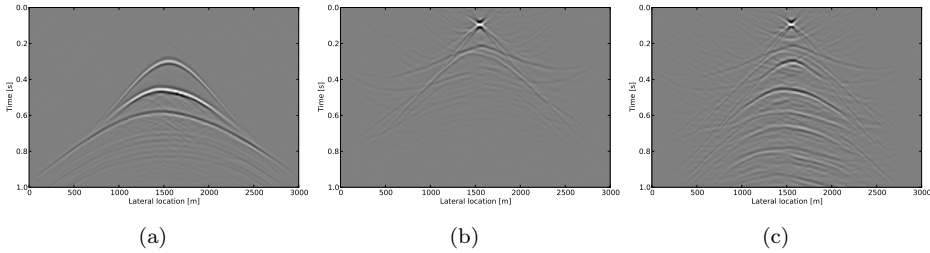


Figure 2.17: Original surface data (a) and result of one roundtrip of adjoint FWMod for non-free surface data (b) and free-surface data (c).

By one roundtrip of adjoint FWMod, the primaries are focused into the wavelet, whereas surface multiples become the new primaries. Basically, each roundtrip of adjoint FWMod removes an order of scattering.

As a numerical example the process is demonstrated on the already familiar dataset used in the forward modelling exercises. Figure 2.17a shows the input data and the result of one roundtrip of adjoint modelling is displayed in Figure 2.17b. It is visible how the primaries are collapsed into the source wavelet. However, it also contains other events like back-propagated internal multiples. Figure 2.17c demonstrates the adjoint FWMod on the data with a free-surface boundary condition. It is visible that, besides the primaries being mainly focused to the source, the first-order surface multiples are transformed to primaries, although only kinematically, with the amplitudes having opposite polarity. Therefore, it is visible that the adjoint modelling does not preserve correct amplitudes and creates non-physical events. However, it can be used in the inversion process for the computation of the gradient for estimating the source as well as a wavefield that is used for the estimation of the reflectivity from below.

Figure 2.18a shows in a VSP mode the result of the downward back-propagation of the wavefield (\vec{P}_a^-) into the subsurface and the following upward back-propagation of the wavefield \vec{P}_a^+ back to the surface is displayed in Figure 2.18b. It is also visible that the adjoint FWMod does not remove the scattering. However, the scattering can be removed if full inverse FWMod is applied (Berkhout, 2014a), where subtraction and not addition of the scattering term is performed.

2.7 Discussion

The introduced forward model allows to calculate the upgoing and downgoing wavefields that include the complex scattering effects (transmission and coda) using the Bremmer series. This approach has similarities with other iterative or recursive and integral-based seismic modelling approaches:

Besides the Bremmer series approach two methods based on similar principles are

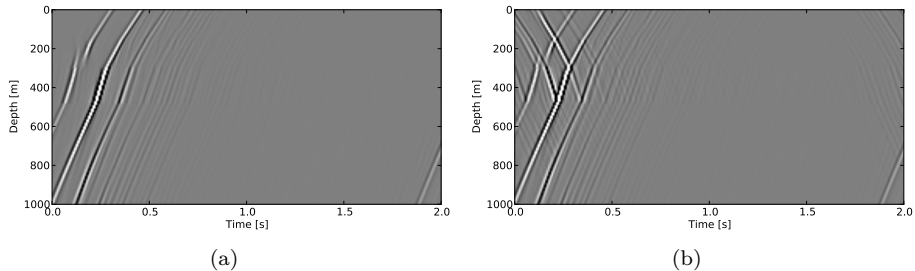


Figure 2.18: Result of the downward back-propagation (half round-trip) (a) and result of one full adjoint FWMod roundtrip (b).

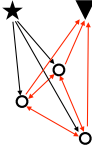
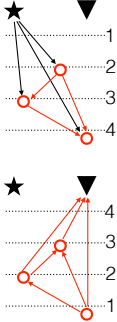
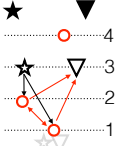
discussed below – Kennett modeling (reflectivity method) and the scattering integral. All methods explain the scattering as the incoming wavefield scaled by a factor that can be either reflectivity or a function based on the difference between background and true parameters. However, all methods have different ways to compute the resulted scattered wavefield.

Kennett modelling (Kennett, 2009), also known as the ‘reflectivity method’ (Fuchs and Müller, 1971), constructs the wavefields by first considering the impulse response for unit sources and receivers at the deepest depth level and recursively shifting depth levels upwards from one to another until the final depth level (i.e. the surface) is reached: at every step virtual sources and receivers of that response are kept at equal depths. Therefore, this approach operates with one impulse response that is continuously updated and does not require to compute and store both upgoing and downgoing wavefields at every depth level of the subsurface. Moreover, during the recursive modelling process, everything that is above the virtual depth level is assumed to be homogeneous. So in each modelling step the effect of adding one extra layer to the current model is added. This method takes internal multiples into account via a prediction series. The method assumes horizontally layered media and is usually calculated in the plane wave domain. Afterwards, by combining different plane wave responses, the impulse response in the spatial domain can be obtained by inverse spatial Fourier or linear Radon transformation.

Alternatively to Kennett modelling and the Bremmer series (FWMod), the method of the scattering integral (van den Berg et al., 1999; De Hoop, 2008) is based on a two-way approach and considers omnidirectional propagation of wavefields (no preferred propagation direction). In a similar way as in FWMod, it allows to include multiple scattering by iterations. However, the computation of the wavefield within one iteration is not recursive in depth – as there is no preferred direction – and it requires computation of point-by-point Green’s functions in a background model for each pair of subsurface grid-points. Scattering is described by multiplying the total data in each grid-point by a contrast function. The latter guarantees the difference in medium parameters of background and true medium.

Table 2.2 summarizes similarities and differences between FWMod and other integral-based modelling approaches.

Table 2.2: Comparison of the integral-based modeling.

Method	Scattering integral	FWMod / Bremmer series	Kennett
Calculation	Point-to-point	Recursive in depth	Recursive in depth
Scattering order	Iteratively	Iteratively	In one step
Scattering mechanism	Property contrasts	Reflectivity	Reflectivity
Direction	Two-way Green's functions	One-way propagation operators	One-way propagation operators
Illustration			

2.8 Conclusions

In this chapter the main aspects of the full wavefield modelling process (FWMod) have been described. The main features of FWMod are:

1) The forward model strictly separates propagation (phase) and the dynamics (amplitude) of the modeled data by two 'orthogonal' parameters: velocity (layer properties) and reflectivity (boundary properties). Such separation plays an important role when performing inversion, which is discussed in the next chapter. Such approach also allows to generate multiple reflections and transmission effects even when a smooth migration velocity model is used. Note that this is not possible when finite-difference modelling is used as a forward modelling algorithm.

2) The modelling can be done in an angle-independent and an angle-dependent manner. The former is relatively easy (requires a structural image), however is not accurate in case of big velocity contrasts (causing AVO effects), whereas the latter

is more accurate, but more complex as it requires full reflectivity matrices at each depth level and is, therefore, computationally more expensive.

3) The modelling is recursive and similar to the Bremmer series. At each iteration (roundtrip) a new order of scattering is included. The input wavefields can be differently defined for different modelling modes. There is a choice of modelling primaries, surface multiples, total wavefield, blended sources. Independently of the source wavefield, the algorithm will simulate the correct transmission effects and internal multiples. Orders of multiples is under user control, so it is possible to model specific order of multiples by subtracting the data with n^{th} and $(n - 1)^{th}$ order of scattering.

4) The modelling can be done in an adjoint manner (back-propagation). Such approach can be used in the imaging process for estimating the reflectivity from below or for the source wavelet estimation.

3

Imaging

In the previous chapter it was extensively discussed how to model the total reflection data using Full Wavefield Modeling (FWMod). This chapter covers another important part of the FWM scheme: the imaging. The basics of this method have been described in Berkhout (2012) with initial examples given by Davydenko et al. (2012). Later on, Berkhout (2014b) more extensively described the main theoretical aspects of FWM.

As an inversion-based method, FWM comprises a gradient computation step. In this chapter it will be shown that the gradient is obtained via a cross-correlation imaging condition applied to the total modeled wavefield (that also contains multiple scattering and the coda) and the back-propagated data residual. Next, the options to parameterize the model space will be discussed (i.e. the angle-dependent versus the angle-independent approach). Further, different ways of parameter updating will be described, namely imaging from above and imaging from below. It will be shown that imaging from below involves the use of internal multiples explicitly. Finally, numerical examples will illustrate all aspects of this chapter.

3.1 Introduction

An important part of the closed-loop process (shown in Figure 1.7) is the imaging. At every iteration of this loop the forward modeled data is compared with the observed data and the residual is computed by subtraction. This misfit is then imaged, which means that it is translated from the data to the model domain, and serves as an

update for the reflectivity. The residual may contain spurious events caused by the modeling process, such as crosstalk from multiples that was mapped in the image. Such events will have a polarity opposite to the corresponding events in the image as they are the result of the subtraction of the (wrongly) modeled data from the measured one. Therefore, by imaging the residual and updating the image such crosstalk, iteration by iteration, will be suppressed in an oscillating manner.

3.2 Imaging and gradient computation

Generally speaking, the FWM algorithm aims at minimizing the difference between the observed and the modeled data, where the latter is computed using the estimated reflection and/or transmission coefficients. The objective function can be described as:

$$J = J_{\Delta} + J_f, \quad (3.1)$$

where the first term quantifies the data mismatch and the second term:

$$J_f = \epsilon F(\mathbf{m}) \quad (3.2)$$

is responsible for the regularization of the estimated model space \mathbf{m} being an argument of some constraining functional F .

The first term in Equation 3.1 is a misfit norm function:

$$J_{\Delta} = \sum_{\omega} \text{tr}(\Delta \mathbf{P} \Delta \mathbf{P}^H), \quad (3.3)$$

where $\Delta \mathbf{P}$ is a data residual – being the difference between observed data \mathbf{P}_{obs}^- and modeled data \mathbf{P}_{mod}^- :

$$\Delta \mathbf{P} = \mathbf{P}_{obs}^- - \mathbf{P}_{mod}^-, \quad (3.4)$$

where \mathbf{P}_{mod}^- and \mathbf{P}_{obs}^- describe now data in a multi-shot experiment.

Each column of the modeled data \mathbf{P}_{mod}^- describes one shot record and is defined as:

$$\vec{P}_{mod}^-(z_0) = \sum_{n>0} \mathbf{W}^-(z_0, z_n) \delta \vec{S}^-(z_n), \quad (3.5)$$

when all sources are assumed at z_0 and $\delta \vec{S}^-(z_n)$ is defined as:

$$\delta \vec{S}^-(z_n) = \mathbf{R}^{\cup}(z_n) \vec{P}_{mod}^+(z_n) + \delta \mathbf{T}^-(z_n) \vec{P}_{mod}^-(z_n). \quad (3.6)$$

The downgoing wavefield is given as:

$$\vec{P}_{mod}^+(z_n) = \mathbf{W}^+(z_n, z_0) \vec{S}^+(z_0) + \sum_{m>0} \mathbf{W}^+(z_n, z_m) \delta \vec{S}^+(z_m), \quad (3.7)$$

where

$$\delta\vec{S}^+(z_n) = \delta\mathbf{T}^+(z_n)\vec{P}_{mod}^+(z_n) + \delta\mathbf{R}^\cap(z_n)\vec{P}_{mod}^-(z_n). \quad (3.8)$$

By substituting Equation 3.8 into Equation 3.7, Equation 3.7 into Equation 3.6 and finally Equation 3.6 into Equation 3.5 it can be seen that the modeled data is a function of the parameter space $\mathbf{M} = [\mathbf{R}^\cup, \mathbf{R}^\cap, \delta\mathbf{T}^+, \delta\mathbf{T}^-]$. Note, that propagation operators \mathbf{W}^\pm and the source wavelet \vec{S}^+ can also be part of the model space. However, estimation of the propagation operators is outside the scope of this thesis. This is described by the Joint Migration-Inversion (JMI) process, as described as by Berkhout (2014c) and Staal et al. (2014). Estimation of the source wavelet is discussed further in Chapter 5.

The second term from Equation 3.1 can be considered as a penalty function applied to \mathbf{M} and, thereby, \mathbf{F} produces an undesired feature of \mathbf{M} to be penalised. The importance of this term is controlled by the ϵ scalar. For instance one can penalize variations of the model by applying a first-order derivative operator and, thereby, promote flatness of the solution. Smoothness of the solution can be promoted by involving a second-order derivative operator. A sparsity constraint (e.g. Cauchy constraint) can be included in order to suppress reflector side-lobes and crosstalk remainders and, thereby, increase the resolution. An objective function for the Cauchy constraint takes the following form:

$$J_f = \epsilon \sum_i \frac{1}{2} \ln\left(1 + \frac{M_i^2}{\sigma^2}\right), \quad (3.9)$$

where index i stands for the sample of the model space. The gradient of this term is given as follows:

$$\left[\frac{\partial J_f}{\partial \mathbf{M}}\right]_i = \epsilon \frac{M_i}{\sigma^2 + M_i^2}, \quad (3.10)$$

where again index i indicates a single sample of the gradient.

The term described in Equation 3.9 is non-quadratic and, therefore, the contribution of its gradient (Equation 3.10) to the gradient of the first term J_Δ will make the total gradient to be affected by the amplitude of the model space sample. Therefore, the main peaks of the reflectors can be enhanced with simultaneous side-lobes suppression, which may lead to higher resolution of the estimated image. Parameter σ controls the 'aggression' of the constraint. For more details the reader is referred to Sacchi et al. (2006) or Schouten (2012).

Figure 3.1 shows an impulse response for each parameter. As visible in Equation 3.5 and 3.6 a grid-point response of the reflectivity from above \mathbf{R}^\cup (Figure 3.1a) and upward transmission \mathbf{T}^- (Figure 3.1b) are mostly linearly related to the measured data, whereas impulse responses for the reflectivity from below \mathbf{R}^\cap and downward transmission \mathbf{T}^+ have a non-linear relationship with the measured data due to the extra round-trip via reflection at every reflector located below the depth level of consideration (Figure 3.1c and d respectively). Note that transmission coefficient may also partly include additional scattering effects also known as duplex or prismatic reflections (N. Marmalevskiy, 2007).

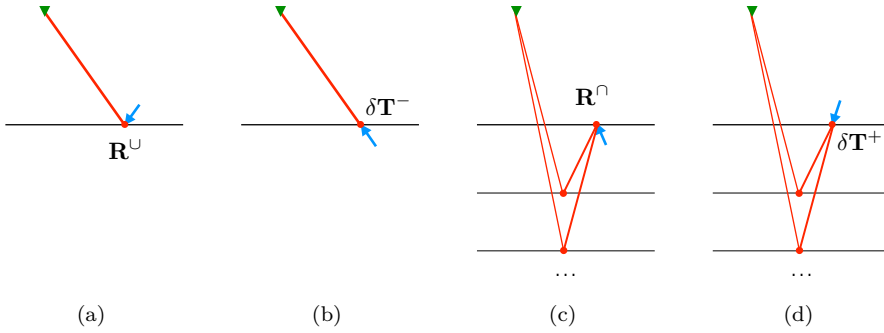


Figure 3.1: Impulse responses for upward reflectivity (a), upward transmission (b), downward reflectivity(c) and downward transmission (d).

3.2.1 Gradient for upward reflectivity and transmission

Estimation of four independent parameters from measured surface data can be a difficult task. If we assume an acoustic case it is not necessary to estimate this complete set. Provided the estimated reflectivity from above \mathbf{R}^U it is possible to constraint other parameters as follows:

$$\begin{aligned}\mathbf{R}^\cap &= -\mathbf{R}^U \\ \delta\mathbf{T}^+ &= \mathbf{R}^U \\ \delta\mathbf{T}^- &= -\mathbf{R}^U.\end{aligned}\tag{3.11}$$

Note that for elastic media angle-dependent reflectivity can still contain true elastic PP-reflectivity. However, the above assumptions will be less valid for higher angles, but given the improved robustness of FWM, this approximation can be acceptable.

In this case the objective function is dependent on one parameter set:

$$J(\mathbf{R}^U) = J_\Delta(\mathbf{R}^U) + J_f(\mathbf{R}^U).\tag{3.12}$$

In order to compute the model update we need to compute the gradient of the objective function 3.1 with respect to parameters \mathbf{R}^U . According to Petersen et al. (2008) one can use the derivative:

$$\frac{\partial}{\partial \mathbf{X}} \text{tr}[(\mathbf{A}\mathbf{X}\mathbf{B} + \mathbf{C})(\mathbf{A}\mathbf{X}\mathbf{B} + \mathbf{C})^H] = 2\mathbf{A}^H(\mathbf{A}\mathbf{X}\mathbf{B} + \mathbf{C})\mathbf{B}^H,\tag{3.13}$$

and link it with Equation 3.3 such that:

$$\begin{aligned}
\mathbf{A}\mathbf{X}\mathbf{B} + \mathbf{C} &= \Delta\mathbf{P}(z_0), \\
\mathbf{A} &= - \sum_{n>0} \mathbf{W}^-(z_0, z_n), \\
\mathbf{X} &= \mathbf{R}^{\cup}(z_n), \\
\mathbf{B} &= \mathbf{P}_{mod}^+(z_n), \\
\mathbf{C} &= \mathbf{P}_{obs} - \sum_{n>0} \mathbf{W}^-(z_0, z_n) \delta\mathbf{T}^-(z_n) \mathbf{P}_{mod}^-(z_n).
\end{aligned} \tag{3.14}$$

According to Equation 3.13 and Equations 3.14 the derivative of the objective function, defined in Equation 3.3, in respect to the upside reflectivity $\mathbf{R}^{\cup}(z_n)$ (for given the depth level z_n and frequency ω) will be as follows:

$$\left[\frac{\partial J_{\Delta}}{\partial \mathbf{R}^{\cup}(z_n)} \right]_{\omega} = -2[\mathbf{W}(z_0, z_n)]^H [\Delta\mathbf{P}(z_0)] [\mathbf{P}_{mod}^+(z_n)]^H. \tag{3.15}$$

Therefore, according to Equation 3.15, we see that the reflectivity update at level z_n , described by this gradient, is obtained by cross-correlation of the data residual $\Delta\mathbf{P}(z_m)$ - back-propagated to the depth level z_m by operator \mathbf{W} - with the downgoing wavefield $\mathbf{P}^+(z_m)$ given by the full wavefield modeling. This is also identical to the cross-correlation imaging condition used in regular migration algorithms.

The imaging condition involves wavefield propagating in opposite directions. Therefore, \mathbf{R}^{\cup} estimation implies matching the opposite wavefields during the last bounce of corresponding events.

Although it is quite efficient to estimate the transmission part as $\delta\mathbf{T}^- = -\mathbf{R}^{\cup}$ one can estimate it explicitly by calculating the gradient similar to Equations 3.13 and 3.14. For this derivation, matrices for Equation 3.13 need to be chosen as follows:

$$\begin{aligned}
\mathbf{A}\mathbf{X}\mathbf{B} + \mathbf{C} &= \Delta\mathbf{P}(z_0), \\
\mathbf{A} &= - \sum_{n>0} \mathbf{W}^-(z_0, z_n), \\
\mathbf{X} &= \delta\mathbf{T}^-(z_n), \\
\mathbf{B} &= \mathbf{P}_{mod}^-(z_n), \\
\mathbf{C} &= \mathbf{P}_{obs} - \sum_{n>0} \mathbf{W}^-(z_0, z_n) \mathbf{R}^{\cup}(z_n) \mathbf{P}_{mod}^+(z_n),
\end{aligned} \tag{3.16}$$

and the resulting gradient will be:

$$\left[\frac{\partial J_{\Delta}}{\partial \mathbf{T}^-(z_n)} \right]_{\omega} = -2[\mathbf{W}(z_0, z_n)]^H [\Delta\mathbf{P}^-(z_n)] [\mathbf{P}_{mod}^-(z_n)]^H. \tag{3.17}$$

Equation 3.17 shows that gradient for the upward transmission part can be obtained by a cross-correlation of wavefields that propagate in the same direction: the back-propagated upgoing receiver-side residual wavefield and the forward modeled upgoing source-side wavefield.

3.2.2 Gradient for downward reflectivity and transmission

As was mentioned earlier, recursive substitutions of Equations 3.8, 3.7 and Equation 3.6 in Equation 3.5 makes it possible to realise the link of the measured data with the downward reflectivity \mathbf{R}^\cap and the downgoing transmission $\delta\mathbf{T}^+$.

Using the principles discussed in the previous section we can compute the gradient for the downward reflectivity by choosing matrices in Equation 3.13 as follows:

$$\begin{aligned}
\mathbf{A}\mathbf{X}\mathbf{B} + \mathbf{C} &= \Delta\mathbf{P}(z_0), \\
\mathbf{A} &= - \sum_{n>m} \mathbf{W}^-(z_0, z_n)\mathbf{R}^\cup(z_n) \sum_{m<n} \mathbf{W}^+(z_n, z_m), \\
\mathbf{X} &= \mathbf{R}^\cap(z_m), \\
\mathbf{B} &= \mathbf{P}_{mod}^-(z_m), \\
\mathbf{C} &= \mathbf{P}_{obs} - \sum_{n>0} \mathbf{W}^+(z_0, z_n)\delta\mathbf{S}^+(z_n) - \\
&\quad - \sum_{n>m} \mathbf{W}^-(z_0, z_n)\mathbf{R}^\cup(z_n) \sum_{m<n} \mathbf{W}^+(z_n, z_m)\delta\mathbf{T}(z_m)\mathbf{P}^+(z_m),
\end{aligned} \tag{3.18}$$

and finally the derivative is:

$$\left[\frac{\partial J_\Delta}{\partial \mathbf{R}^\cap(z_n)} \right]_\omega = -2 \sum_{m<n} [\mathbf{W}^-(z_0, z_m)\mathbf{R}^\cup(z_m)\mathbf{W}^+(z_m, z_n)]^H [\Delta\mathbf{P}^-(z_0)][\mathbf{P}_{mod}^-(z_n)]^H. \tag{3.19}$$

As it can be observed in Equation 3.19, for updating the reflectivity from below \mathbf{R}^\cap , the upgoing modeled wavefield is cross-correlated with the data residual that was firstly back-propagated downwards at every depth-level located below the target depth level, multiplied by the reflectivity of these levels ($z_m > z_n$) and finally back-propagated upwards to the target depth level z_n . Note that downward reflectivity is mainly responsible for generating the internal multiples as it translates the upgoing incoming wavefield downwards to the subsurface, which make it possible to reach the surface only by one extra upward reflectivity \mathbf{R}^\cup . Therefore, by estimating the downward reflectivity we directly address internal multiples for imaging, whereas the reflectivity from above is mainly driven by information coming from primaries. The process of estimating the reflectivity from below is similar to imaging of internal multiples proposed by Malcolm et al. (2009). However, in case of FWM, every combination and all orders of the internal multiples are automatically included, whereas the work of Malcolm et al. (2009) focuses specifically on first-order internal multiples.

In order to estimate the downward transmission we need to slightly modify the Equation 3.13 as follows:

$$\begin{aligned}
\mathbf{A}\mathbf{X}\mathbf{B} + \mathbf{C} &= \Delta\mathbf{P}(z_0), \\
\mathbf{A} &= - \sum_{n>m} \mathbf{W}^-(z_0, z_n) \mathbf{R}^\cup(z_n) \sum_{m<n} \mathbf{W}^+(z_n, z_m), \\
\mathbf{X} &= \delta\mathbf{T}^+(z_m), \\
\mathbf{B} &= \mathbf{P}_{mod}^+(z_m), \\
\mathbf{C} &= \mathbf{P}_{obs} - \sum_{n>0} \mathbf{W}^-(z_0, z_n) \delta\mathbf{S}^+(z_n) - \\
&\quad - \sum_{n>m} \mathbf{W}^-(z_0, z_n) \mathbf{R}^\cup(z_n) \sum_{m<n} \mathbf{W}^+(z_n, z_m) \mathbf{R}^\cap(z_m) \mathbf{P}^-(z_m),
\end{aligned} \tag{3.20}$$

such that we get the final derivative with respect to the downward transmission:

$$\left[\frac{\partial J_\Delta}{\partial \delta\mathbf{T}^+(z_n)} \right]_\omega = -2 \sum_{m>n} [\mathbf{W}(z_0, z_m) \mathbf{R}^\cup(z_m) \mathbf{W}(z_m, z_n)]^H [\Delta\mathbf{P}^-(z_0)] [\mathbf{P}_{mod}^+(z_n)]^H. \tag{3.21}$$

This imaging condition involves cross-correlation of the downgoing forward modeled wavefield with the back-propagated data residual via reflections at the levels below the target level, which is also downgoing at the target level.

3.2.3 Remarks on parameter selection

In the previous section we only considered the gradient from the data misfit J_Δ . In addition the gradient note for the constraint term J_f should be calculated separately.

Thus, the gradients for all four types of parameters that are responsible for the scattering in the forward model are as follows:

$$\begin{aligned}
\Delta\mathbf{R}^\cup(z_m) &\simeq [\Delta\mathbf{P}^-(z_m)] [\mathbf{P}^+(z_m)]^H + \frac{\partial}{\partial \mathbf{R}^\cup} (J_f) \\
\Delta\mathbf{R}^\cap(z_m) &\simeq [\Delta\mathbf{P}^+(z_m)] [\mathbf{P}^-(z_m)]^H + \frac{\partial}{\partial \mathbf{R}^\cap} (J_f) \\
\Delta\delta\mathbf{T}^-(z_m) &\simeq [\Delta\mathbf{P}^-(z_m)] [\mathbf{P}^-(z_m)]^H + \frac{\partial}{\partial \mathbf{R}^\cup} (J_f) \\
\Delta\delta\mathbf{T}^+(z_m) &\simeq [\Delta\mathbf{P}^+(z_m)] [\mathbf{P}^+(z_m)]^H + \frac{\partial}{\partial \mathbf{R}^\cap} (J_f),
\end{aligned} \tag{3.22}$$

As discussed before, the most easy and robust inversion approach is to estimate the upward reflectivity \mathbf{R}^\cap only and express all three parameters dependent on it (see again Equation 3.11). However, additional information can be extracted from multiple scattering if we estimate reflectivity from below separately, as will be shown later on in this chapter. In order to put more emphasis on getting good reflectivities in areas of weak illumination and amplify reflectivities in the early iterations Berkhout

(2014b) suggests to use a deconvolution imaging condition instead (implemented by weighted cross-correlation).

Regarding the differential transmission operators $\delta\mathbf{T}^\pm$, the additional information can be obtained via so-called duplex waves (i.e, internal multiples with two reflections where one of the reflections does not change its vertical propagation direction), which allows to estimate vertical structures. Examples of the estimation of the transmission effects will be shown from the perspective of duplex waves imaging in Chapter 4. For the rest of this chapter we will focus on the reflectivity operators.

Independent of the choice of parameterization, correct estimation of the model parameter(s) should lead to the correct explanation of the observed data in terms of the primary and multiple reflections and including transmission effects at every step. The crosstalk that is formed when the forward model assumes a linear relationship between the reflectivity and the observed data, as is done in conventional least-squares migration (Nemeth et al., 1999). Another advantage of FWM is that an additional coda is included in the source-side wavefield, which provides additional subsurface illumination by internal multiples. Note that, as discussed in Chapter 2, the source-side wavefield can be any type: a point source or an areal source that represents surface multiples. It is also possible to incorporate blended sources. Each source wavefield will have its own internally scattered wavefields (internal multiples).

In the next section we will discuss two possibilities to parameterize the model space: in an angle-dependent and an angle-independent mode, and their associated gradients.

3.3 Parameterisation

The reflectivity update $\Delta\mathbf{R}$, after being transformed to the time-domain, for each subsurface location contains a spike event focused around zero-time. However, it also contains causal and anti-causal components. It is not desired to have these causal and anti-causal arrivals in the reflectivity operator as they are not physically linked to the depth level of consideration where the potential reflector is. Therefore, it is important to exclude such events. In order to constrain the reflectivity around zero time we apply summation over all frequencies and, thereby, apply zero-time selection from the gradient data. However, for angle-dependent reflectivity this process needs to be applied in the angle or ray parameter domain. The options are discussed in the next two subsections.

3.3.1 Angle-independent mode

The simplest parameterization of the model space is related to structural imaging. In this case each grid point of the subsurface is characterized by a single reflection coefficient, that can efficiently explain the complete reflection event in the data

domain. Such choice is suitable when the medium contrasts are present mainly by density variations, when the offsets in the data are small, or when obtaining a structural image is the only aim of the process.

Since there is only one reflection coefficient per grid point, the reflectivity process is described by a simple, local scalar multiplication of the wavefield with these coefficients and the reflectivity matrix is composed of the diagonal elements. Therefore, the gradient is computed by diagonal selection and summing over frequencies in Equation 3.22, which will correspond to selecting the zero-time component from the conventional cross-correlation imaging condition:

$$\begin{aligned}\overline{\Delta R_{ij}^{\cup}}(z_n) &= 2Re\{\sum_{\omega} \Delta R_{ij}^{\cup}(z_n)\delta_{ij}\} \\ \overline{\Delta R_{ij}^{\cap}}(z_n) &= 2Re\{\sum_{\omega} \Delta R_{ij}^{\cap}(z_n)\delta_{ij}\}.\end{aligned}\quad (3.23)$$

The angle-independent imaging condition may be computed by trace-by-trace cross-correlation of source-side (\vec{P}^+) and receiver-side ($\Delta\vec{P}^-$) wavefields for each source experiment and sum these results. In principle, for every depth level the diagonal elements of the reflectivity matrix $\mathbf{R}(z_m)$ for each frequency component contains the seismic image, where each diagonal element corresponds to one specific lateral location.

3.3.2 Angle-dependent mode

In the angle-dependent mode the reflection coefficient at every point is estimated as a function of angle or ray-parameter. de Bruin et al. (1990) showed that the angle-dependent reflection information can be transformed from the wavenumber to the space domain and these reflectivity operators fill the columns of the \mathbf{R} -matrix. Extra information that describes of angle-dependent reflection coefficients comes from the off-diagonal elements of the reflectivity matrix. These off-diagonal elements can be considered as a local offsets of the reflectivity functions. As in the angle-independent version we would like to select zero-time from the source-side and receivers cross-correlation result. However, due to the angle-dependency this time constraint is best applied in the linear Radon domain. It is computed as follows:

$$\overline{\Delta\mathbf{R}}(z_n) = \mathbf{L}\{2Re(\sum_{\omega} \mathbf{L}^H\{\Delta\mathbf{R}(z_n)\})\}, \quad (3.24)$$

where operators $\mathbf{L}\{\}$ and $\mathbf{L}^H\{\}$ mean forward and backward linear Radon transformation, respectively. The reflectivity is constrained at zero-time by summing all frequencies ω . Matrix $\Delta\mathbf{R}$ is described in equation 3.22. Diagonal elements of this matrix represent again the 'standard' imaging condition, whereas off-diagonal elements represent so-called extended imaging conditions - source and receiver side wavefields are selected in a such way that they are being cross-correlated with some lateral shift related to each other. The larger the distance from the diagonal, the larger the lateral shift. The angle-dependent information is contained along these lateral shifts, or subsurface offsets h (Berkhout and Verschuur, 1997; Sava and Fomel, 2003).

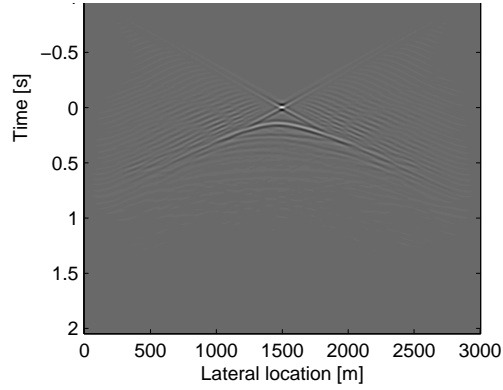
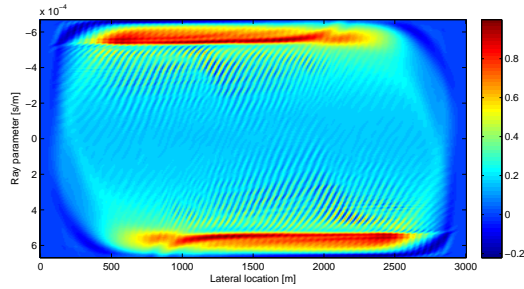
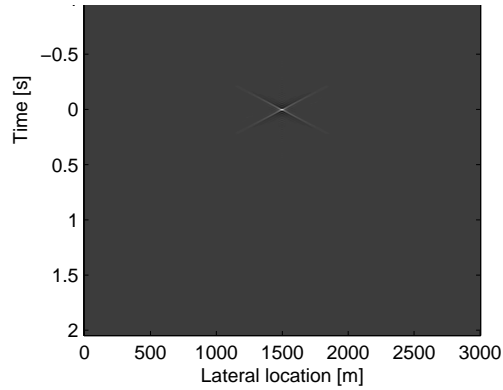
(a) $\Delta\mathbf{R}$ (b) $\sum_{\omega} \mathbf{L}\{\Delta\mathbf{R}\}$ (c) $\overline{\Delta\mathbf{R}} = \mathbf{L}^H\{\sum_{\omega} \mathbf{L}\{\Delta\mathbf{R}\}\}$

Figure 3.2: Example of the angle-dependent reflectivity estimation. a) Column of the $\Delta\mathbf{R}$ matrix in the time domain. b) Estimated AVP values at the depth level with a horizontal boundary. c) Result of applying the zero-intercept time imaging constraint to b) in the linear Radon domain and transforming the result back to the space-time domain.

The \mathbf{L} matrix is a Radon transform matrix:

$$L_{ij} = e^{i\omega p_i h_j}, \quad (3.25)$$

where p is a ray parameter and h is an offset. As it contains offset lateral vector h , it is applied to the offset axis: the diagonal elements of the gradient correspond to zero-offset and decreasing/increasing column-wise. Therefore, the gradient matrix is skewed (indicated by the $\{ \}$ signs) before the Radon transform is applied.

Note that in principle reflectivity operator \mathbf{R} (when considered for all frequencies) has the same size as the complete data volume, which has the danger of over-parameterisation. Therefore, the estimate of \mathbf{R} in the linear Radon domain is constrained at zero-time by stacking all frequencies. However, the Radon domain keeps the angle-dependent information along the ray parameter axis. In this interpretation, the angle-independent case (with non-zero diagonal elements only) may be considered as a spike operator in the space domain, meaning that in the angle-domain all values are constant along the ray parameter axis. Note that for the angle-dependent case the resulting reflectivity operator is still frequency dependent, because it involves a frequency-dependent transformation (See Equation 3.24 and 3.25).

After estimating the reflectivity (convolution) matrix as described in Equation 3.24, this matrix can be used for the forward modeling in order to explain the observed data. Figure 3.2 shows the estimation process for the first horizontal reflector of the model shown in Figure 1.4. As an example (Figure 3.2), for each frequency slice one column of the $\Delta\mathbf{R}$ matrix has been selected and transformed to the time-domain (see Figure 3.2a). Figure 3.2b shows the Radon transform of the $\sum_{\omega} \mathbf{L}^H \Delta\mathbf{R}$ matrix (at $\tau = 0$). Note that the post-critical reflectivity effect can be clearly observed. Figure 3.2c demonstrates how the adjoint Radon transform can recover the reflectivity operator from the AVP plot. Such operator contains only a spatially band-limited spike-like event, in which angle-dependent reflection information is encoded and which can be used in the forward modeling process.

It can be observed that the model space for the angle-dependent case is represented by angle-domain common image gathers (ADCIGs) and Figure 3.2 basically displays a horizontal selection of ADCIG volume. Theoretically, various constraints can be applied to this type of model space. For example a regularisation penalty function was used in Sava and Fomel (2003) in order to regularize solution and achieve smoothness of the estimated ADCIGs. Applying sparsity constraint can be also included, but one has to be careful in order to avoid provide sparsity along the angle dimension. In this thesis sparsity constraint for the angle-dependent case was not yet implemented.

3.4 Reflectivity updating

Independent of the choice of parameterization we need to update the reflectivity during the FWM process. As a first option we can choose to use the information only from the reflectivity from above and keep reflectivity from below hard-constrained based on an acoustic approximation:

$$\begin{aligned}\mathbf{R}_i^{\cup} &= \mathbf{R}_{i-1}^{\cup} + \alpha \overline{\Delta \mathbf{R}_{i-1}^{\cup}} \\ \mathbf{R}_i^{\cap} &= -\mathbf{R}_i^{\cup},\end{aligned}\quad (3.26)$$

where i stands for iteration number. In this case, the reflectivity is updated mainly from primaries and surface multiples. Internal multiples only contribute implicitly as they become part of the downgoing wavefield. Thus, internal multiples play a more passive role: they are explained and removed from the residual, and thereby don't provide crosstalk in the image.

However, it is also possible to include imaging information from the internal multiples more explicitly by the following imaging condition:

$$\begin{aligned}\mathbf{R}_i^{\cup} &= \mathbf{R}_{i-1}^{\cup} + \alpha [\overline{\Delta \mathbf{R}_{i-1}^{\cup}} - \overline{\Delta \mathbf{R}_{i-1}^{\cap}}] \\ \mathbf{R}_i^{\cap} &= -\mathbf{R}_i^{\cup}.\end{aligned}\quad (3.27)$$

Here, the reflectivity is updated jointly from above and from below.

As a third option, it is also possible to update the reflectivities from above and from below completely independently:

$$\begin{aligned}\mathbf{R}_i^{\cup} &= \mathbf{R}_{i-1}^{\cup} + \alpha \overline{\Delta \mathbf{R}_{i-1}^{\cup}} \\ \mathbf{R}_i^{\cap} &= \mathbf{R}_{i-1}^{\cap} + \beta \overline{\Delta \mathbf{R}_{i-1}^{\cap}}.\end{aligned}\quad (3.28)$$

Note that for this option optionally a link between \mathbf{R}^{\cap} and \mathbf{R}^{\cup} can be incorporated during optimisation, e.g. by including an extra constraint term to the objective function, like $\min \|\mathbf{R}^{\cap} + \mathbf{R}^{\cup}\|^2$.

3.5 Scaling

The $\Delta \mathbf{R}$ obtained from the imaging condition (Equation 3.22) is not at 'true-amplitude' scale and mathematically represents a direction in the steepest descent (or conjugate-gradient) scheme. Therefore, we need to get a scalar for retrieving true amplitudes while updating the reflectivities as mentioned in Equations 3.26 – 3.28. The scalar is computed by minimizing the following quantity:

$$\|\Delta \mathbf{P} - \alpha \mathbf{A}\|_2^2 \rightarrow \min, \quad (3.29)$$

where $\mathbf{A} = \mathbf{P}_{mod}^-(\overline{\Delta \mathbf{R}})$ is the simulated wavefield based on the gradient 'reflectivity'. In other words, the following expression is minimized:

$$J = \text{tr}[(\Delta \mathbf{P} - \mathbf{A})^H (\Delta \mathbf{P} - \mathbf{A})] = \text{tr}[\Delta \mathbf{P}^H \mathbf{A} - \alpha \Delta \mathbf{P}^H \mathbf{A} - \alpha \mathbf{A}^H \Delta \mathbf{P} + \alpha^2 \mathbf{A}^H \mathbf{A}]. \quad (3.30)$$

We need to find α such that J will be minimum. Therefore, the derivative with respect to α is taken:

$$\frac{\partial J}{\partial \alpha} = \text{Tr}[-\Delta \mathbf{P}^H \mathbf{A} - \mathbf{A}^H \Delta \mathbf{P} + 2\alpha \mathbf{A}^H \mathbf{A}] = 0, \quad (3.31)$$

and the scalar factor is given by:

$$\alpha = \frac{\text{tr}[\Delta \mathbf{P}^H \mathbf{A} + \mathbf{A}^H \Delta \mathbf{P}]}{2\text{tr}[\mathbf{A}^H \mathbf{A}]}. \quad (3.32)$$

In the case of multi-parameter inversion (like in Equation 3.28) we have:

$$\begin{aligned} J(\alpha, \beta) &= \text{tr}[(\Delta \mathbf{P} - \alpha \mathbf{A} - \beta \mathbf{B})^H (\Delta \mathbf{P} - \alpha \mathbf{A} - \beta \mathbf{B})] = \\ &= \text{tr}[\Delta \mathbf{P}^H \Delta \mathbf{P} - \alpha \mathbf{A}^H \Delta \mathbf{P} + \alpha^2 \mathbf{A}^H \mathbf{A} + \alpha \mathbf{A}^H \beta \mathbf{B} - \beta \mathbf{B}^H \Delta \mathbf{P} + \beta \mathbf{B}^H \alpha \mathbf{A} + \beta^2 \mathbf{B}^H \mathbf{B}], \end{aligned} \quad (3.33)$$

where \mathbf{A} and \mathbf{B} are wavefields at the surface, modeled with the corresponding gradient updates. Two derivatives are taken, and therefore, α and β might be solved as a following system of equations:

$$\begin{aligned} \frac{\partial J(\alpha, \beta)}{\partial \alpha} &= \text{tr}[-\mathbf{A}^H \Delta \mathbf{P} + 2\alpha \mathbf{A}^H \mathbf{A} + \beta(\mathbf{A}^H \mathbf{B} + \mathbf{B}^H \mathbf{A})] = 0, \\ \frac{\partial J(\alpha, \beta)}{\partial \beta} &= \text{tr}[-\mathbf{B}^H \Delta \mathbf{P} + \alpha(\mathbf{B}^H \mathbf{A} + \mathbf{A}^H \mathbf{B}) + 2\beta \mathbf{B}^H \mathbf{B}] = 0. \end{aligned} \quad (3.34)$$

More generally, in the case of more than two parameters, this system of equations can be observed as a matrix-vector equation, where the matrix has off-diagonal elements that are cross-products between different gradient-responses and diagonal elements that are traces of auto-correlated responses.

After finding α and β , all parameters are updated according to Equations 3.26 – 3.28 and also all wavefields can be updated via Equations 3.5-3.8. The modeled wavefields will provide the new residual that can be used for updating parameters at the next iteration.

3.6 Wavefield options in FWM

Keep in mind the difference between FWM and conventional lease-squares imaging algorithms (Nemeth et al., 1999), which we will refer to as primary wavefield imaging (PWM). The latter are usually based on the simplified Equation 2.14 where the scattering term $\delta \vec{S}$ is neglected, meaning that transmission effects and internal multiples are not included in the forward modelling scheme, although including surface multiples in this approach is still possible. In the next section we will make a comparison between the FWM and PWM approaches.

In Table 3.1 we show how both FWM and PWM can be implemented in three different ways. The difference with PWM is mentioned: in FWM the scattering term $\delta \vec{S}$ is included at each depth level. Note that primary wavefield imaging can be implemented not only to the primary data itself (PWM-prim), but also to the

imaging of surface multiples (PWM-surf) and total data (PWM-tot). In each case, the internal multiples are neglected, whereas FWM takes care of the corresponding internal multiples, independent on the input. Note that any of the six options can describe the situation of simultaneous sources, by redefining \mathbf{S}^+ and \mathbf{S}^- . Table 3.1 shows that if the illuminating wavefield (at the source-side) is the downgoing source wavefield together with the re-injected total data ($\mathbf{Q}^+ = \mathbf{S}^+ + \mathbf{R}^\cap \mathbf{P}^-$), then the total data (at the receiver-side) will be explained. If only the source wavefield \mathbf{S}^+ is used as an illuminating wavefield, then only primaries \mathbf{P}_0^- (and its internal multiples) will be explained. The third situation refers to the re-injection of total data $\mathbf{R}^\cap \mathbf{P}^-$ and in this case the modeled data should match only the surface multiples \mathbf{M}^- and their corresponding internal multiples.

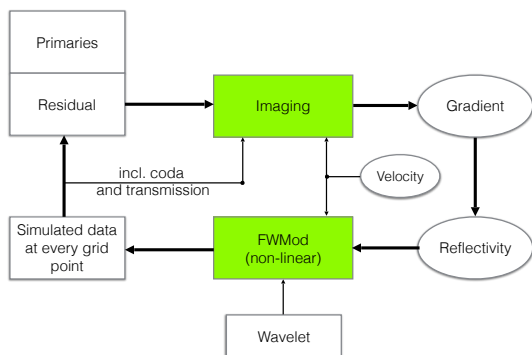
Table 3.1: All three imaging options in the FWM process.

Options	Source side	Receiver Side	$\delta \vec{S}$ included
1a) FWM-tot	$\mathbf{S}^+ + \mathbf{R}^\cap \mathbf{P}^-$	\mathbf{Q}^-	Y
1b) PWM-tot	$\mathbf{S}^+ + \mathbf{R}^\cap \mathbf{P}^-$	\mathbf{Q}^-	N
2a) FWM-prim	\mathbf{S}^+	\mathbf{P}_0^-	Y
2b) PWM-prim	\mathbf{S}^+	\mathbf{P}_0^-	N
3a) FWM-surf	$\mathbf{R}^\cap \mathbf{P}^-$	\mathbf{M}^-	Y
3b) PWM-surf	$\mathbf{R}^\cap \mathbf{P}^-$	\mathbf{M}^-	N

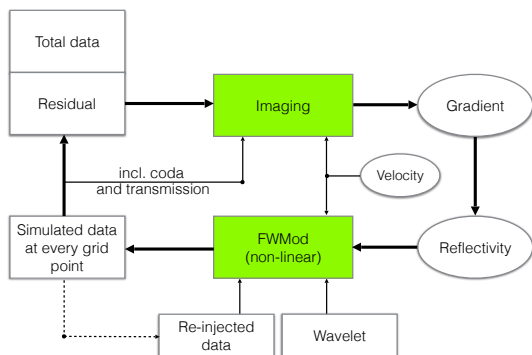
Work flows of options 1a, 2a and 3a are demonstrated in Figure 3.3. Note that the same elements of the closed-loop approach are present. It is only the source-side and receiver-side wavefields that are changed. It is also important to mention that surface multiples may be treated differently when the total data is imaged (Figure 3.3b). Surface multiples can be modeled either in a linear way (observed data is re-injected at the surface and used as a source-field for surface-related multiple illumination). Alternatively, the modeled data can be re-injected as indicated by the dashed path in Figure 3.3b. In this case surface multiples are modeled non-linearly - they are modeled during the iterative FWM procedure in the same way as internal multiples, all starting from the original source field \mathbf{S}^+ .

3.7 Numerical examples

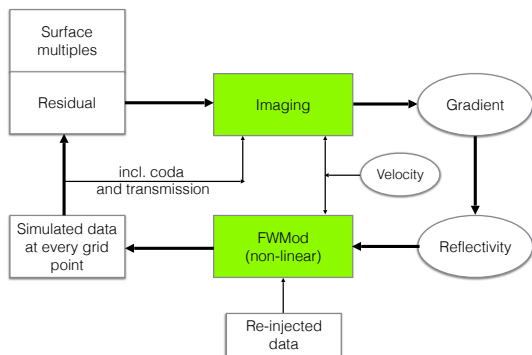
In this section we demonstrate the FWM process with numerical examples. We will make use of the flexibility of the FWM process to run it in various modes: total data, primaries and internal multiples only, or surface multiples only as described by Table 3.1. In addition, we will consider the use of imaging the reflectors from below via internal multiples only.



(a) FWM for primaries



(b) FWM for total data



(c) FWM for surface-related multiples

Figure 3.3: Different FWM workflows according to Table 3.1.

3.7.1 FWM applied to total data

In the first example we consider options 1a and 1b from Table 5.1. We use the velocity and density model shown in Figure 3.4a and b, respectively. As can be ob-

served, the subsurface is featured by a horizontal pack of the layers, representing the target area, and a salt structure that serves as a strong internal multiple generator. It is expected that internal multiples, when being imaged as crosstalk at the first iteration of FWM or at the any iteration of conventional inversion-based imaging, will overwhelm the target reflections.

Reflection data has been modeled by an acoustic finite-difference modeling scheme with sources every 50 meters along the surface. A free-surface boundary condition has been applied. Therefore, the full wavefield, including primaries, surface and internal multiples is considered. The image at the first iteration (Figure 3.4c) represents standard imaging with a cross-correlation imaging condition. The strong crosstalk formed by all multiples is evidently visible. The PWM image is shown in Figure 3.4d. The resulted image has improved in terms of the amplitude and, moreover, the crosstalk from the surface multiples is efficiently suppressed. However, it retains the crosstalk from the internal multiples, as it is not included in

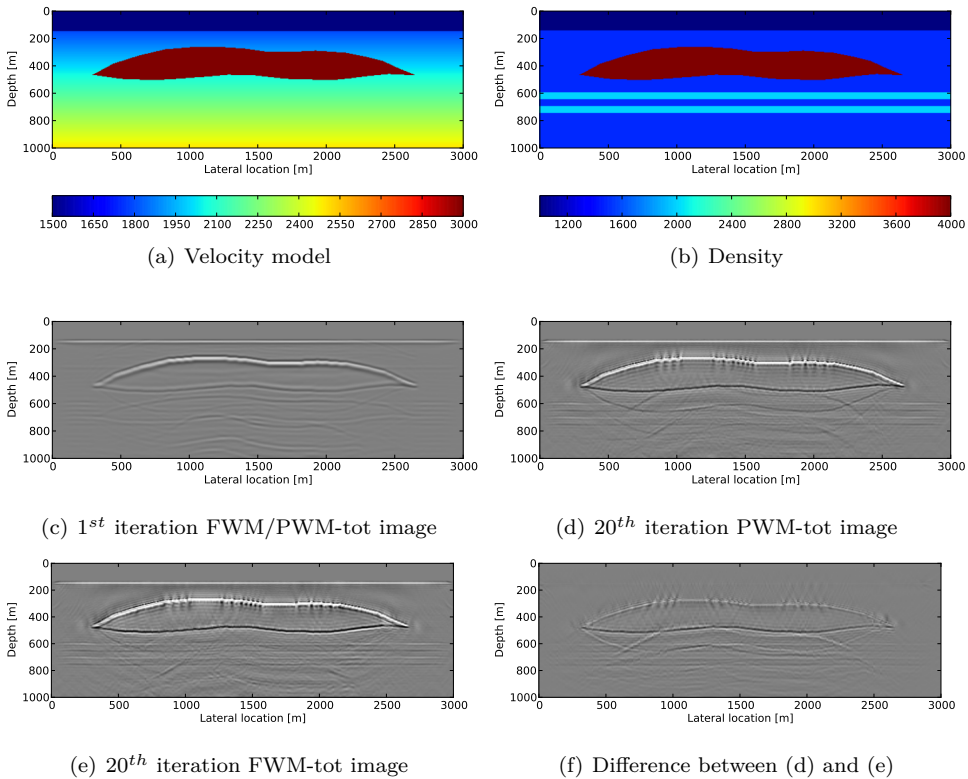


Figure 3.4: Example of FWM. a) Velocity model; b) Density model; c) Image at the 1st iteration; d) Image at the last iteration of PWM; e) Image at the last iteration of FWM; f) Difference between (d) and (e).

the forward model of PWM. The iterative process of FWM is able to successfully suppress this noise such that the target reflectors below the salt are clearly marked (see Figure 3.4e).

3.7.2 FWM applied to primaries and internal multiples

Next, we demonstrate options 2a and 2b from Table 5.1 by imaging primaries only. We assume that surface multiples have been perfectly removed in advance. It is clearly visible in Figure 3.6a that the target zone is still overwhelmed by the internal multiples caused by the salt body. The PWM image (Figure 3.6b) improves the image, however, it also contains spurious events that create via FWM false primaries that have the same travel times as the internal multiples and, therefore, mask the actual structure of the target area. However, when using FWM (Figure 3.6c) most internal multiples crosstalk is resolved and the target reflections can be well interpreted.

Figure 3.5 compares the image resulted by PWM (Figure 3.5a) and FWM (Figure 3.5b) for imaging primaries, one shot only. It is visible that when internal multiples and transmission are not taken into the account the shadow zone is quite visible (area is marked by the dashed rectangle). Internal multiples in FWM drastically increase the illumination and recover the shadow zone. Moreover, the amplitude is also corrected for transmission effects. Note that the horizontal target reflector of the multiple shots PWM image (Figure 3.6b) also show the effects of neglecting transmission.

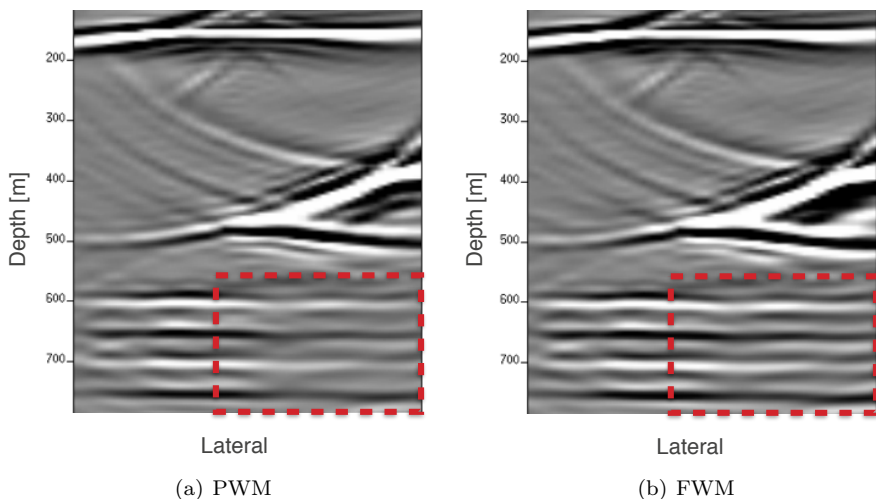


Figure 3.5: Comparison of PWM (a) and FWM (b) for one shot only. The image is zoomed at the left corner of the salt body (around $x=250m$).

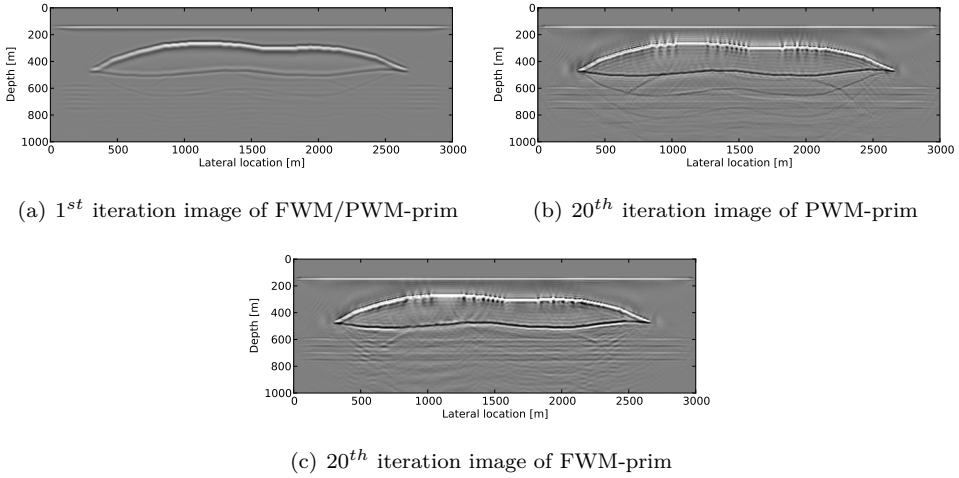


Figure 3.6: Imaging of primary wavefield including interbed multiples for the same model as in Figure 3.4. a) Image at the first iteration; b) PWM image at the 20th iteration; c) 20th iteration FWM image.

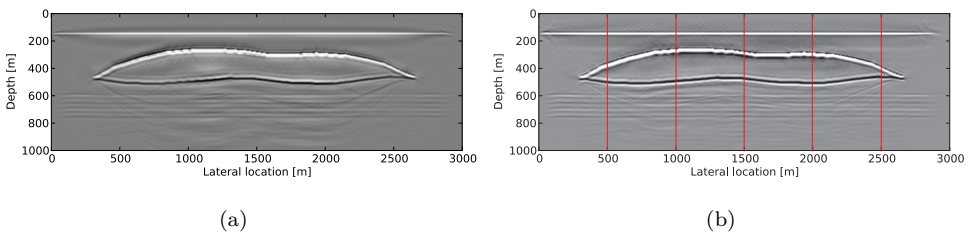


Figure 3.7: Comparison of FWM for large offset input data using a diagonal reflectivity operator (angle-independent approach) with FWM using the band-diagonal reflectivity operator (angle-dependent approach). a) Structural image; b) Angle-averaged image. The red lines show locations of the angle gathers from Figure 3.8.

Note that the results from Figure 3.6 are obtained by angle-independent imaging using only small-offset data (up to 700 meters in this example). Figure 3.7 demonstrates the comparison between the angle-independent and the angle-dependent approach when the full data aperture is considered. Figure 3.7a shows the structural image at the 20th iteration, while Figure 3.7 shows the angle-dependent image after summation all angle contributions. Figure 3.8 shows angle gathers resulting from angle-dependent imaging. Results at the first and the 20th iteration are compared in Figures 3.8(a,b), respectively. It is visible that the angle gathers after iterating have a better resolution and that most of the crosstalk (visible as curved events in the gathers) is suppressed.

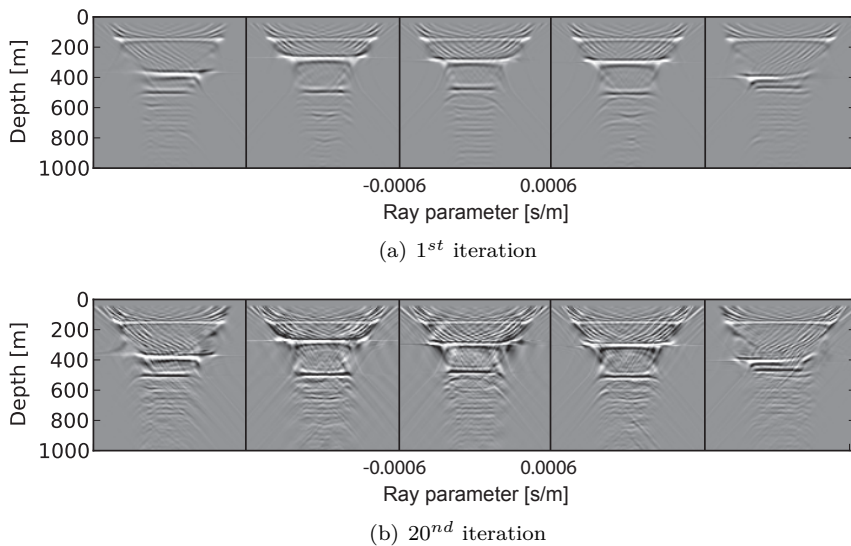


Figure 3.8: Angle-gathers at five lateral locations (50m, 100m, 150m, 200m and 250m) resulting from angle-dependent imaging. a) Result after the first iteration; b) Result after 20 FWM iterations.

3.7.3 FWM applied to surface multiples only

Another application is the imaging of surface multiples alone (options 3a and 3b from Table 3.1). This option is demonstrated on the same model shown in Figure 3.4a,b. For imaging of surface multiples only it is required to use re-injected measured data at the surface as the source-side wavefield and separated surface multiples at the receiver side. Such approach might be helpful for imaging shallow areas where surface multiples play a significant role in terms of illumination and angle coverage (Lu et al., 2014b).

The interesting feature of migrating the surface multiples is that the source wavelet information is not required. Only surface multiples (and their internal multiples)

are treated as useful information. Figure 3.9b shows the closed-loop imaging of the surface multiples without internal multiples included in the forward model. Figure 3.9c shows that the FWM approach on imaging of surface multiples also allows to suppress the resulting crosstalk from it's own internal multiples.

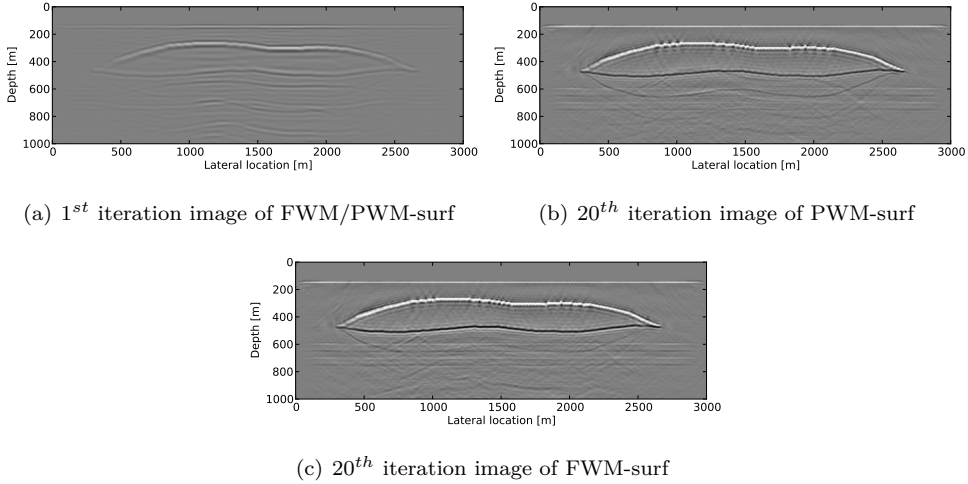


Figure 3.9: Imaging of surface multiples and their interbed multiples for the same model as in Figure 3.4. a) Image at the first iteration; b) PWM image at the 20th iteration; c) 20th iteration FWM image.

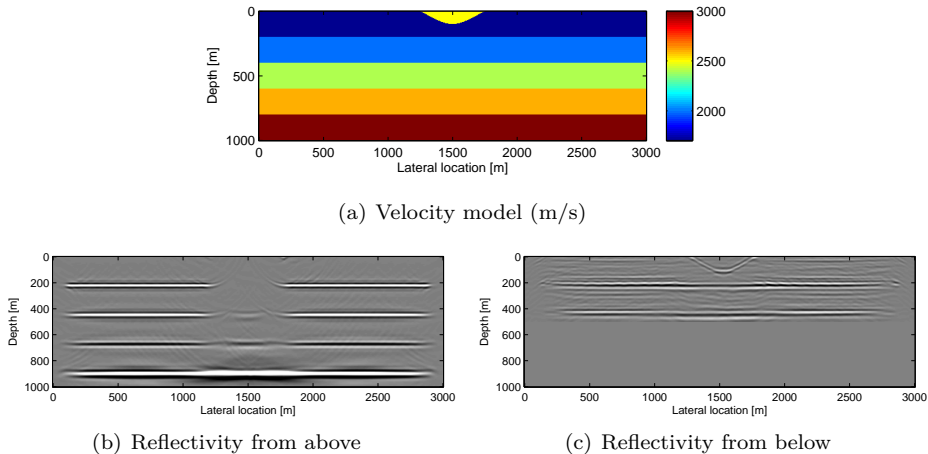
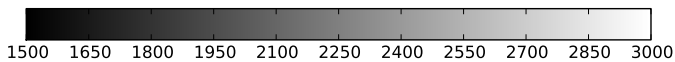
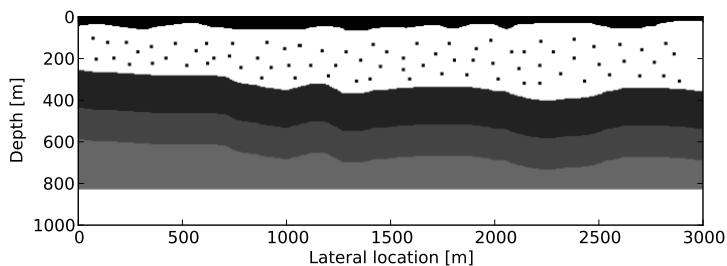


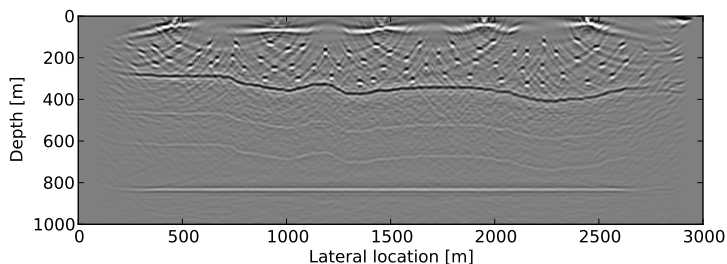
Figure 3.10: Internal multiples imaging example. a) Velocity model; b) Estimated reflectivity from above; c) Estimated reflectivity from below via the internal multiples.

3.7.4 Imaging of internal multiples with FWM

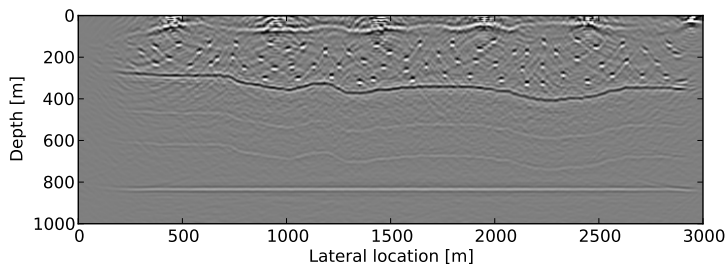
In the previous set of examples the reflectivity has been estimated from above and the reflectivity from below has been approximated as opposite polarity of the former one (i.e. $\mathbf{R}^\cap = -\mathbf{R}^\cup$). As it was discussed in the imaging section, the reflectivity from below can be estimated independently by imaging of internal multiples.



(a) Density kg/m^3



(b)



(c)

Figure 3.11: a) Density model. b) FWM image using the imaging condition from above. c) FWM based on joint ("from above" together with "from below") reflectivity estimation.

This will be demonstrated for the velocity model shown in Figure 3.10a. Sources and receivers are located at the surface but excluding the area between 1250m at 1700m (i.e. around the anomaly). Because of such acquisition gap the image obtained by imaging from above has an illumination hole that is visible in Figure 3.10b. Because internal multiples propagate with different ray paths and arrive at later times, they contain additional subsurface information. Figure 3.10c shows the image with the reflectivity from below estimated by internal multiples. Note the structure of the near-surface anomaly that is also well imaged. Moreover, one additional advantage of such approach is that the propagation velocity knowledge of the anomaly itself is not required, because the measured internal multiples don't propagate directly within this area, but only get reflected at the lower side.

Next, we consider the effect of coarse source sampling in Figure 3.11. The model contains a complex near surface and few strong reflectors beneath. The input data has sources every 500m, while receivers are densely sampled at the surface.

Figure 3.11 shows a comparison between imaging from below only (Figure 3.11b) and imaging using the combined imaging condition via Equation 3.27 (Figure 3.11c). Both images are the results after 10 iterations of FWM. Coarse source sampling creates illumination holes when imaged from above only. However, this gap can be infilled by information coming from internal multiples as they first propagate in the subsurface and, therefore, can reach different areas.

It is also visible that some of the diffractors are better imaged, which can be also explained by improved illumination from multiple angles by internal multiples.

3.7.5 3D extension of FWM

In this section the three dimensional extension of the FWM algorithm is demonstrated. The method is governed by the same equations, with the difference being that one extra dimension is included. As remarked earlier, all formulas as mentioned in this chapter can be used for both the 2D and full 3D case (see Kinneking et al. (1989)). However, the additional dimension opens various challenges that are discussed separately in Appendix C.

In the three dimensional case, each depth level represents a horizontal slice of the subsurface. The propagation is now performed by 2D spatial convolution operators in the x, y, ω domain. In case of a homogeneous velocity within a certain depth layer a simple phase shift operator can be applied in the frequency-wavenumber domain ($k_x - k_y - \omega$) in order to speed up the calculations. The additional challenge for 3D FWM is extra memory requirements, because FWM needs to save both upgoing wavefields at every grid-point of the subsurface. In order to reduce the memory requirement (numerical) source blending can be applied.

Our 3D example is based on the three-dimensional SEG EAGE salt model (Amnzadeh et al., 1994). The velocity model is shown in Figure 3.12 and represents a

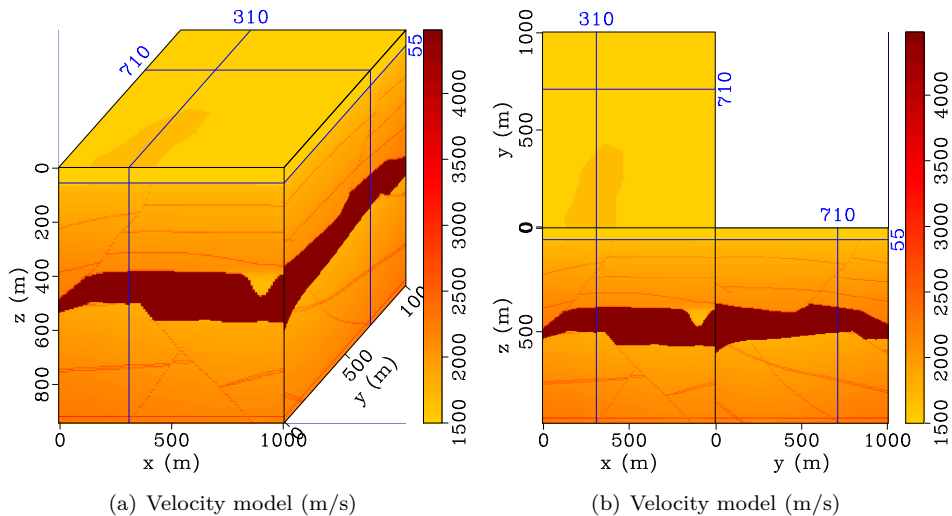


Figure 3.12: Middle cube of $1 \times 1 \times 1$ km selected from the 3D SEG EAGE salt model.

$1 \times 1 \times 1$ km subset of this 3D model. The density model is considered to be homogeneous. The grid size of the model is 5m and receivers are located at the surface on a regular grid of 20m spacing. In order to reduce computation time we blend shot records numerically: nine shot records include three blended sources each. The latter are randomly distributed at the surface such that the minimum distance between sources in each group is greater than 500m.

Figure 3.13a shows the image after the first iteration. It is visible that the image is weak in the lower part. Moreover, strong artifacts due to the blending (red arrows) are present in those images. Figure 3.13b demonstrates the advantages of the closed-loop imaging approach: after 15 iterations of the inversion process the blended crosstalk is largely suppressed and illumination is improved. Also note that the latter images have higher resolution, although those results are based on the conventional least-squares imaging approach that considers multiples as noise and involves primary-only illumination in the downgoing wavefield. Crosstalk from internal multiples is present (indicated by green arrows). Next, we show results of FWM after 15 iterations (Figure 3.13c), where the modeled wavefields were updated at every iteration by the estimated reflection coefficients. Differences between FWM and PWM are shown (at the same amplitude scale) in Figure 3.13d. It shows the amplitude enhancement in the lower half of the model, which is caused by the transmission effects and internal multiples included in FWM.

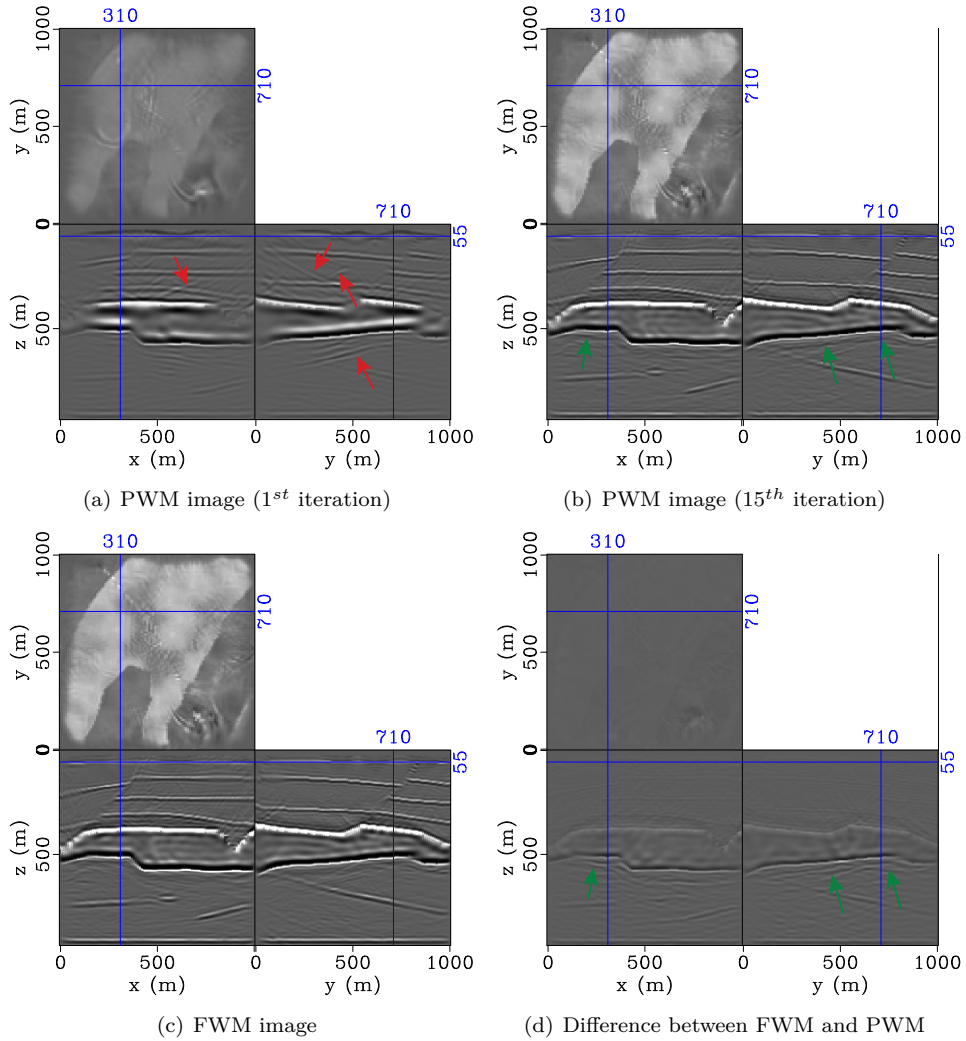


Figure 3.13: Example on the 3D SEG EAGE salt model. a) PWM image at the 1st iteration; b) PWM image at the 15th iteration; c) FWM image at the 15th iteration; d) Difference between b) and c), indicating the impact of internal multiples on the image.

3.8 Discussion

In this chapter it was shown that the imaging step within FWM provides a gradient computation for the descent algorithm that solves an inverse problem. As an inverse problem FWM has to address issues like parameterisation and solution uniqueness. It is required to constrain the reflectivity operator in order to avoid over-parameterisation. The most straightforward way is considering angle-independent reflection coefficients. Angle-dependent reflectivity, in its turn, has slightly more freedom and is obtained by estimating the angle gather per grid-point of the subsurface. However, this way might already be dangerous, because it gives an opportunity to explain the data in different ways (more discussion in Appendix B) and the final solution will be dependent on the initial model.

The demonstrated modelling and imaging methodology considers horizontal slicing of the subsurface (depth levels). At every grid-point of any arbitrary depth level the presence of a local, flat horizontal reflector is assumed. Between these levels the velocity model is assumed to be homogeneous.

Therefore, such approach is designed for waves travelling preferably in the vertical direction. However, there is also a strong interest to image vertical structures via waves traveling more horizontally. In the next chapter both modeling and imaging will be extended such that it will be possible to model horizontally propagating diving waves and scattered wavefields by including also horizontal wavefield extrapolation, both forward for modelling and backward for imaging.

It is also interesting to compare FWM with different imaging methods that address internal multiples. The method of Malcolm et al. (2009) may be considered as a predecessor of FWM. The downgoing and upgoing wavefields are also computed in the one-way manner. Two-way back-propagation is involved in the similar way. Internal multiples are also used for imaging the down-side reflectivity. However, the difference is in the iterative approach of FWM, whereas the first method is based on a 'single-step' migration (i.e. the first iteration of FWM). As shown in this chapter, the closed-loop (inversion) approach is important in order to obtain the best estimate of the reflectivity and suppress crosstalk.

The two-way method introduced by Fleury and Snieder (2012) incorporates internal multiples in RTM. In this method the scattered wavefield is computed using information based on the imaged reflectivity that comes from conventional RTM (that addresses the so-called reference wavefield). Therefore, it creates a non-linear relationship between the scattered data and the reflectivity. Four different imaging conditions are used such that each image requires the decomposition of the two-way reference and scattered wavefields into upgoing and downgoing components. This method is also not inversion-based.

Marchenko imaging (Broggini et al., 2013; Wapenaar et al., 2013) is based on the interferometric approach of recovering the Green's functions (upgoing and downgoing) that are used in the multiple-free imaging condition. The crosstalk is elegantly removed without applying a direct inversion approach. However, full two-way

Green's functions are estimated via an iterative process. Moreover, the method is target-oriented. It means that in order to image a specific subsurface point there is no need to resolve the whole subsurface as required by applying the Bremmer series (used in the FWMod approach). The main limitation of this method is in the acquisition requirements - source and receiver spacing should be dense - as this method is fully data-driven. This is in strong contrast to FWM, which can work pretty well with sparse sampling (see e.g. the 3D OBN data in Chapter 5). So you might say that the subsurface wavefields relationships act as a physical constraint in the inverse problem, such that acquisition requirements can be greatly reduced

3.9 Conclusions

In this chapter the imaging aspects of FWM has been discussed. It was shown that the main parameters of the model space (reflection and transmission both for the upgoing and downgoing direction) can be obtained by the corresponding gradient computations. The update for the reflectivity is a cross-correlation imaging condition of wavefields in opposite directions: the forward modeled incident wavefield and backward propagated residual wavefield. The update for the transmission effects is a cross-correlation of coinciding wavefields.

It is sufficient to estimate only the reflectivity from above and use it to express the rest of parameters. On the other side, it is possible to perform multi-parameter inversion of separate parameters with optional soft-constraints applied.

Various numerical examples showed the benefits of the approach of imaging using multiples: enhanced illumination by multiples (surface and internal) with the crosstalk – being an issue for conventional imaging methods – being suppressed.

4

Omnidirectional extension

As explained in the previous chapters, the machinery of the FWM algorithm is based on one-way wavefield extrapolation. The extrapolation in the wavenumber-frequency domain in a homogeneous medium is done by phase shift of plane waves (Berkhout, 1982):

$$\tilde{P}(z + \Delta z) = \tilde{P}(z) \exp^{-jk_z \Delta z}, \quad (4.1)$$

where, for the 2D case, $k_z = \sqrt{\omega^2 c^{-2} - k_x^2}$ and \tilde{P} represents a wavefield in the wavenumber-frequency domain. We can see that there is no propagation assuming $k_x^2 = \omega^2 c^{-2}$ (i.e. for 90 degree propagation angle). Therefore, one-way equation migration algorithms suffer from dip-limitation.

There are several ways to avoid such limitation. An interesting approach was proposed by Sava and Fomel (2005), in which the wavefield extrapolation is performed in the Riemannian coordinate system that conforms with main wavefield propagation direction. Such grid adjustment is performed using ray-tracing that, thereby, forms a skeleton of the grid. However, this grid will vary for different choices of source or receiver location. Another solution is to perform propagation in a tilted medium (Biondi and Shan, 2002).

In this chapter we investigate the idea of using a tilted medium for the extreme case of performing FWM additionally on an orthogonal grid. A similar approach, but for primaries only, is described in Xu and Jin (2007). In the modeling section it is discussed how it is possible to interchange scattering information between different grids. The imaging section describes the variety of imaging conditions that are used in this approach.

4.1 Omnidirectional modeling

The FWM forward model is based on the so-called wavefield relationship, as described in Berkhout (2012, 2014a) and in chapter 2 of this thesis. According to the already established version of the algorithm, the depth level can be approached from above by the downgoing wavefield \mathbf{P}^+ and it can be approached from below by the upgoing wavefield \mathbf{P}^- .

When the modeling is performed in an orthogonal direction, the corresponding wavefield relationship takes place for left-going and right-going wavefields. Note that the same relationships between total and incoming wavefields are valid.

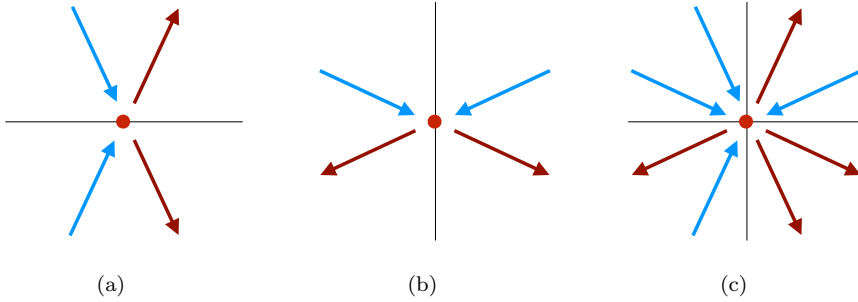


Figure 4.1: Full wavefield relationships for (a) the vertical propagation case, (b) the horizontal propagation case and (c) the total propagation case.

The corresponding set of equations can be written as:

$$\begin{aligned}
 \mathbf{Q}^+(z_m) &= \mathbf{P}^+(z_m) + \delta\mathbf{S}(z_m) \\
 \mathbf{Q}^-(z_m) &= \mathbf{P}^-(z_m) + \delta\mathbf{S}(z_m) \\
 \mathbf{Q}^+(x_m) &= \mathbf{P}^+(x_m) + \delta\mathbf{S}(x_m) \\
 \mathbf{Q}^-(x_m) &= \mathbf{P}^-(x_m) + \delta\mathbf{S}(x_m).
 \end{aligned} \tag{4.2}$$

Note that depth level indication (z_m) indicates the horizontal depth level, while x_m considers a vertical screen for wave propagation.

In contrast to the single-direction wave propagation, the scattering term not only contains upgoing wavefields and downgoing wavefields multiplied with the corresponding reflectivity operator, but it also contains the contribution from the orthogonal component:

$$\delta S_{nm} = [\vec{P}^u(z_m)]_n + [\vec{P}^r(z_m)]_n + [\vec{P}^u(x_n)]_m + [\vec{P}^r(x_n)]_m, \tag{4.3}$$

where:

$$\begin{aligned}
\vec{P}^{\cup}(z_m) &= \mathbf{R}^{\cup}(z_m)\vec{P}^+(z_m) \\
\vec{P}^{\cap}(z_m) &= \mathbf{R}^{\cap}(z_m)\vec{P}^-(z_m) \\
\vec{P}^{\cup}(x_m) &= \mathbf{R}^{\cup}(x_m)\vec{P}^+(x_m) \\
\vec{P}^{\cap}(x_m) &= \mathbf{R}^{\cap}(x_m)\vec{P}^-(x_m).
\end{aligned} \tag{4.4}$$

With the aid of Equation 4.3 it is possible to interchange the scattering between the vertical and the horizontal wavefields. In this way, it basically means that $\delta\mathbf{S}$ does not just describes the two-way scattering, but an omnidirectional source (like a monopole).

However, in this implementation the information interchange between the orthogonal coordinate systems can be done only via scattering. For example, it cannot accommodate complete turning waves as they transform from vertical to horizontal wavefields without scattering.

According to Equations 4.2, 4.3 and 4.4, the modeling can be performed as a sequence of forward one-way propagations into two opposite directions (both vertical and horizontal), while including the potential scattering $\delta\mathbf{P}$ at any passing screen level (z_m or x_m). Note, that it is required to save all wavefields \mathbf{P} in order to recursively recompute $\delta\mathbf{S}$, which will be used again in the next modeling iteration. Thus, every modeling iteration will create an additional order of scattering in the modeled data. Finally, the general modeling equation can be written as follows:

$$\begin{aligned}
\mathbf{P}^+(z_m) &= \sum_{s < m} \mathbf{W}^+(z_m)\mathbf{S}(z_s) + \sum_{n < m} \mathbf{W}^+(z_m, z_n)\delta\mathbf{S}(z_n) \\
\mathbf{P}^-(z_m) &= \sum_{s > m} \mathbf{W}^-(z_m)\mathbf{S}(z_s) + \sum_{n > m} \mathbf{W}^-(z_m, z_n)\delta\mathbf{S}(z_n) \\
\mathbf{P}^+(x_m) &= \sum_{s > m} \mathbf{W}^+(x_m)\mathbf{S}(x_s) + \sum_{n > m} \mathbf{W}^+(x_m, x_n)\delta\mathbf{S}(x_n) \\
\mathbf{P}^-(x_m) &= \sum_{s < m} \mathbf{W}^-(x_m)\mathbf{S}(x_s) + \sum_{n < m} \mathbf{W}^-(x_m, x_n)\delta\mathbf{S}(x_n).
\end{aligned} \tag{4.5}$$

Note that the first term on the right hand side of each sub-equation is only non-zero for physical sources at z_s or x_s . Due to the combined propagation in both spatial dimensions some angles of propagation (around 45 degrees) can be present on both wavefield components. This can lead to over-amplifying the total wavefield, because our omnidirectional extension is mostly based on physical intuition.

4.2 Omnidirectional imaging

As it was mentioned before, FWM aims at explaining the observed reflection data by the modeled one. The objective function describes a misfit (to be minimised) between the observed and the modeled data, but now the last one comprises vertical and horizontal components, as described in Equation 4.5. Also note that in principle

the method has no limitation in source/receiver positioning and can, for example, be suitable for VSP data (El-Marhoul and Verschuur, 2014).

In the current setup the both vertically and horizontally modeled data is influenced by the horizontal reflectivities $\mathbf{R}^{\cup}(x_m)$ and $\mathbf{R}^{\cap}(x_m)$ as well. Therefore, the full set of gradients will be as following:

$$\begin{aligned}\Delta\mathbf{R}^{\cup}(z_m) &= [\Delta\mathbf{P}^-(z_m)][\mathbf{P}^+(z_m)]^H \\ \Delta\mathbf{R}^{\cap}(z_m) &= [\Delta\mathbf{P}^+(z_m)][\mathbf{P}^-(z_m)]^H \\ \Delta\mathbf{R}^{\cup}(x_m) &= [\Delta\mathbf{P}^-(x_m)][\mathbf{P}^+(x_m)]^H \\ \Delta\mathbf{R}^{\cap}(x_m) &= [\Delta\mathbf{P}^+(x_m)][\mathbf{P}^-(x_m)]^H.\end{aligned}\tag{4.6}$$

Next, the reflectivities are updated at each iteration:

$$\begin{aligned}\mathbf{R}_{i+1}^{\cup}(z_m) &= \mathbf{R}_i^{\cup}(z_m) + \alpha[\Delta\mathbf{R}_i^{\cup}(z_m) - \Delta\mathbf{R}_i^{\cap}(z_m)] \\ \mathbf{R}_{i+1}^{\cup}(x_m) &= \mathbf{R}_i^{\cup}(x_m) + \beta[\Delta\mathbf{R}_i^{\cup}(x_m) - \Delta\mathbf{R}_i^{\cap}(x_m)] \\ \mathbf{R}_{i+1}^{\cap}(z_m) &= -\mathbf{R}_{i+1}^{\cup}(z_m) \\ \mathbf{R}_{i+1}^{\cap}(x_m) &= -\mathbf{R}_{i+1}^{\cup}(x_m),\end{aligned}\tag{4.7}$$

where α and β are scalar values that are computed as described in Section 3.4. Thus, the main loop of FWM is based on imaging the residual wavefield, updating the reflectivity, subsequent forward modeling, scaling the reflectivity update and recalculating the residual wavefield, etc. In the next section, this process will be demonstrated based on a few basic examples.

4.3 Examples

4.3.1 Dipping structure example

The first imaging example is based on a simple model with one flexure-like reflector that is shown in Figures 4.2a,b,c. Figure 4.2a shows the reflectivity estimated in the vertical direction only. Note that in the estimated image, the amplitude of the dipping reflector is weaker. This can be explained, because the other part of the amplitude is contributed to the image estimated by the horizontal propagation (Figure 4.2b). In Figure 4.2c the sum of the images is shown, where it is visible that the amplitude of the reflector is now corrected along the full reflector. The finite-difference modeling snapshot of the wavefield with the source located at the surface, at $x=1500\text{m}$, is shown in Figure 4.2d. The snapshot of the one-directional FWM modeling scheme is shown in the middle plot (Figure 4.2e). The lack of amplitudes corresponding to the horizontal propagation is clearly visible. The right plot (Figure 4.2f) demonstrates the data modelling via omni-directional FWMod (using Equations 4.5), which is very close to the results of finite-difference modeling.

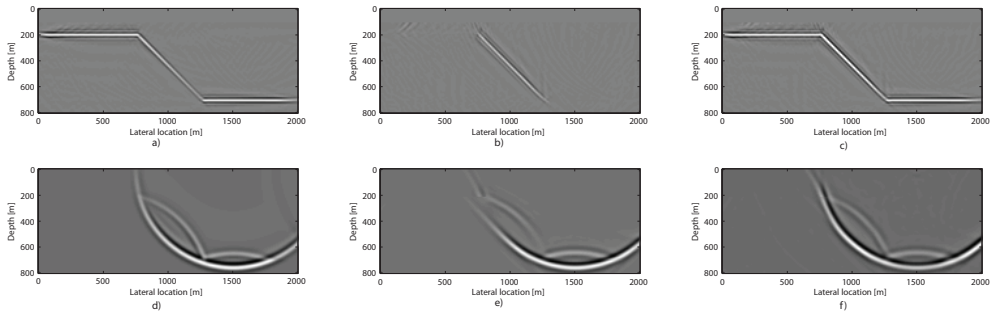


Figure 4.2: Imaging results of the omnidirectional FWM version: a) vertical reflectivity, b) horizontal reflectivity and c) combined one. Modeling results: d) finite-difference wavefield snapshot of the source located at the surface at $x=1500\text{m}$, e) same snapshot by standard FWM, f) snapshot of the extended FWM version.

4.3.2 Vertical anomaly example

The second example of the extended FWM scheme is demonstrated using the model shown in Figure 4.3. The velocity model is represented by an increasing velocity according to a linear gradient towards the depth axis, while it is laterally invariant. The geological vertical structure is represented by density variations only. Figure 4.3c demonstrates the total image (superposition of both vertical and horizontal estimated reflectivities) at the first iteration. Note that crosstalk from the horizontally propagating internal multiple can be observed. Figure 4.3d shows the omnidirectional FWM image after the fifth iteration. Note that the resolution has improved and that the crosstalk has been largely resolved. Figure 4.3e displays the snapshot of the total wavefield calculated by omnidirectional FWM, which can be well compared with the result achieved by finite-difference modelling (Figure 4.3f). Note that the boundaries in the finite-difference modeling (Figure 4.3f) are not fully absorbing.

4.3.3 Duplex waves imaging by horizontal modeling

This section studies the possibility to include so-called duplex waves (or prismatic waves) into the modelling and imaging process. Such waves can be basically classified as internal multiples that scatter only twice within the subsurface.

It was shown (Marmalyevskyy et al., 2005; Zhang et al., 2006; Xu and Jin, 2007) that duplex wave imaging can be formulated as an extension of the one-way migration methods to image vertical structures. It involves the reflected upgoing wavefields $\mathbf{P}^-(z_m, z_0)$ (basically, the first roundtrip of omni-directional FWM modeling) at the source-side, whereas the receiver wavefield is the again the back-propagated measured wavefield. In other words, the reflectivity is estimated for waves that are initially reflected at a horizontally oriented structure and then approach the vertical

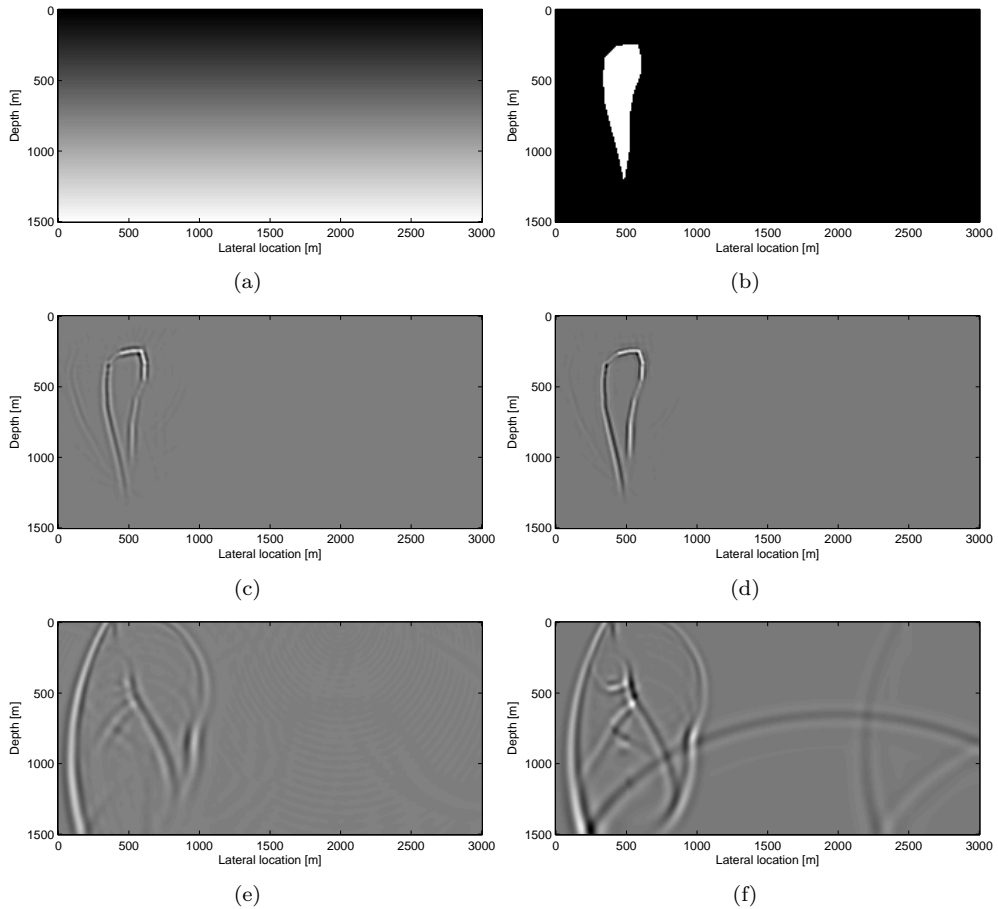


Figure 4.3: Example of omnidirectional FWM. a) Velocity model represented by a positive linear vertical gradient; b) Density model, including a vertically structured anomaly; c) Total image at the first iteration (note the artifact from the vertically oriented internal multiple); d) Total image at the fifth iteration, where crosstalk has been suppressed; e) snapshot of the total (all directions) FWM wavefield at 1.12ms; f) snapshot of the wavefield computed by finite-difference modeling.

one. The imaging condition is applied to this last reflection.

The example shown in Figure 4.4 demonstrates how duplex imaging is automatically incorporated in the omnidirectional extension of FWM. Figure 4.4a shows the result of the vertical-only FWM. Modeled wavefields at 0.68s and 0.96s are shown respectively in Figures 4.4d,e. It is visible that the estimated reflectivity has a lacking vertical structure and modeled wavefields do not completely model the prismatic reflection (with the first bounce at the lower horizontal boundary and the second bounce at the vertical boundary, or vice versa). However, the omnidirectional ex-

tension overcomes this problem (Figure 4.4f,g.)

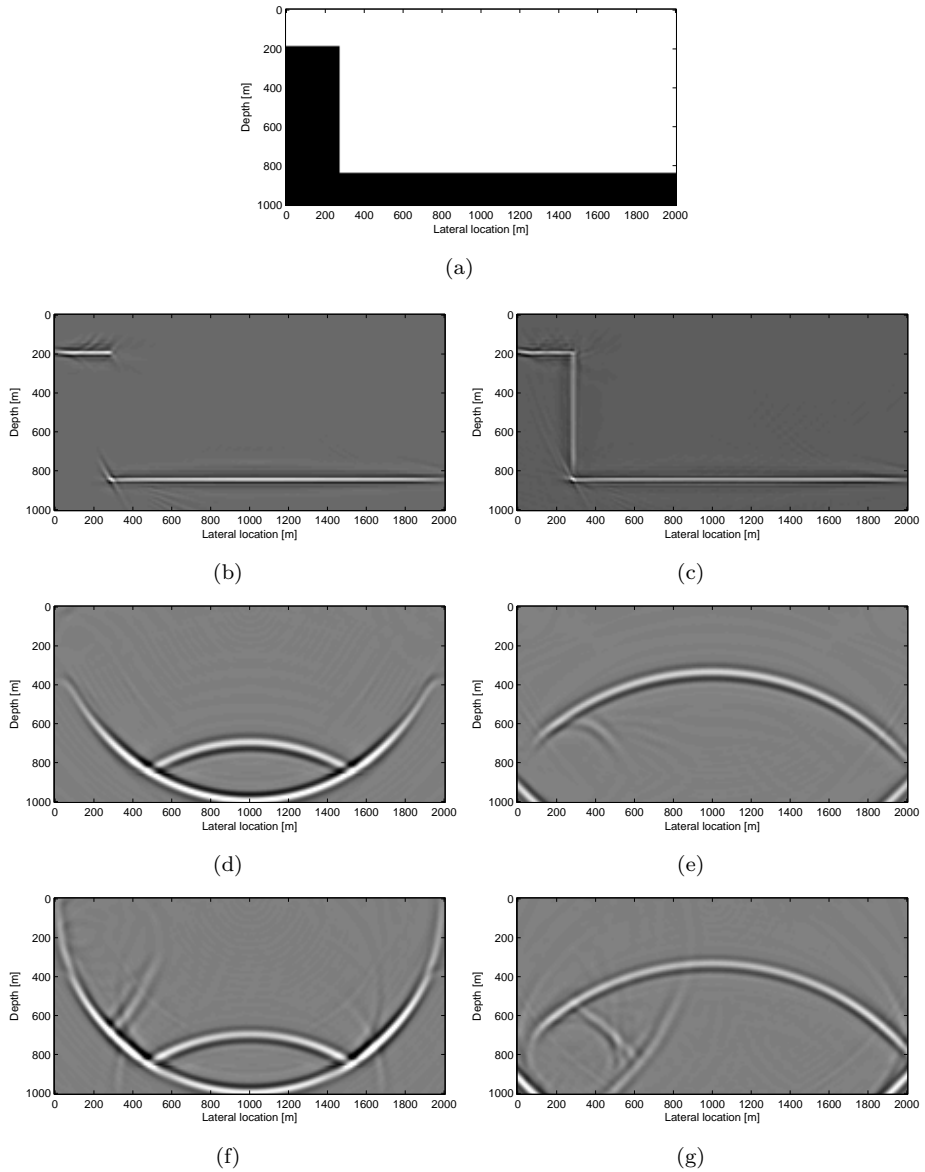


Figure 4.4: Example of duplex wave imaging. a) Density model; b) Image in the vertical FWM mode; c) Image obtained via the omnidirectional FWM mode; d) vertical FWM mode wavefield snapshot at 0.68s and (e) at 0.96s; f) omnidirectional FWM mode wavefield snapshot at 0.68s and (g) and at 0.96s.

4.3.4 Salt model example

A geologically more realistic example is demonstrated on the BP 2004 Benchmark model (Billette and Brandsberg-Dahl, 2005). Velocity and density models are shown in Figures 4.5a,b, respectively. Figure 4.5c shows the FWM image in the vertical mode: the vertical flank of the salt body is not imaged because of diving waves that are missing in the conventional FWMod (down and up only). Omnidirectional FWM is able to include the vertical flank of the salt body (Figure 4.3d). Note the artifacts located in the shallow part (above the first reflector) that are especially visible in the area around each source position. Additional muting of the reflectivity close to the source location can be used to avoid such artifacts.

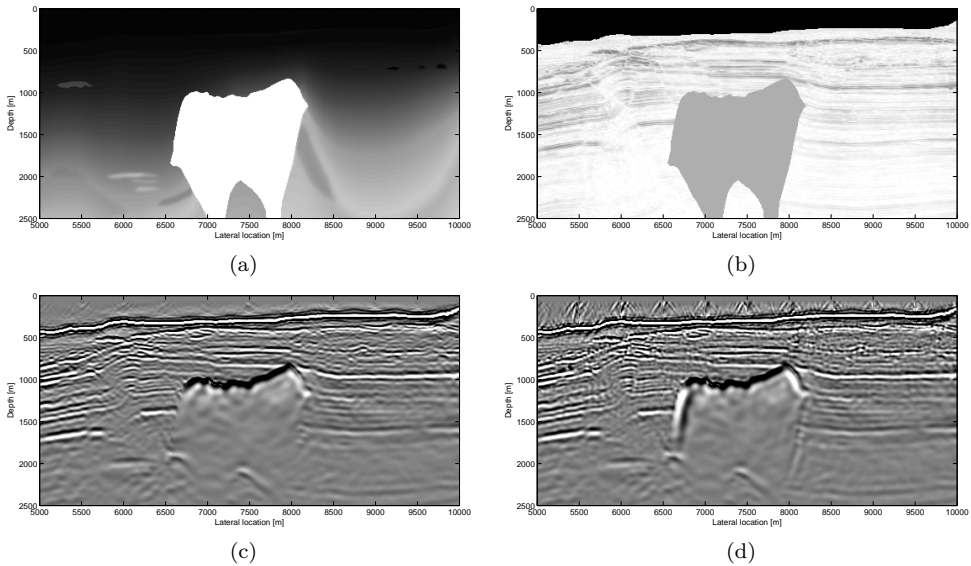


Figure 4.5: Example based on BP 2004 Benchmark model. a) Velocity model; b) Density model; c) FWM image (vertical mode); d) FWM image (omnidirectional mode).

4.4 Discussion

It was shown that the full wavefield modeling can be performed separately in two orthogonal directions in order to compensate for emphasizing only one preferred direction and, therefore, losing the accuracy in the orthogonal one. The current approach allows wavefields from orthogonal directions to intercommunicate via the scattering term $\delta\mathbf{S}$.

Note that the approach discussed in this chapter needs to be extended to the three dimensional case. For instance, in addition to up/down, two horizontal North/South

and West/East round-trips need to be applied.

Also note that, as mentioned in Wapenaar and Grimbergen (1996), in theory the lateral variations of the medium must be taken into account by the propagation operator. In such description, the \mathbf{W} operator does not only contain propagation effects but it also includes scattering in the direction coincident to the propagation. However, such description requires an accurate density and velocity model of the subsurface, like used in FD modelling. However, in this chapter we followed a different path by assuming the horizontal horizontal reflectivity as a separate operator in the orthogonal grid, such that a more data-driven approach can be utilized.

We have shown in this chapter that the horizontal reflectivity is able to scatter the horizontal wavefield omitting the duplex waves in the vertical component. However, as mentioned in the previous chapter, imaging of transmission coefficients can capture such information from the vertical component. Figure 4.6a shows the reflectivity estimated in the vertical sense, whereas Figure 4.6b shows the estimated upgoing transmission part where we can see not only the horizontal part of the image but also the vertical boundary. Therefore, the most complete approach would be estimation of the transmission coefficients independently rather than constraining it by reflectivity that lacks imaging vertical structures. However, this option is not yet fully investigated due to the artifacts and difficulties appearing during cross-correlation of the source-side and receiver-side wavefields from the same direction.

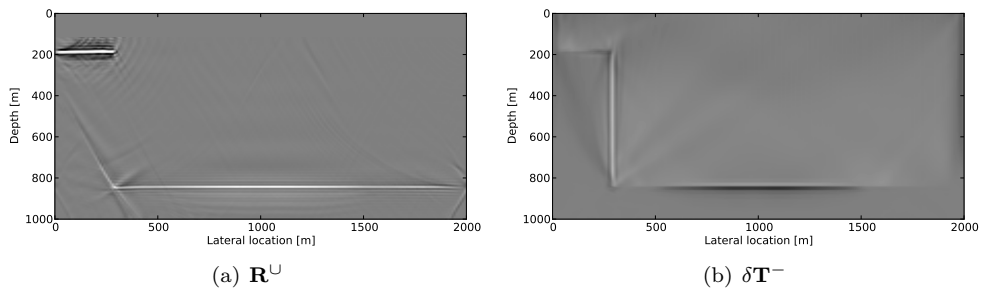


Figure 4.6: FWM applied in the vertical mode with estimation of the upgoing transmission as independent parameter. a) Estimated reflectivity \mathbf{R}^U ; b) Estimated upgoing transmission part $\delta\mathbf{T}^-$.

4.5 Conclusions

An omnidirectional extension of Full Wavefield Migration has been proposed, where one-way wave propagation in the vertical and in the horizontal direction is combined such that reflectivity under all angles can be properly estimated. Four synthetic examples showed the virtues of this extended FWM algorithm.

However, the wavefields at some angles are presented on both components, yielding

the danger of over-parametrisation. Therefore, the wavefields possibly should be filtered. Some further research is required to properly represent the wavefields at all angles.

5

Applications

5.1 Introduction

This chapter demonstrates various application options and strategies that are possible via FWM and full wavefield modelling (FWMod).

In Chapter 3 different imaging input options were already introduced. In the next section imaging of surface multiples and its various modifications will be described. It will be shown that imaging of surface multiples will increase the illumination and may drastically improve the image quality especially in cases of coarse source or receiver sampling. The latter is discussed in the OBN imaging subsection.

When imaging surface multiples, the original source wavelet is not required as the measured wavefield is reinjected at the surface and is used as a source wavefield. This feature can be used for the actual source estimation by running FWMod in a time-reverse (adjoint) mode, which translates primaries into the source wavelet. A special section demonstrates the source estimation approach.

Finally, it is demonstrated how to apply missing data reconstruction and deblending using FWMod.

5.2 Imaging surface multiples

Imaging of surface multiples has been already introduced in Chapter 3. In this section we will demonstrate the benefits of this approach. Surface multiples allow

to image the subsurface without actual knowledge of the source wavelet, whereas knowledge of the source wavelet is necessary when imaging primaries. Previously, it was discussed that FWM can be applied to different types of data: depending on the choice of the source-side wavefield that is used, primaries, surface multiples or total data can be imaged. The options are gathered again in Table 5.1. In particular, surface multiples for the marine case can be generated after re-injection of the measured data multiplied by the surface reflection coefficient.

As mentioned before in Chapter 3, that there are two possibilities to model the surface multiples. In the first, linear way, the source wavefield at the surface is taken as $\vec{Q}^+(z_0) = \vec{S}^+(z_0) + \mathbf{R}(z_0)\vec{P}_{obs}^-(z_0)$, i.e. as a superposition of the wavelet and the re-injected observed wavefield, meaning that re-injected measured data takes one extra roundtrip through the subsurface. Thus, the last bounce of each event is used in the imaging process. Surface multiples, in this case, would have the same sensitivity to the velocity model errors possibly present. You could say that the wavefield relationship at the surface is passive, because multiples are included by adding the measured data in the source term.

Table 5.1: Three imaging options in the FWM process.

Options	Source side	Receiver side
1) FWM-tot	$\vec{S}^+ + \mathbf{R}^\cap(z_0)\vec{P}^-$	\vec{P}^-
2) FWM-prim	\vec{S}^+	\vec{P}_0^-
3) FWM-surf	$\mathbf{R}^\cap(z_0)\vec{P}^-$	\vec{M}^-

Another, non-linear way, is to model surface multiples via active wavefield relationship at the surface, starting from the original source wavelet. It means that the total downgoing wavefield is actually $\mathbf{Q}^+(z_0) = \mathbf{S}^+(z_0) + \mathbf{R}(z_0)\mathbf{P}_{mod}^-(z_0)$, being the source wavelet and the re-injected modelled data (generated with FWM_{Mod}). In this case, the knowledge of the source wavelet is required in order to generate the surface multiples.

In most cases we do the first, linear, option, especially because then surface multiples are correctly imaged even without knowledge of the source wavelet. Moreover, it has a better convergence rate: the surface multiples are started being explained already at the second iteration (right after the first estimate of the reflectivity obtained at the first iteration). The second option might be very useful for estimating velocities with high resolution in Joint Migration Inversion (JMI) (Berkhout, 2014c; Staal et al., 2014) or when there are large acquisition gaps.

Figure 5.1 compares the imaging result of primaries on the model shown in Figure 3.4, which was also used in the previous chapter. The source spacing has been slightly increased from 50m to 100m. In Figures 5.1a,b,c the AVP functions selected at the depth level of the first horizontal reflector are shown for primaries, surface multiples and total data, respectively. Figures 5.1d,e,f show corresponding angle-averaged reflectivity plots. The acquisition imprint is strong and clearly visible (see Figure 5.1a) as gaps with a period matching the source sampling. By looking

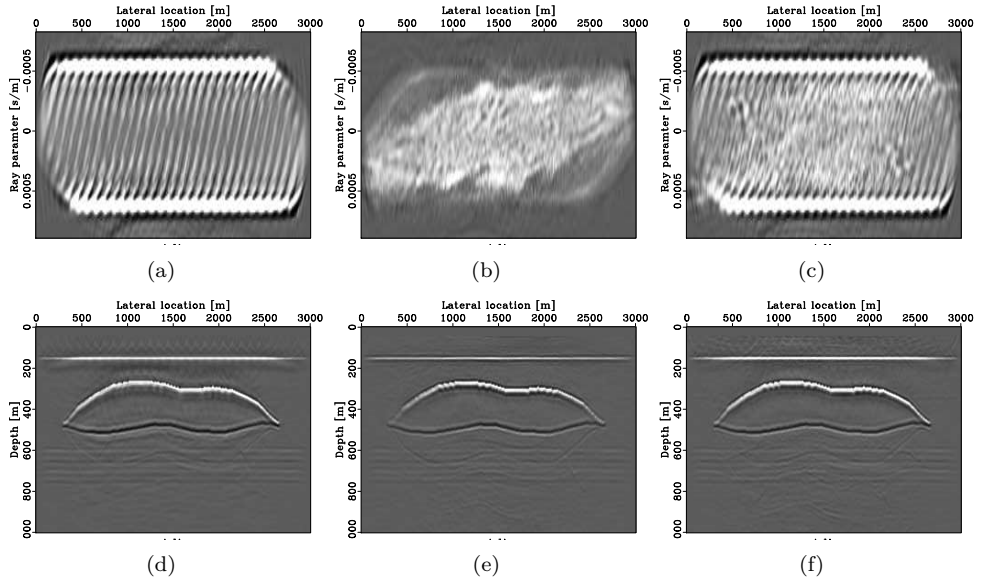


Figure 5.1: Angle-dependent imaging of primary data: AVP plot (a) and angle-averaged image (d); imaging of surface multiples only: AVP plot (b) and angle-averaged image (e) and imaging of the total data: AVP plot (c) and angle-averaged data.

at Figure 5.1b it is visible that imaging of surface multiples does not have such strong acquisition imprint and illuminates all angles for all lateral locations more or less homogeneously. This can be explained as the surface detectors act as secondary sources, reflecting all upgoing energy and, thereby, generate additional illuminations. Imaging of surface multiples might be very useful for detecting shallow structures (see Lu et al. (2014b)). Imaging of the total wavefield uses both information from the surface multiples and the primaries. However, it is clearly visible that information coming from the primaries overwhelms the contribution from the surface multiples, such that a residual acquisition imprint remains visible (Figure 5.1c).

5.3 Joint primaries and surface multiples imaging

Given the observations in the previous section, it is interesting to consider joint-FWM when two datasets (primaries and surface multiples) are being inverted via a closed-loop process separately, while their image is connected. The strategy can be described as follows:

1. Total data imaging. FWM for the first option from Table 5.1 is performed.
2. Prediction of surface multiples and primaries. Wavefields are predicted using FWMod based on the reflectivity obtained at the previous step. The predicted

wavefields are subtracted from the total data: the modeled primaries are subtracted from the total data in order to achieve an estimate of surface multiples a subtraction of the modeled surface multiples is used to calculate an estimate of the primaries. Thereby, the separation is performed (see also Section 5.7).

3. Joint primary/surface multiples FWM. In the last step separated wavefields are inverted independently, while updating and using the joint (combined) image that aims at explaining both wavefields simultaneously. Weighted sum of the separated images can be applied in order to calculate a total image.

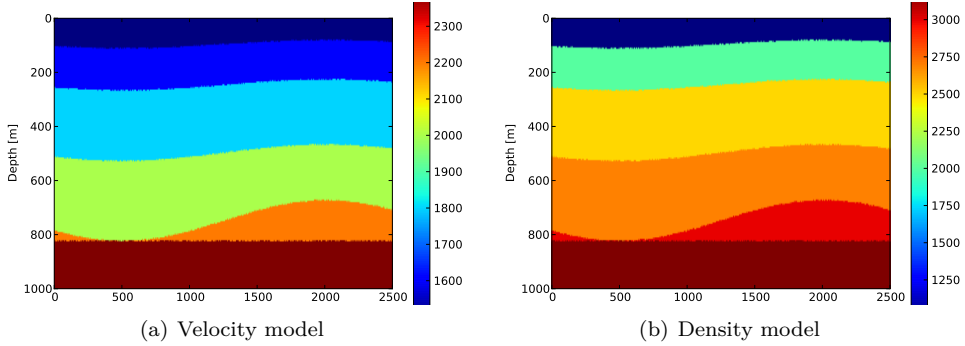


Figure 5.2: Velocity model (a) and density model (b) used to generate numerical data using acoustic finite difference modelling.

We study this approach on a numerical example. Figure 5.2 shows the velocity and density model used for acoustic finite-difference modelling in order to generate the total reflection data (one of the experiments is shown in Figure 5.4a). Sampling of the sources is 350m and the receivers are sampled with 10m. Note that Gaussian noise has been added to the generated wavefields.

First we image the total data. The resulting image after 20 iterations is shown in Figure 5.3a. The image is good (crosstalk has been successfully suppressed), however, due to the coarse source sampling (350m) the first reflector has an acquisition imprint. Next, we use the reflectivity from this result in order to model primaries and surface multiples using FWM. The resulting modelled primaries and surface multiples are subtracted from the given total data in order to estimate surface multiples and primaries, respectively, from the total data. The resulting datasets are shown in Figure 5.4b and c, respectively.

The FWM images for separated primaries and surface multiples are shown in Figure 5.3c and d. It is visible that the image of the primaries has an acquisition imprint as well in the shallow part, whereas the image of the surface multiples is better in this area. However, the surface-multiples image is more noisy in the deeper part.

Finally, we apply the proposed joint imaging process (see Figure 5.3b). The joint image was combined such that above 300 meters the surface multiples imaging con-

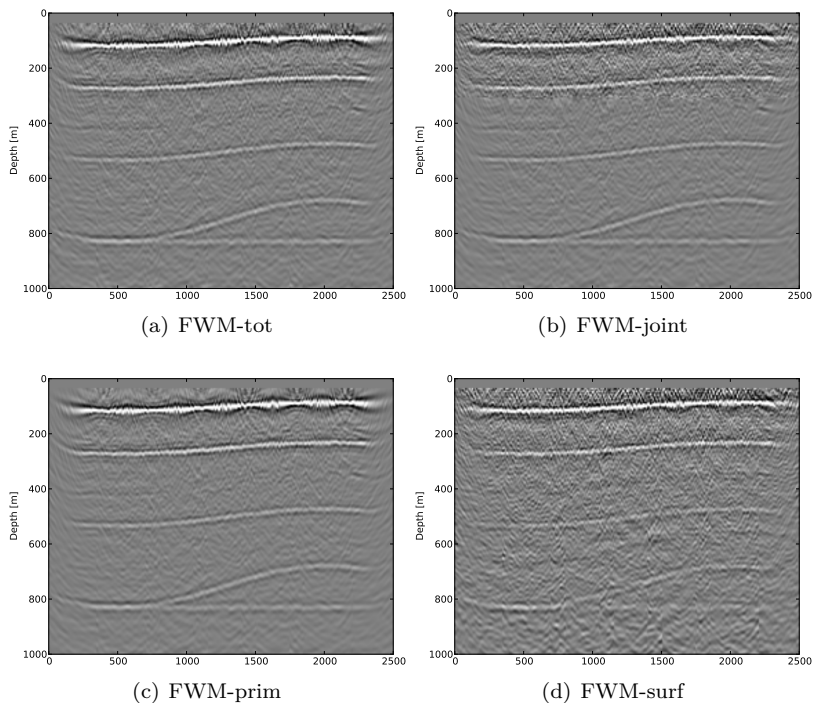


Figure 5.3: a) Total wavefield FWM image, b) joint FWM image, c) separated primary FWM image and d) separated surface multiples FWM image.

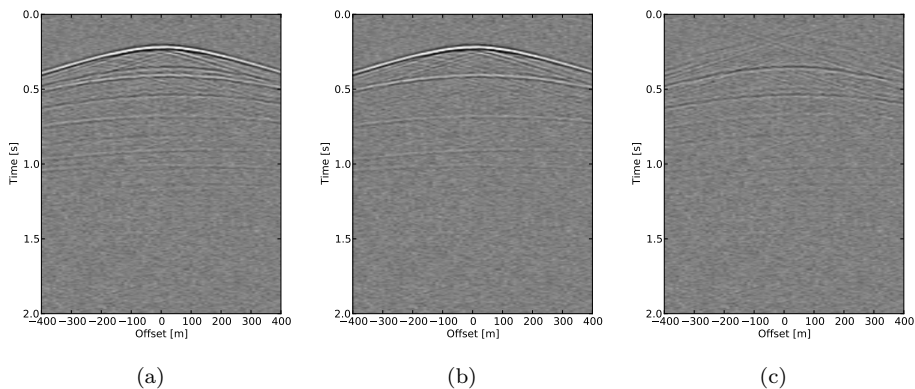


Figure 5.4: Wavefield separation results via FWM. a) Total data, b) Separated primaries by using FWMod and c) Separated surface multiples by using FWMod.

dition was used, whereas beneath the primary imaging was involved. Note, that the shallow area now has no acquisition imprint and there is slightly improved resolution

in comparison to the surface multiples image at the shallow part (Figure 5.3d). At the deeper part this image is made up of the primary image that takes the advantage over the noisy result coming from Figure 5.3d.

In this example a straightforward separation between the contribution of multiples ($z < 300$) and primaries ($z > 300$) was used. Of course, more advanced weighting schemes and additional constraints can be used for potentially better results.

5.4 Ocean bottom node imaging

Another important application of imaging surface multiples is the ocean bottom node (OBN) acquisition. OBN becomes a common acquisition method (Mitchell et al., 2010). Because of various practical and economic constraints the distance between two nodes can be in the order of a few hundred meters in both spatial directions. Due to the sparse receiver sampling the acquisition design should be compensated by dense source sampling at the surface. In the reciprocal domain several common receiver gathers can represent shot records – with sources on the ocean floor – with well-sampled receivers at the surface. Because the number of shot-records is small and the source (in the reciprocal domain) is located close to the water bottom, imaging of primaries becomes difficult, especially close to the water bottom. However, the data is very suitable for using surface multiples to image the subsurface. Usually this is done via the mirror source principle. This will only allow the imaging of first-order multiples, while it can create crosstalk from other events. In this section we describe the capability of FWM to image OBN data in a more complete sense.

Figure 5.5 shows the mentioned options. It is visible that imaging of primaries is limited to an area around each ocean bottom node (Figure 5.5a), whereas imaging via the mirror source and surface multiples (Figure 5.5b,c) drastically increases illumination.

In previous publications a so-called mirror imaging is applied. In this case a source-wavelet is forward propagated to the depth twice deeper than the actual OBN station, which makes it possible to image surface multiples (Figure 5.5b) of the first order. This approach works well in the case of a deep water bottom, as then separation of primaries and surface multiples is guaranteed (Pacal et al., 2015). Wong et al. (2012) demonstrated that the mirror imaging technique can be enhanced by the joint inversion-based imaging approach with surface seismic data.

Lecerf et al. (2015) showed the advantage of using all surface multiples over the mirror source imaging process – every additional order of surface multiple brings additional information about the subsurface (instead of using only the first order). Using the same reasoning FWM also uses all orders of surface multiples but at the same time it also includes transmission effects and interbed multiples. Thus, a physically more correct forward model, in combination with the closed-loop approach,

allows to use the information from all reflection events (see Figure 5.5c) and to suppress the crosstalk.

Next, a numerical example demonstrates the three described approaches of OBN imaging, starting with imaging primaries, then using mirror source imaging and, finally, imaging the full wavefield (excepting primaries). The velocity and density models for this set of examples are shown in Figures 5.6a,b respectively. The data was modeled using finite-difference modelling with an OBN configuration: a dense regular source distribution at the surface with a sparse set of the receivers (ocean bottom nodes) measuring the components of the particle velocity and the pressure, which can provide up/down wavefield separation by PZ summation. Because of sparse source sampling (150m) it is important to mention that multiple elimination in this situation is challenging such that imaging of multiples provides a great alternative: it works on a shot basis and multiples will largely enhance the illumination.

Four imaging approaches have been performed on these data: imaging of primaries (Figure 5.6c), closed-loop mirror source imaging (Figure 5.6d) and surface multiples imaging using PWM (Figure 5.6e) and FWM (Figure 5.6f). All steps were carried out in the reciprocal domain considering sources at the water bottom with a dense receiver array located at the surface.

For imaging of primaries a receiver-side wavefield contained separated up-going component, whereas source-side wavefield contained the actual source wavelet that was injected at the depth of the water bottom. Note, the image contains crosstalk as visible in Figure 5.6c and the water bottom is not imaged. The crosstalk is caused by linear mapping of surface multiples with a source wavelet (see also Fig-

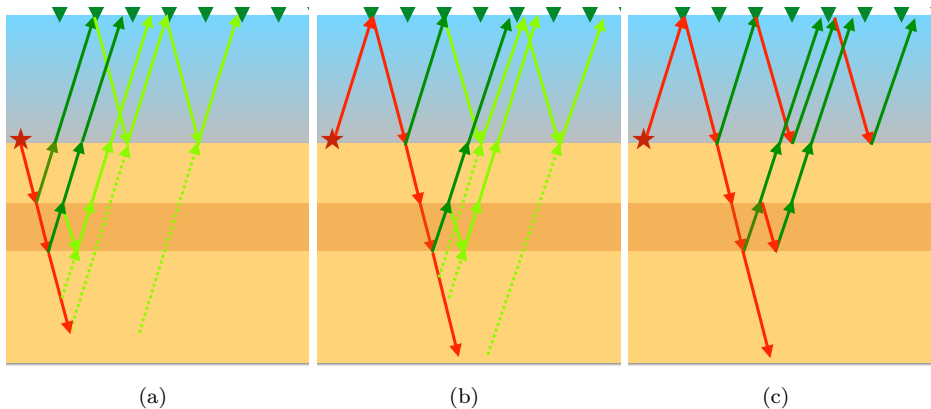


Figure 5.5: Imaging options considered in this paper. a) Imaging primaries; b) Mirror source imaging; c) FWM of surface multiples. Red paths represent source-side wavefield continuation. Green paths represent receiver-side wavefield back-propagation. Light green paths indicate events being not imaged correctly and a dashed line means a wrongly back-propagated event that creates crosstalk after being cross-correlated with a non-relevant event.

ure 5.5a).

The next imaging approach is based on the mirror-source principle. In this example we use the direct arrival as a source-side wavefield, whereas the receiver-side wavefield is the separated downgoing component of the measured data. This approach shows a significant improvement for imaging the water bottom, as can be observed in Figure 5.6d. Note, however, that the mirror-source image is not yet crosstalk free.

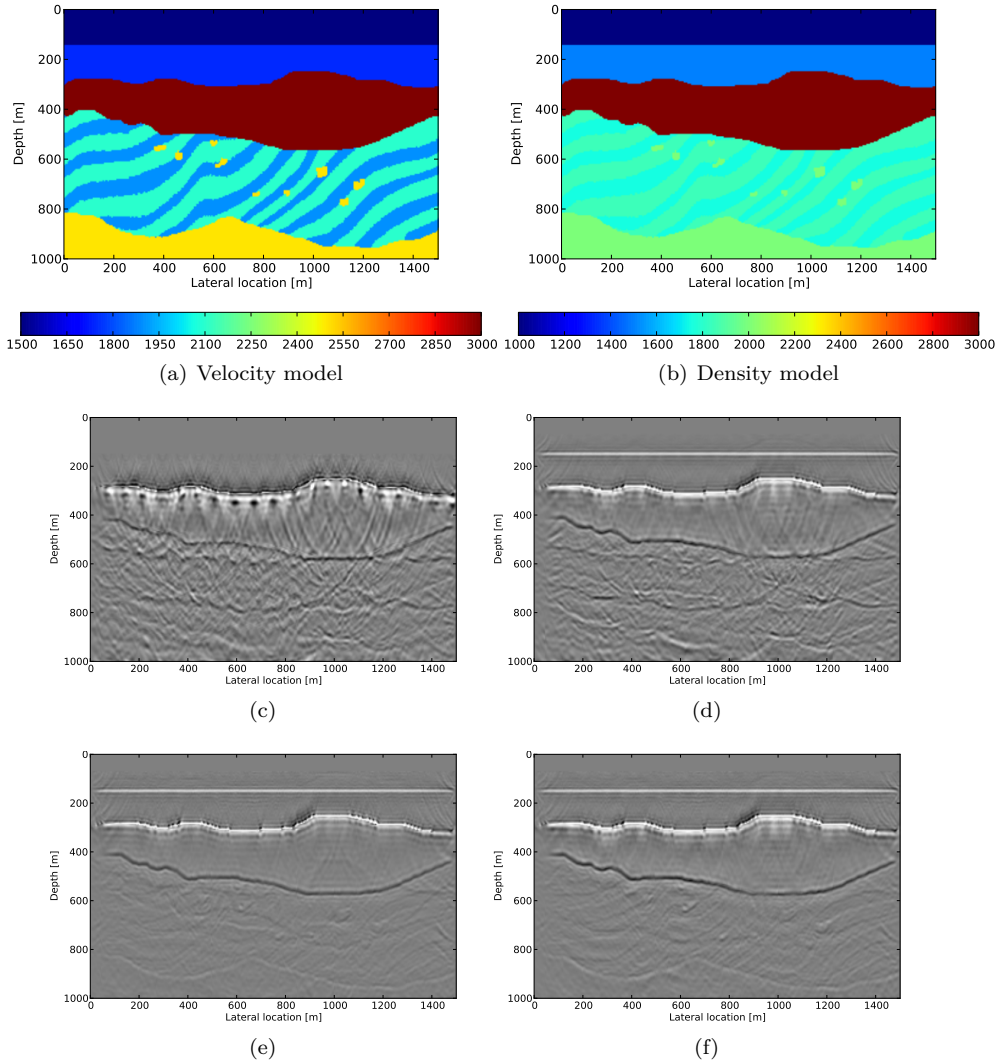


Figure 5.6: Numerical 2D example for imaging OBN data. a) Velocity model; b) Density model; c) Imaging of primaries; d) Mirror source imaging of first-order surface multiples; e) FWM imaging of all multiples.

As shown in Figure 5.6d again crosstalk is formed, but now by interference of the second-order surface multiple with the reflected direct arrival (being only one event representing the source-side wavefield, as also shown in Figure 5.5b).

Imaging of the surface multiples by PWM and FWM approaches are shown in Figures 5.6 e,f respectively. Note that there is no crosstalk with primaries, because they are not present in the downgoing component that is used for imaging. The receiver-side wavefield was muted before the arrival time of the earliest second order of surface multiple. Note that imaging results for FWM (Figure 5.6f), as expected, have resolved internal multiples and transmission effects, which provides more accurate result than one of PWM (Figure 5.6e).

5.5 Source estimation

It was already discussed that in order to obtain a true-amplitude image from primary reflections a correct source wavelet, especially in terms of its amplitude, is required. If the amplitude of the wavelet is overestimated it will lead to the underestimation of the reflection coefficients. As result, FWMod will model too weak internal multiples and, therefore, the crosstalk from internal multiples will not be sufficiently suppressed. On the another hand, underestimation of the source amplitude leads to the overestimation of the reflectivity. In that situation, instability in the forward modelling may arise: internal multiples can be modeled with amplitudes stronger than original primaries if the reflection coefficients get larger than 1.

In the previous sections we already demonstrated the benefits of imaging surface multiples. The source estimation procedure is also based on the surface multiple image as a starting point.

First, we start imaging using the re-injected total data at the source-side and the total data at the receiver side. The final image will show anti-causal crosstalk that will remain in the final image in order to explain primaries by re-injected data. In order to minimise this crosstalk, the image can be muted above the water bottom. Alternatively, this crosstalk can be avoided if purely separated multiples are imaged.

Next, it is possible to perform one roundtrip of FWMod in the adjoint mode for the measured total data: it will be visible that primaries will be focused at the position of the source, whereas surface multiples will be kinematically located at the position of the primaries. Selecting the resulting wavefield only around the source location and for small travel times, thus retrieving only the focused part, may be considered as a gradient for the source estimation.

Figure 5.7 shows the closed-loop (inversion) approach for this source wavelet estimation process. The total data serves as an input. If separated primaries are available, they will be even more desirable. Next, a roundtrip of the adjoint FWMod is applied, which provides the gradient for updating the source. Next, we perform

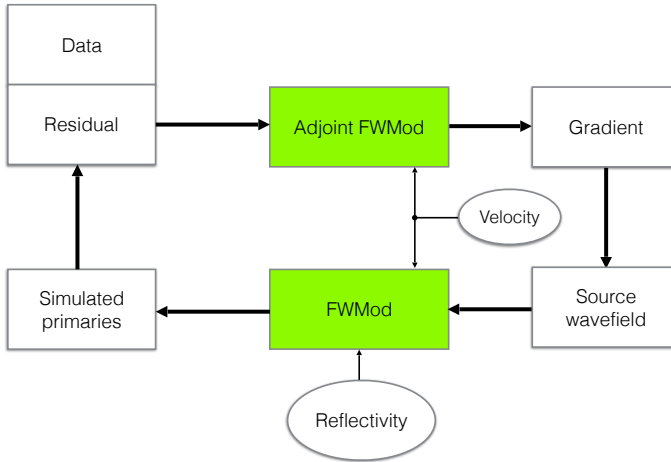


Figure 5.7: Source estimation scheme using iterative focusing of the data and modeling of the primaries. Reflectivity is considered to be given (by imaging from surface multiples) whereas the source wavelet is assumed to be unknown.

forward modelling using the updated source wavefield and the resulted modeled primaries are subtracted from the input data. Then, the new residual is computed and it can be used for computation the gradient for the source wavefield in the next iteration. It is noticeable that this closed-loop scheme is very similar to FWM, but instead of estimating reflectivity the source wavefield is estimated, while reflectivity is kept as is. Thus, the difference is only in the model space (source wavefield instead of image) and in the adjoint operator (source focusing instead of imaging).

A simple synthetic example demonstrates the source estimation procedure. There is one horizontal boundary represented by a homogeneous velocity and a density contrast shown in Figure 5.8. The data was generated by an acoustical finite-difference modelling scheme with a free-surface boundary condition.

The modeled shot record with a source located in the middle ($x=1500\text{m}$) of the model is shown in Figure 5.9a. First, six iterations of FWM were performed without knowledge of a source wavelet, meaning that the measured data, scaled with -1, was used as the source-side wavefield and, thereby, primaries are considered to be noise, ending up in the residual (see Figure 5.9b). Anti-causal crosstalk located in the image needs to be muted, otherwise primaries can be wrongly explained by reflected surface multiples. The corresponding estimated images are shown in Figures 5.10a,b.

Primaries for each shot record were re-datumed towards the source position in the described iterative manner. Figure 5.11a shows the true source wavefield and the estimated source wavefield (Figure 5.11b). When the source is estimated we can re-start FWM and migrate from scratch using both estimated source wavelet and re-injected data, thereby imaging the total wavefield. The final residual is shown in Figure 5.9c, while the estimated images are shown in Figures 5.10c,d.

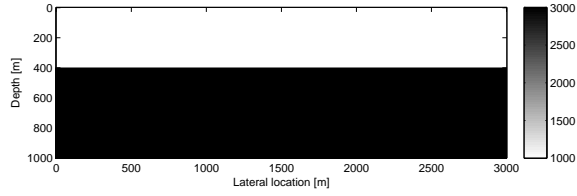


Figure 5.8: Subsurface model (density) for generating numerical data.

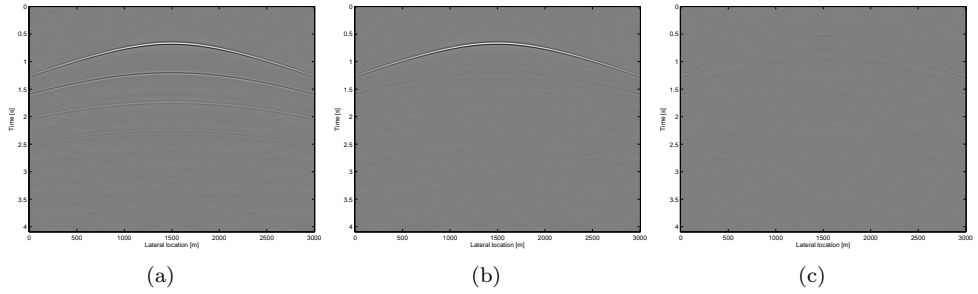


Figure 5.9: Residuals at different iterations: a) First iteration (data); b) Last iteration without the source knowledge; c) Last iteration after using the total data and including the estimated source wavefield.

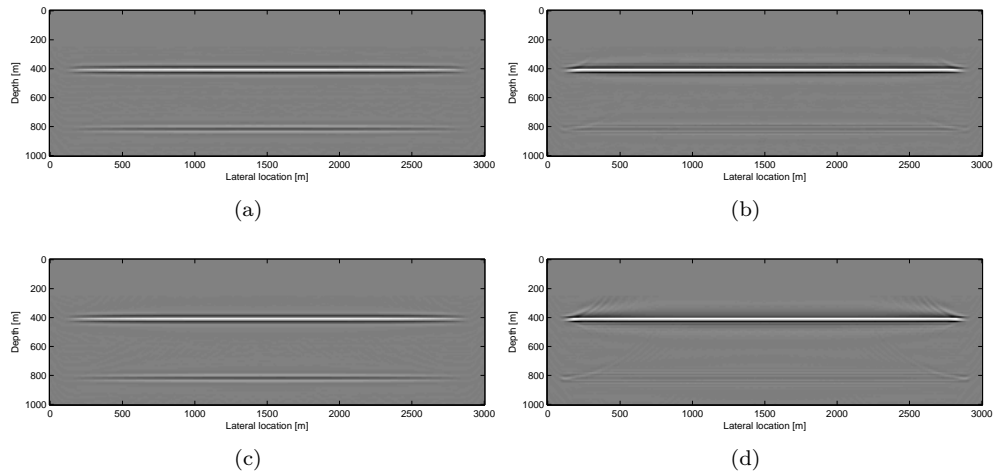


Figure 5.10: Images at different iterations: at the first iteration (a), at the last iteration without source wavefield (b), at the first iteration with the estimated source wavefield (c) and at the last iteration with the estimated source wavefield (d).

The focused wavelet is truncated along the time axis such that it excludes artifacts surface multiples that are translated to primaries. Hence, forward modelling is

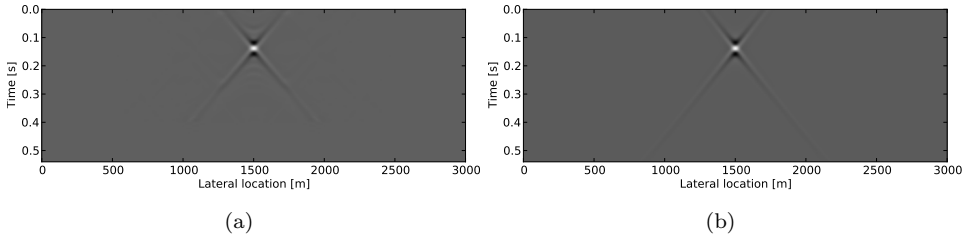


Figure 5.11: Estimated source wavefield (a) versus true source wavefield (b).

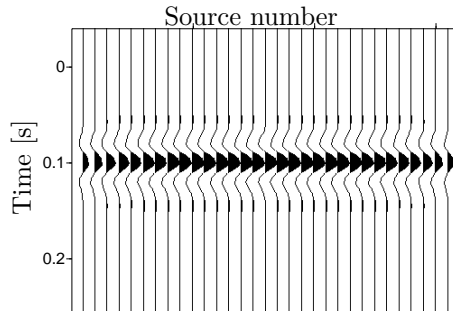


Figure 5.12: Estimated wavelets for different shot-records.

performed with a source side wavefield containing the estimated source wavelet only. It is also possible to truncate the wavelet spatially. For instance we can estimate only one trace of the wavelet per shot record. The results of such estimation is shown in Figure 5.12. It is important to mention that a spatially truncated wavelet loses its directivity information, whereas the fully sampled source wavefield (as shown in Figure 5.11) will have directivity effects included.

It appears that using a spatially truncated wavefield is good for missing data interpolation using FWMod. For example, the source can be estimated when near offsets are present and the result of the forward modeled data using the spatially truncated source wavelet can be used for near-offset reconstruction. In this way it becomes possible to estimate missing data using FWM and FWMod. Interpolation using FWMod is discussed in the next section.

5.6 Interpolation using Full Wavefield Modelling

In this section it will be shown that full wavefield modelling can also be used as an interpolation tool. The data can be modelled using the reflectivities obtained by FWM but in a denser sampling than the actual receivers. Next, the modelled data can be infilled in the missing traces, after which imaging can be repeated again.

Figure 5.13 shows how missing data interpolation can be introduced in the FWM closed-loop algorithm as an additional outer loop. It is proposed to perform several FWM computations with repeating a complete reset of the reflectivities and the wavefields. Before each 'reset' the upgoing wavefield can be infilled in the missing data, therefore, the new residual can be calculated from a combination of the original traces with the missing data filled in by traces obtained from FWMod.

A first interpolation example is based on the model introduced in Figure 3.4, but the input data has a smaller amount of traces as it represents marine streamer acquisition: we simulate a moving spread acquisition with a minimum offset of 100 meters and a maximum offset of 350 meters. The original shot record is shown in Figure 5.14b. Note that the negative offsets are sparsely sampled because of the source sampling that is being coarser than the receiver sampling (50 meters and 10 meters, respectively). Figure 5.14a demonstrates obtained FWM image after some iterations of using the incomplete data.

Next, the missing traces from Figure 5.14b are replaced by traces obtained by FWMod using the image from Figure 5.14a. The new complete shot record is shown in Figure 5.14c.

It is interesting to note that interpolation by FWM can be more efficient in the angle-independent mode. The reason is that by using a single parameter per grid-point 'spreads' the energy equally along the offset, while during the angle-dependent mode the data including missing areas will create distorted angle-dependent reflectivity behaviour, from which missing data cannot be properly estimated.

Of course, such data reconstruction approach will be especially useful for 3D situations, where the cross-line direction is usually coarsely sampled due to the typical marine streamers configuration. The next synthetic example demonstrates implementation of FWMod interpolation in 3D. There are 4 sources located at the center of the surface. The receiver spacing is 10m in the in-line and 50m in the cross-line direction. The original input data is shown in 5.15a. The image obtained using this data is shown in Figure 5.15c. After this, the missing data is reconstructed using the modelled upgoing wavefield, shown in Figure 5.15b. Note, that the final

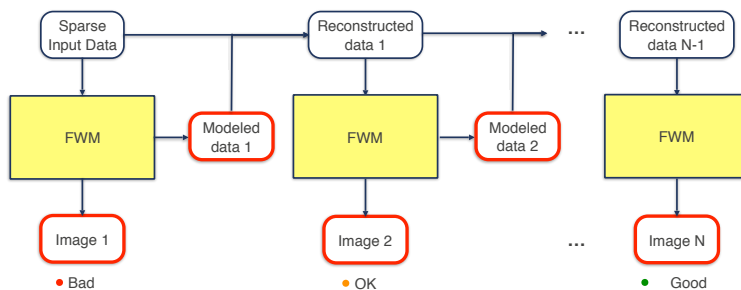


Figure 5.13: Interpolation strategy using modelled wavefields obtained by FWM(od).

image (Figure 5.15d) is improved with aliasing artifacts reduced, which were visible in the horizontal slice in Figure 5.15c as a striping pattern across the coarse sampling direction.

This set of examples demonstrates that FWM can be designed as a self-sufficient approach that handles the missing data. At each reset of FWM, the modelled traces from FWMod are re-inserted at the missing locations, which provides a better image for the following run of FWM.

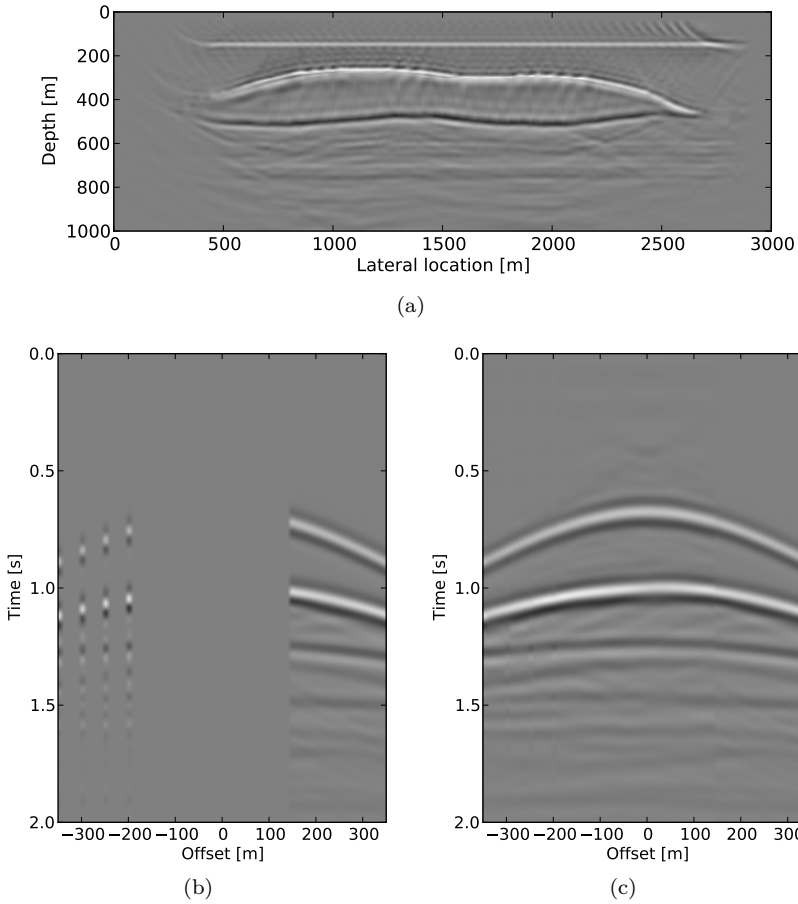


Figure 5.14: Reflectivity image (a) obtained by imaging the data shown in (b) and data reconstructed by Full Wavefield Modeling (c).

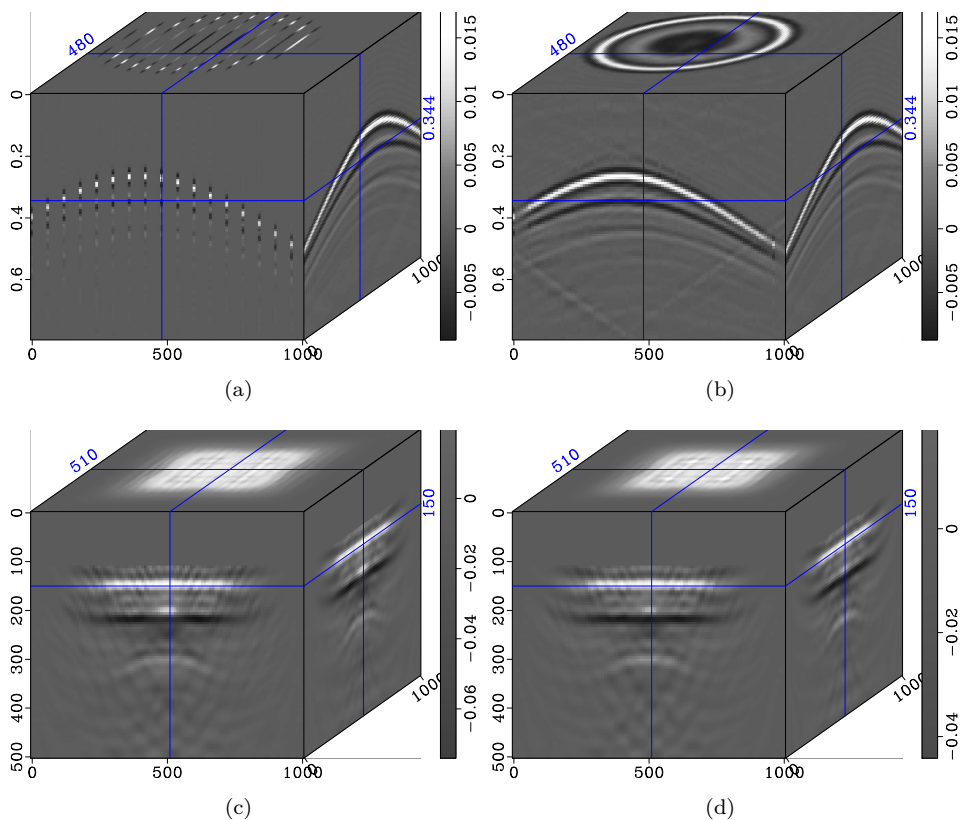


Figure 5.15: Original data (a) and data interpolated by FWM (b). Images using the original data (c) and interpolated data (d).

5.7 Separated primaries and multiples prediction

Once an FWM image is obtained, FWMMod allows to model specific events depending on the source-side input. Therefore, the forward model can be used as a primary/multiple separation process. This option was already briefly discussed in the joint imaging of primaries and surface multiples. However, the primaries and multiples from FWMMod can also be considered as the output of FWM process. As an example, Figure 5.16a shows the total surface data based on the model shown in Figure 3.4 a,b. After FWM a crosstalk free, true-amplitude image has been obtained. Using this image, the primaries can be modelled (predicted) by using the source wavelet at the source side (Figure 5.16b). Surface multiples can be predicted as well by using the re-injected measured, total wavefield, excluding the source wavelet, at the source side, for which the result is shown in Figure 5.16c.

Optionally, the predicted primary wavefield can be (adaptively) subtracted from

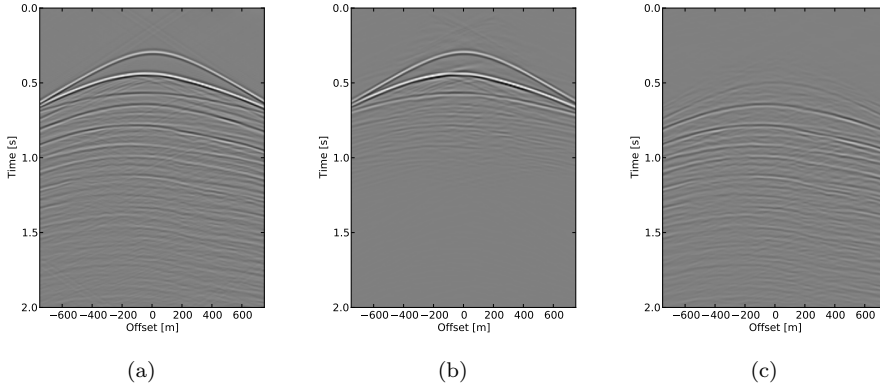


Figure 5.16: Example of predicting primaries and surface multiples: a) total input data, b) predicted primaries and c) predicted surface multiples

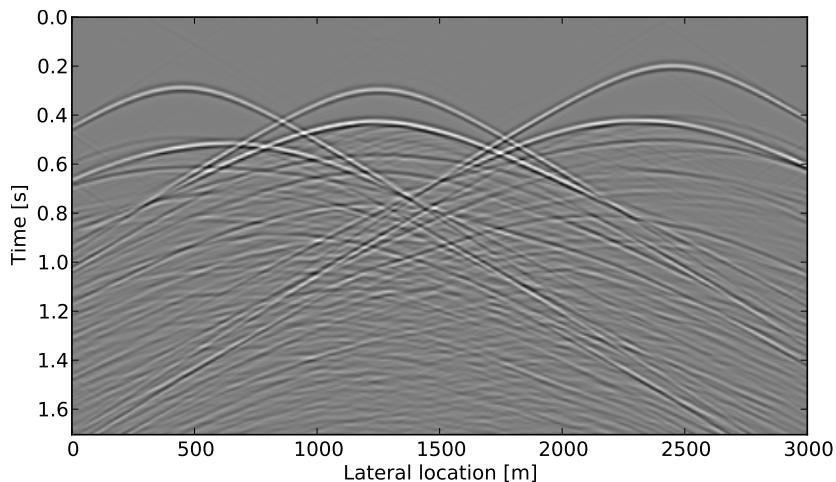
the original shot-record in order to calculate more accurate surface multiples, although potentially leaving some residual primary energy as noise. Vice versa, predicted surface multiples can be subtracted from the input data in order to get more accurate primaries.

5.8 Deblending

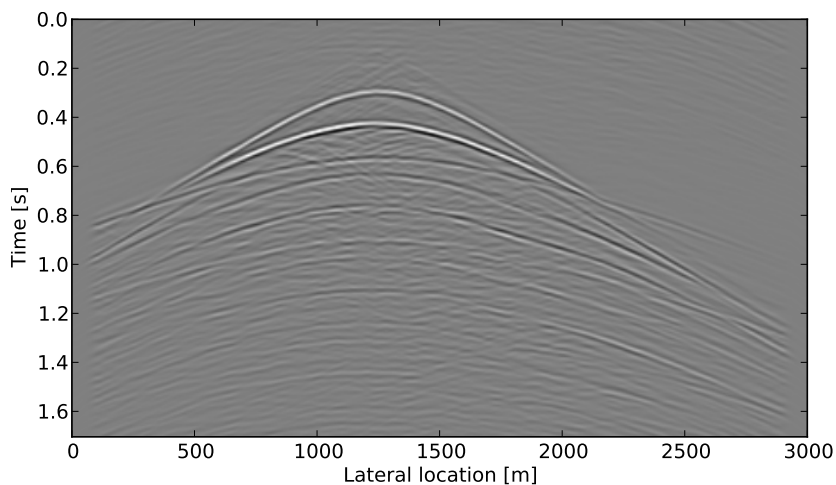
Another application of FWM can be used for de-blending purposes. The approach can be described as follows. Given the blended shot-records with known source encoding and source signature FWM imaging can be performed, which eventually will produce the image with suppressed blending noise. Next, the unblended shot record can be computed in two ways. In the first way a straightforward modelling can be applied where the source wavefield contains its wavelet at zero-time. Alternatively, deblended shot record can be achieved by modeling of the encoded source wavefield excluding the wavelet of the 'target' shot record. Next, the modeled blended shot records can be subtracted from the complete data in order to retrieve the shot record of interest.

Figure 5.17a shows one of the numerically blended shot records containing three simultaneous sources simulated on the model shown in Figure 3.4. After obtaining a crosstalk-free FWM image (as the closed-loop approach also deals with the simultaneous sources crosstalk), each separated shot record can be optionally predicted using FWMod, as shown in Figure 5.17b.

Alternatively, the de-blended shot record can be computed as a sequential subtraction of all predicted blended source responses except the source record of interest.



(a)



(b)

Figure 5.17: Example of predicting de-blended shot-record: given blended data (a) and predicted unblended shot (b) after modelling from the FWM image.

5.9 Discussion

In this chapter it was demonstrated that FWM can be used to perform data reconstruction (interpolation), simultaneous sources deblending and source wavelet estimation. It is interesting to compare FWM with other algorithms recently developed and closely related to FWM - being the Focal domain method (Kutscha and Verschuur, 2012; Kontakis and Verschuur, 2014) and Estimation of Primaries

by Sparse Inversion (EPSI) (Van Groenestijn, 2010). Both the focal domain method and EPSI aim at explaining the observed data via a specific data-driven parameterisation and are used for data preprocessing (deblending, prediction of primaries and source estimation). Table 5.2 compares the main features of the three methods.

The aim of the focal domain method is to estimate the focal domain wavefields $\mathbf{X}(z_n)$ obtained by focusing the surface data at the major reflectors of the subsurface. Besides the focused primary event each focal domain wavefield also contains other events in the anti-causal and causal parts. Actually, each focal domain wavefield can be considered as the response of virtual sources and receivers positioned at the depth level of interest. The forward model of focal domain method is described as follows:

$$\mathbf{P}^-(z_0) = \sum_n \mathbf{W}^-(z_0, z_n) \mathbf{X}(z_n) \mathbf{W}^+(z_n, z_0). \quad (5.1)$$

Equation 5.1 says that the reflection data can be presented as a sum of such focal domain wavefields with linearly applied \mathbf{W} operators on both sides. Typically, a sparseness constraint imposed on the focal domain suppresses acquisition footprint effects. Therefore, after applying the forward model, the reconstructed data can be obtained. Because there are usually few depth levels, some of the events can be represented by different focal operators simultaneously. Such freedom in the parameters space allows to fit the observed data very well. Using just a macro velocity model is sufficient, which is convenient because usually at the pre-processing stage accurate velocity model is not yet present.

FWM can be approximately considered as an extreme case of the previous method in the sense that the reflectivity is also a focused wavefield but containing only the reflection event and not other events. To achieve this, FWM requires an accurate velocity model and imaging at every depth-level. Upside and downside reflectivities being respectively multiplied with a downgoing wavefield and upgoing wavefield gives a two-way scattering term that can be linearly propagated to the surface. The sum of such operators gives the modeled data. The main difference with the focal domain is that the modelling of the downgoing and upgoing wavefields is non-linear (see scheme in Table 5.2). Moreover, it mainly aims first at estimating the reflectivity (construct an image), although in this chapter it was shown that it can also be used for providing the data (and not only at the surface depth level). In such mode FWM can be considered as a data transformation, just like the focal domain method.

FWM in this case is more expensive than the focal domain, but it can be more accurate because it comprises the scattering terms at every depth level with a step size of imaging. The reflectivities contain only information at zero-time (imaging condition) and does not contain the anti-causal and causal parts that are present in the focal domain and which should be kept in order to explain the surface data. Because the zero-time is selected in FWM, no sparsity (in time domain) constraint is required. The upgoing and downgoing wavefields contain only causal components. However, as mentioned before, FWM relies on having accurate velocity model.

Table 5.2: Comparison of FWM with the focal domain method and EPSI.

Method	Focal	FWM	EPSI
Forward model	$\sum_n \mathbf{W}^- \mathbf{X}(z_n) \mathbf{W}^+$	$\sum_n \mathbf{W}^- \delta \mathbf{S}(z_n)$	$\sum_n \mathbf{X}_0 \mathbf{S}$
Model space	\mathbf{X}	\mathbf{R}	\mathbf{X}_0
Depth levels (n)	Few	Many	Only one
Velocity information	Approximate	Accurate	None

Another development – EPSI – aims at explaining the primary impulse response data \mathbf{X}_0 from the measured data including all surface multiples. Actually, the estimated response should contain only primaries and its interbed multiples. The forward model can be described as follows:

$$\mathbf{P}_{obs}^-(z_0) = \mathbf{X}_0(z_0)[\mathbf{S}^+(z_0) + \mathbf{R}^\cap(z_0)\mathbf{P}_{obs}^-(z_0)], \quad (5.2)$$

where the first term on the right hand side ($\mathbf{X}_0\mathbf{S}$) explains the observed primaries (and their internal multiples) and the second term ($\mathbf{X}_0\mathbf{R}^\cap\mathbf{P}^-$) explains the observed surface multiples (and their internal multiples). Via inversion, \mathbf{X}_0 and \mathbf{S}^+ are estimated by explaining the observed data.

It is also important to mention that hybrid approaches can be implemented. For example, the so-called focal closed loop SRME method (Lopez and Verschuur, 2015) implies the forward model that is based on the coupling of the forward modal of the Focal domain method (Equation 5.1) with the forward model of EPSI (Equation 5.2).

5.10 Conclusions

In this chapter it was demonstrated that FWM can have various applications and strategies in imaging. It was shown that imaging of surface multiples can be very beneficial for revealing structures located close to the source: shallow reflectors, such as the water bottom, or even the area close to a deep water bottom in case of ocean bottom node (OBN) data imaging. Imaging of surface multiples can also be very useful for the full 3D case as usually sources and receivers are relatively sparse in at least one dimension.

It was also shown that it is possible to estimate the source wavelet using imaging of surface multiples. A closed-loop procedure was introduced for estimation of the effective source wavefield.

In the rest of this chapter it was also demonstrated that it can be important to consider not only the resulting image as an output of FWM but also the modelled wavefields that are accessible at every grid-point on the subsurface. FWM can be considered as a transformation that decomposes the surface data in terms of the subsurface wavefields related to the subsurface reflectivities at the corresponding grid-points. Successful application of this approach are primaries/multiples separation, deblending and data reconstruction.

6

Field data examples

6.1 Introduction

This chapter will demonstrate the application of FWM to several field datasets. All datasets are offshore but have different depths of the water bottom. First, the chapter is focused on the role of the surface multiples in imaging in shallow and deep water scenarios. An example of imaging of multiples in 3D sparsely sampled OBN data is demonstrated as well. Next, suppression of crosstalk from internal multiples is demonstrated. Additionally, the source wavelet estimation and data prediction process, as discussed in the previous chapter, are demonstrated.

6.2 Imaging of surface multiples

In this section applications of imaging of surface multiples by FWM to field data is studied. Firstly, a 2D deep water case scenario is discussed. Next, the application to 2D data acquired in shallow water is shown. Finally, the features of using surface multiples are demonstrated for 3D OBN data, where primaries cannot provide a decent image at all.

6.2.1 Deep water scenario

As a first example a dataset from the Gulf of Mexico (kindly provided by PGS) is used. The available data consists of a dual-streamer sail line with only positive offsets, the minimum offset being 125m. Regarding the pre-processing, a deconvolution has been applied to separate downgoing and upgoing wavefields using P-Z summation. The source wavelet was not known and only positive offsets (actual measurements) were used.

First, imaging without source wavelet has been performed using only the re-injected surface total data as a source-side wavefield, such that only surface multiples contribute to the image. Figure 6.1a shows the imaging results at the first iteration. The red arrow indicates crosstalk formed due to the first order of scattering surface multiple at the source side interfering with the second order of surface multiple at the receiver side. Note that after 6 iterations (Figure 6.1b) this crosstalk has been

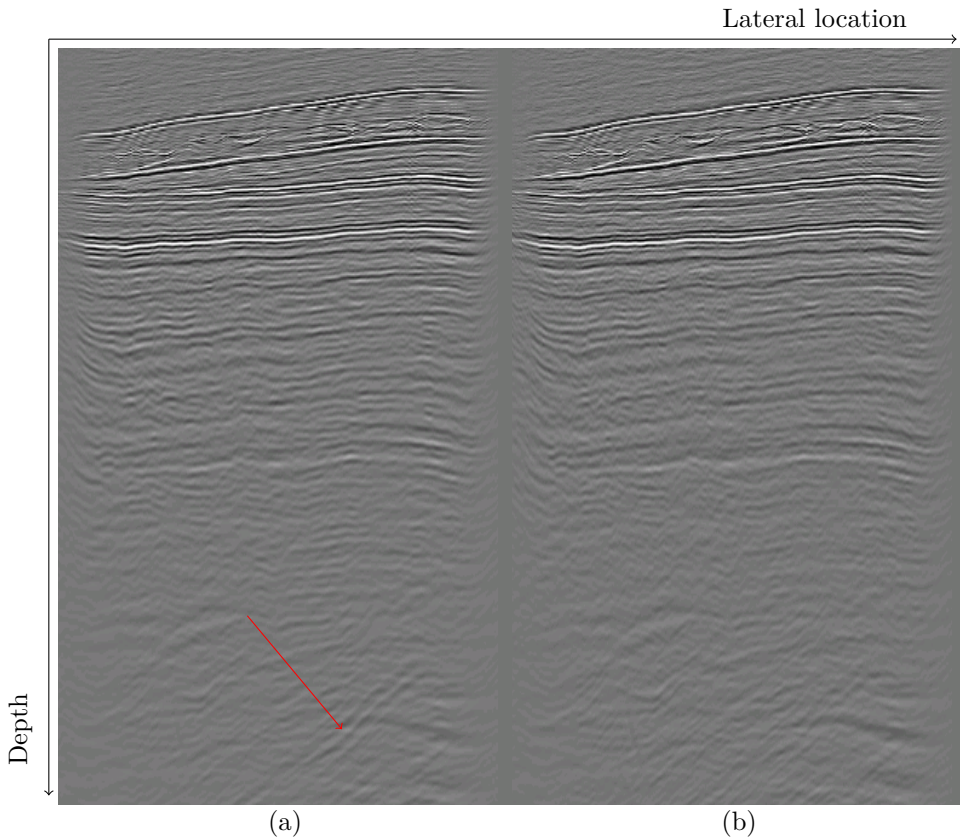


Figure 6.1: Field data FWM results on Gulf of Mexico data. a) First iteration of imaging only surface multiples; b) 6th iteration of imaging only surface multiples.

greatly suppressed.

Next, using the given image, the source wavelet has been estimated, as described in the previous chapter, and a new imaging process of the total wavefield has been performed. This means that the total data is used at the receiver side, while at the source side the measured data is re-injected together with the source wavelet ($\bar{Q}^+ = \bar{S}^+ + \mathbf{R}^\cap \bar{P}^-$). The result of imaging the total data is shown in Figure 6.2. The image at the first iteration is displayed in Figure 6.2a. Kinematically the same crosstalk is observed. Because the incident source wavefield is also present, crosstalk is generated due to the cross correlation of that wavefield with the first order of surface multiples. The image at the 15th iteration (Figure 6.2b) shows successful crosstalk suppression. Also note an increased resolution in the deeper part.

Comparing the image of the total wavefield (Figure 6.2b) versus imaging by surface multiples only (Figure 6.1b) we can observe that including the primaries in in

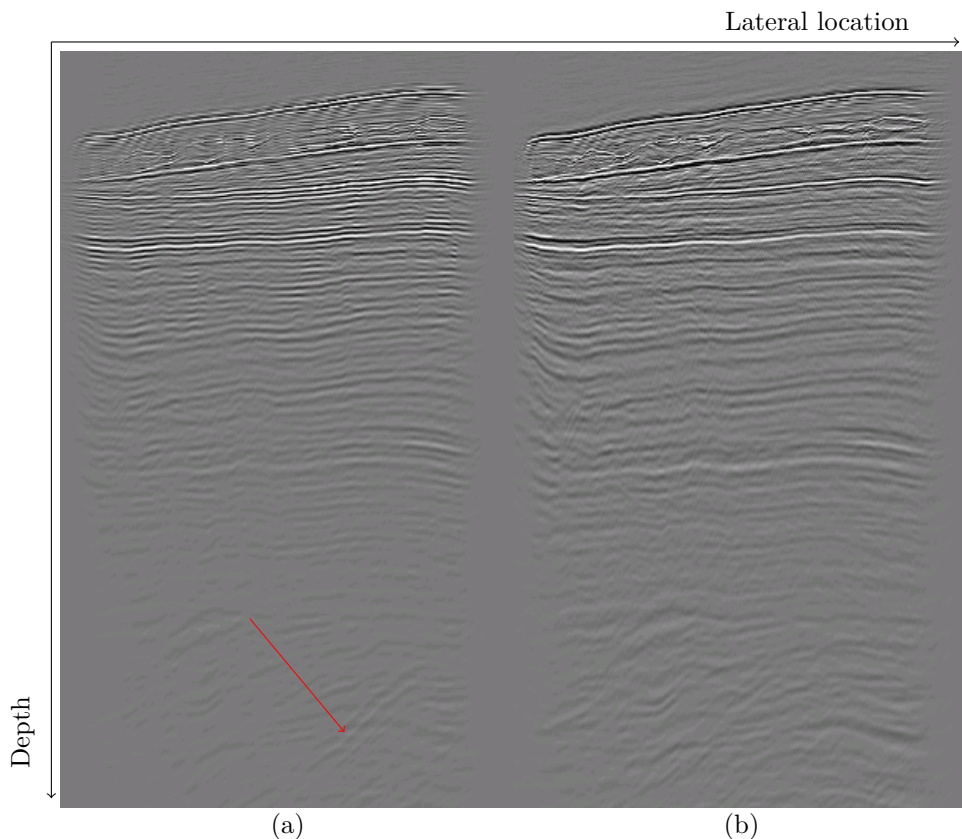


Figure 6.2: Continuation of Figure 6.1. a) First iteration of imaging the full wavefield; b) 15th iteration of imaging the full wavefield.

imaging still has advantages: they are strong, thereby, will have a better S/N ratio. Moreover, at deeper locations angle coverage by surface multiples will not be distinguishable anymore from angle-coverage of primary illumination. The better S/N ratio of primary imaging is clearly visible around the water bottom (the water layer is less noisy). Thus, for deep water the added value of using surface multiples in imaging may not be too large, as primary illumination for this data is already quite good. However, for 3D data in the cross-line direction there will be more benefits. Still, for this 2D line, an important contribution of using surface multiples was getting an accurate source field.

In the next section, however, it will be demonstrated how surface multiples do have advantages over primaries in the actual image.

6.2.2 Shallow water scenario

Next, using FWM in a shallow water situation has been investigated. The dataset, provided by PGS, has been acquired in the Nelson field located in the British sector of the North Sea. Figure 6.3 shows the nearest-offset gather of the available survey.

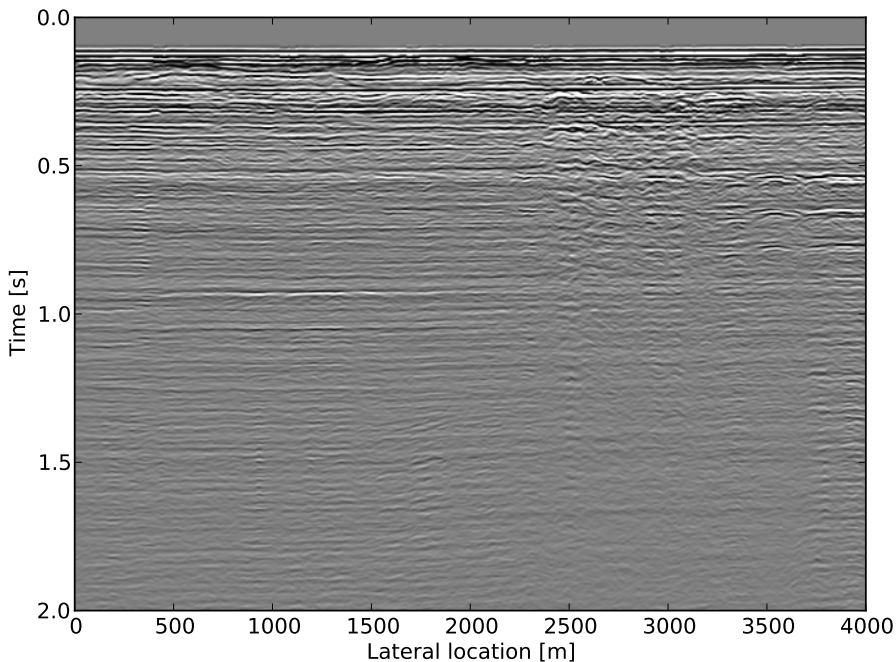
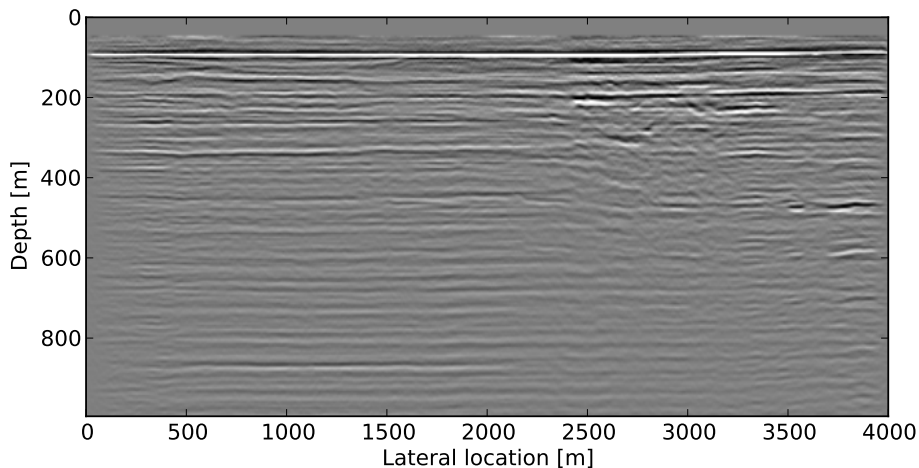


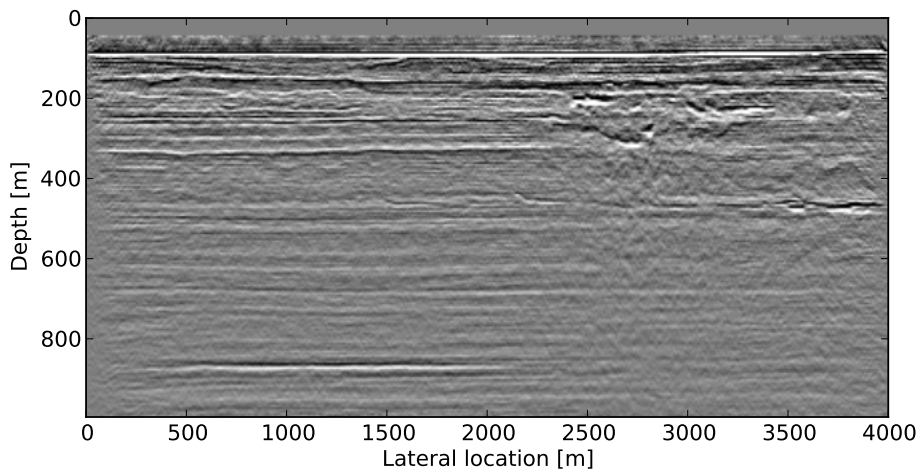
Figure 6.3: Nelson data nearest-offset sub-section. Note that reflections from channels and their multiples are well visible in the section around 2000-3500m in the lateral direction and between 0.15-0.5s in time.

The relatively shallow water bottom causes strong reverberation between the water bottom and the surface. Other strong surface multiples are also present due to the reflections from the so-called paleo channels that are more clearly present in the right part of the image.

The marine streamer data used as input for FWM has the following parameters: receiver sampling 12.5m, time sampling 0.004s, source sampling 25 m, record time (used) 2s. The basic preprocessing included near-offset interpolation. Surface multiples estimation has been done using the Estimating Primaries by Sparse Inversion



(a)



(b)

Figure 6.4: Full Wavefield Migration, imaging of surface multiples in shallow water. a) Image at the first iteration; b) Image at the 10th iteration.

(EPSI) method (Van Groenestijn, 2010).

Figure 6.4 shows the imaging of separated surface multiples. The image at the first iteration is shown in Figure 6.4a. It is visible that there is a lot of crosstalk visible as repetitive structures. The 10th iteration of FWM suppresses such crosstalk, as expected (shown in Figure 6.4b). Also note the improved resolution of the image due to the closed-loop approach of FWM. Next, imaging of primaries is performed, for which results are shown in Figure 6.5. Note, that the primaries were computed as a

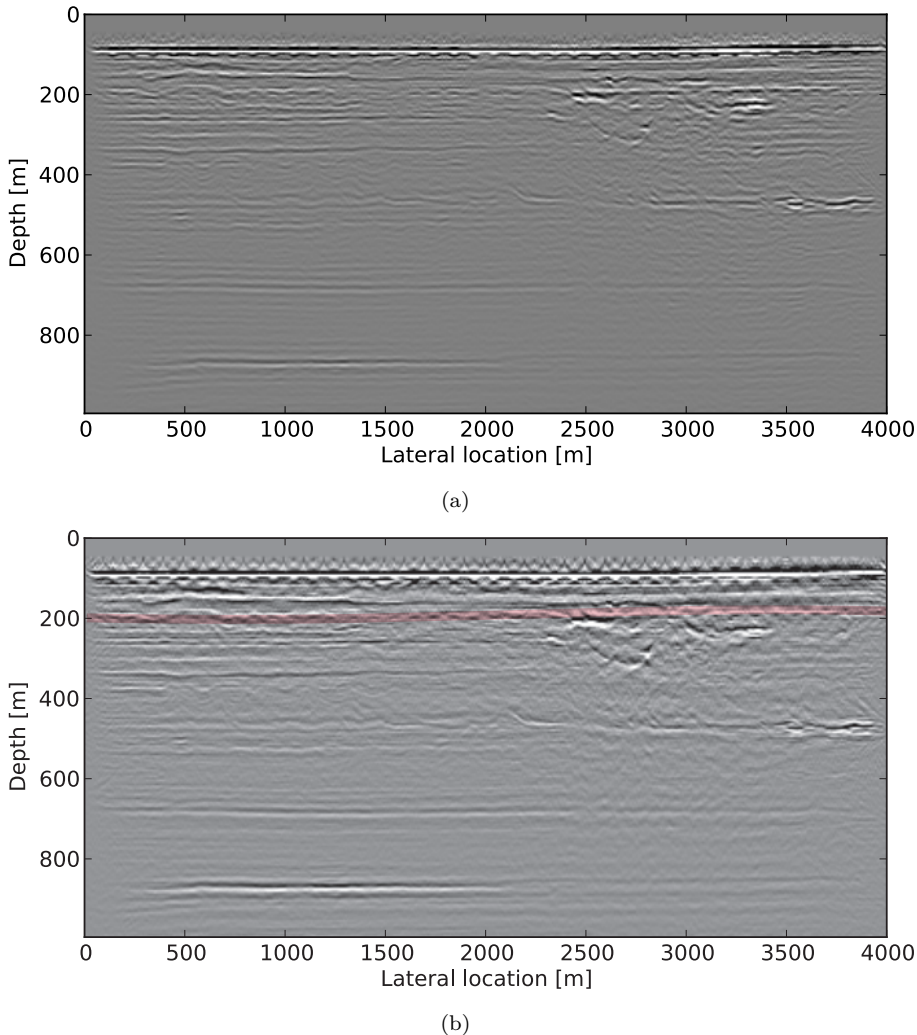


Figure 6.5: Full Wavefield Migration, imaging of primaries in shallow water. a) Image at the first iteration; b) Image at the 10th iteration.

result of adaptive subtraction of the surface multiples (as used in the previous set of examples) from the total data. The first iteration image (Figure 6.5a) seems to be already crosstalk free, because internal multiple crosstalk is not observable in this data. Note, however, that some residual multiple energy (from EPSI) is visible in the image (indicated by red line in Figure 6.5b), whereas imaging of surface multiples did not show such crosstalk. Also note the strong acquisition imprint on the water bottom and other shallow reflectors (Figure 6.5a and b).

Hence, this data example demonstrates that imaging of surface multiples has advantages as there is almost no acquisition imprint at small depths. It is shown that the crosstalk might be better suppressed by the closed-loop approach rather than eliminating it as a separated pre-processing step. However, the advantage of using surface multiples is decreasing with depth: at larger depths (starting from around 600 meters in this example) it is visible, that the primary image become more consistent than the image obtained by surface multiples.

6.2.3 3D ocean bottom node data

Even if primaries take the advantage over surface multiples at larger depths, there are situations, when there is hardly any illumination at all coming from the primaries.

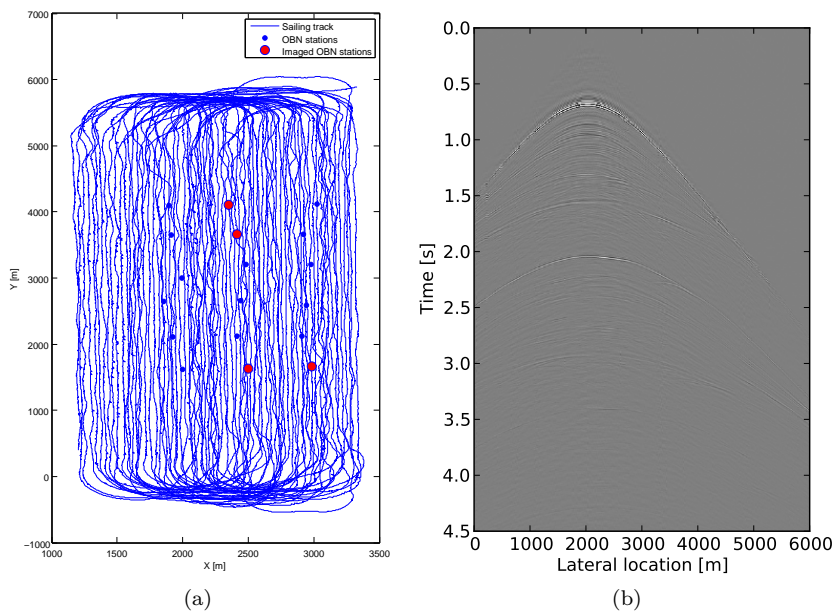


Figure 6.6: a) Geometry of the OBN nodes and sources. b) Common receiver gather along the y-coordinate for a fixed x-coordinate for one of the OBN stations. Note that primaries and surface multiples are well separated in time.

In this section we study the imaging of ocean bottom node (OBN) data in the reciprocal domain, where coarse 'source' (i.e. OBN stations) sampling fails to image the area close to the water bottom (where the stations are located). Therefore, as discussed in the previous chapter, imaging of the area around the water bottom is only possible via the surface multiples.

The data used in this section is kindly provided by TEEC. The data originates from offshore New Zealand (Bialas et al., 2013) and was acquired by GEOMAR. Figure 6.6a shows the geometry of the sources and receivers.

Figure 6.6b shows one common receiver record for a fixed x-coordinate. The missing traces have been linearly interpolated and extrapolated in the move-out corrected domain. The water bottom is so deep that surface multiples don't overlap with primaries in the data domain. Therefore, we used time muting in order to split the primaries and surface-related multiples.

Due to memory limitation, only four OBN stations were selected and, therefore, considered as shot-records (see the red dots in Figure 6.6). Figures 6.7a,b show the result of imaging of OBN data by using primaries only. Note the poor illumination due to the small number of shots (OBN nodes in the reciprocal domain) selected for imaging. Next, surface multiples are used for the imaging, the result being shown in Figures 6.7c,d and 6.7e,f. Figure 6.7c and Figure 6.7e show the images at the first iterations. The same pair of images at the 10th iteration are shown in Figure 6.7d and Figure 6.7f. Note that the difference between Figure 6.7c,d and Figure 6.7e,f is in the depth slice that is plotted on top of the image cube.

This example clearly demonstrates the extended illumination by surface multiples comparing to imaging by primaries. It is clearly visible, that the water bottom is nicely imaged. Also, due to the inversion process embedded in FWM, the resolution is increased and the lateral extend of the image has also improved. At the deeper horizontal slice in Figure 6.7f, some fault structures are now visible. Note that imaging of primaries, as discussed before, might perform better for the deep structures. However, imaging of the part that is relatively close to the water bottom by primaries is simply impossible in an OBN acquisition configuration.

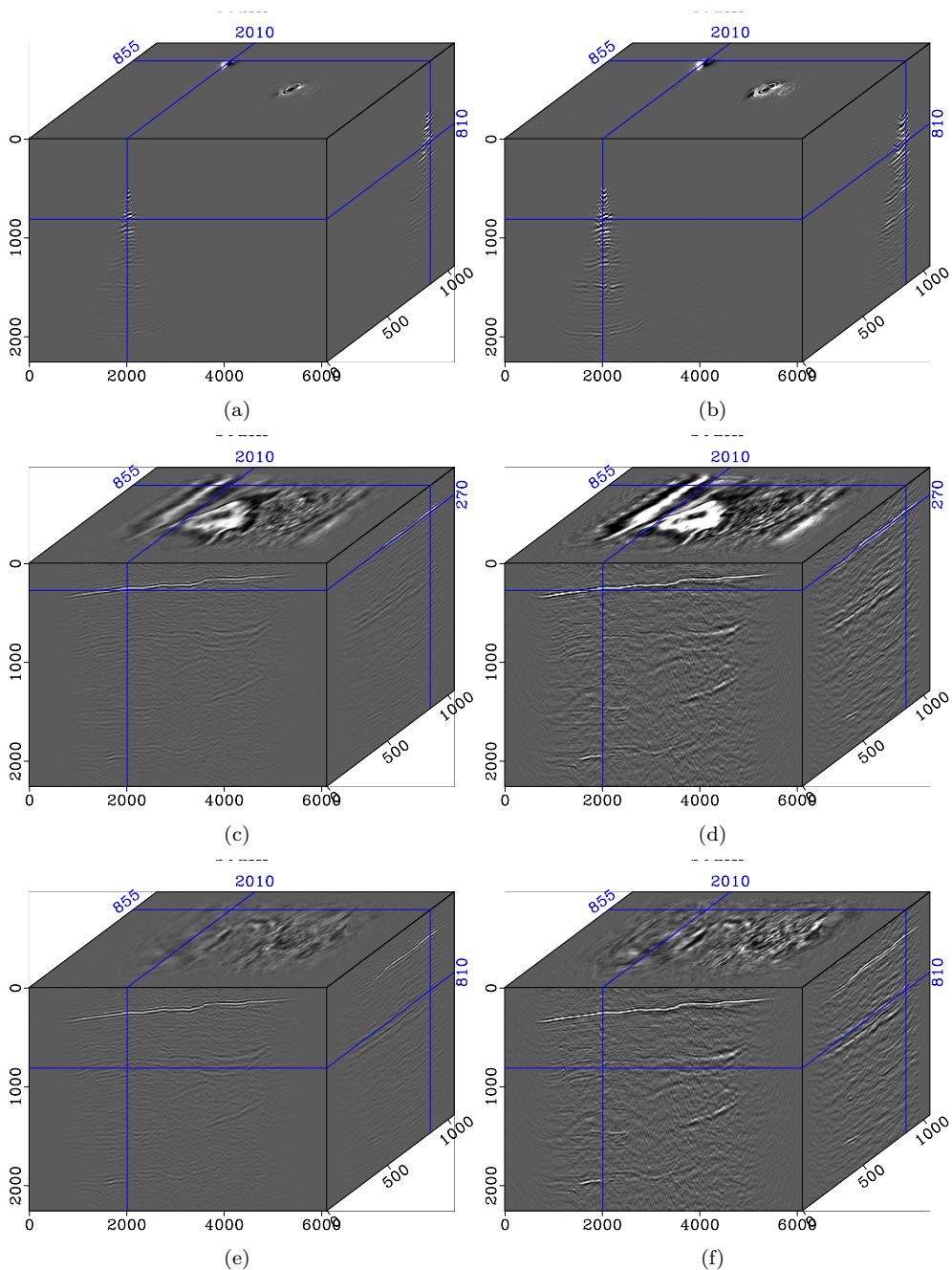


Figure 6.7: Full Wavefield Migration of OBN data using primaries only: image at the first iteration (a) and image at the 10th iteration (b); Full Wavefield Migration of OBN data using surface multiples only. Image at the first iteration (c) and image at the 10th iteration (d) when horizontal slice is selected at the water bottom and (e) and (f) are the same as (c) and (d) but for the horizontal slice selected at 800m depth.

6.3 Impact of internal multiples

This section demonstrates how FWM can deal with internal multiples in field data. The survey - provided by Statoil - originates from the Norwegian Sea and is located in the Vøring basin.

Because of the deep water bottom (1.5km), surface multiples are quite well separated from most of the primary reflections. It was known from previous studies that internal multiples are visibly present in the area between 2.5 and 3.0s (Berkhout and Verschuur, 2005).

The following pre-processing steps were done to the dataset:

- Interpolation of near offsets;
- Deconvolution for removing the air gun bubble effect;
- Surface-related multiple elimination;
- Estimation of the source wavelet using EPSI;
- Applying reciprocity and create a split-spread dataset.

In this example only the primaries will be imaged, meaning that surface multiples are separated upfront. The area of internal multiples crosstalk is located at smaller

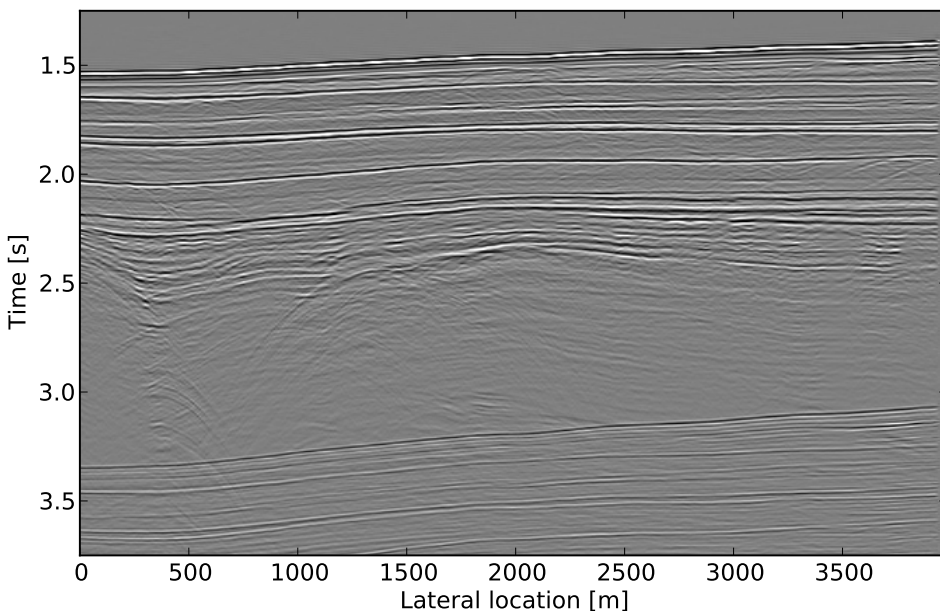


Figure 6.8: Near-offset cross-section from the Vøring basin dataset.

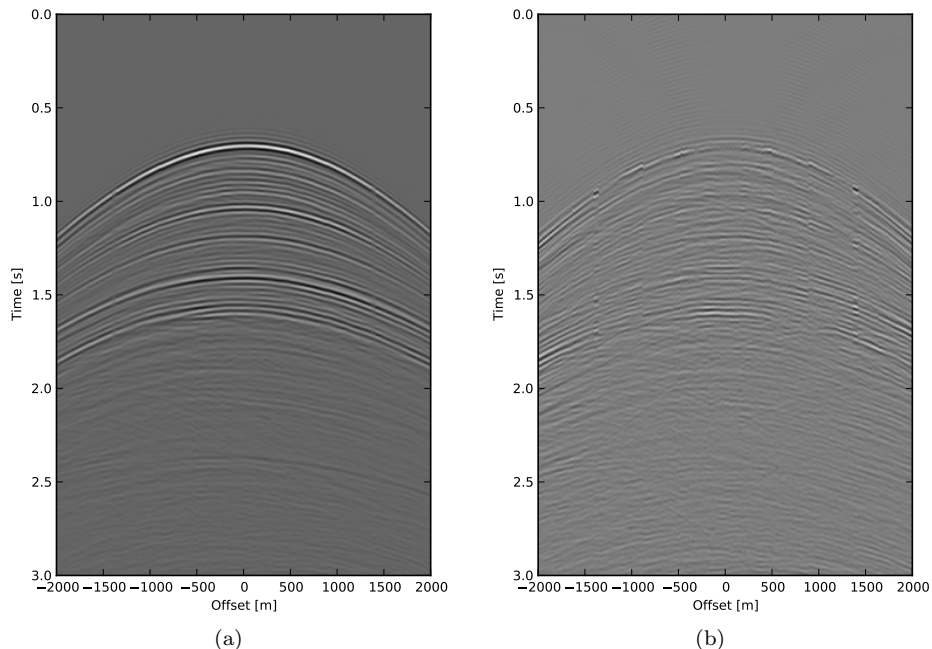


Figure 6.9: Field data from Vøring basin. a) Measured shot-record. b) Residual from the FWM process.

times than the possible crosstalk obtained by interference with residuals from surface multiples, which guarantees that internal multiples are not misinterpreted.

Figure 6.9 shows one of the measured shot-records after SRME (Figure 6.9a) and the residual (Figure 6.9b) obtained after the FWM procedure. Figure 6.10 shows the PWM image where internal multiples are not taken into account. Below the anticline structure it is possible to observe two groups of dipping events. The group of events that tends to be more horizontal is a result of crosstalk between the source wavefield and the internal multiples (shown by yellow arrows in Figure 6.10a).

The forward model of FWM includes internal multiples and, therefore, they are removed from the residual. As a result, the FWM image (Figure 6.10b) has the internal multiples crosstalk suppressed. Particularly, it is visible that in the FWM result the dipping structures at ($x=2000\text{m}$, $z=2250\text{m}$) are more clear.

The difference plot (Figure 6.10c) contains the crosstalk from the internal multiples that are suppressed in the FWM image. Note that the difference plot contains not only crosstalk but also actual reflector imprints because of the transmission effects that is taken into account in the forward model of FWM.

As a final remark, it can be seen from the residual data after FWM (Figure 6.9) that apparently some artifacts are present in the input data, showing up as lateral

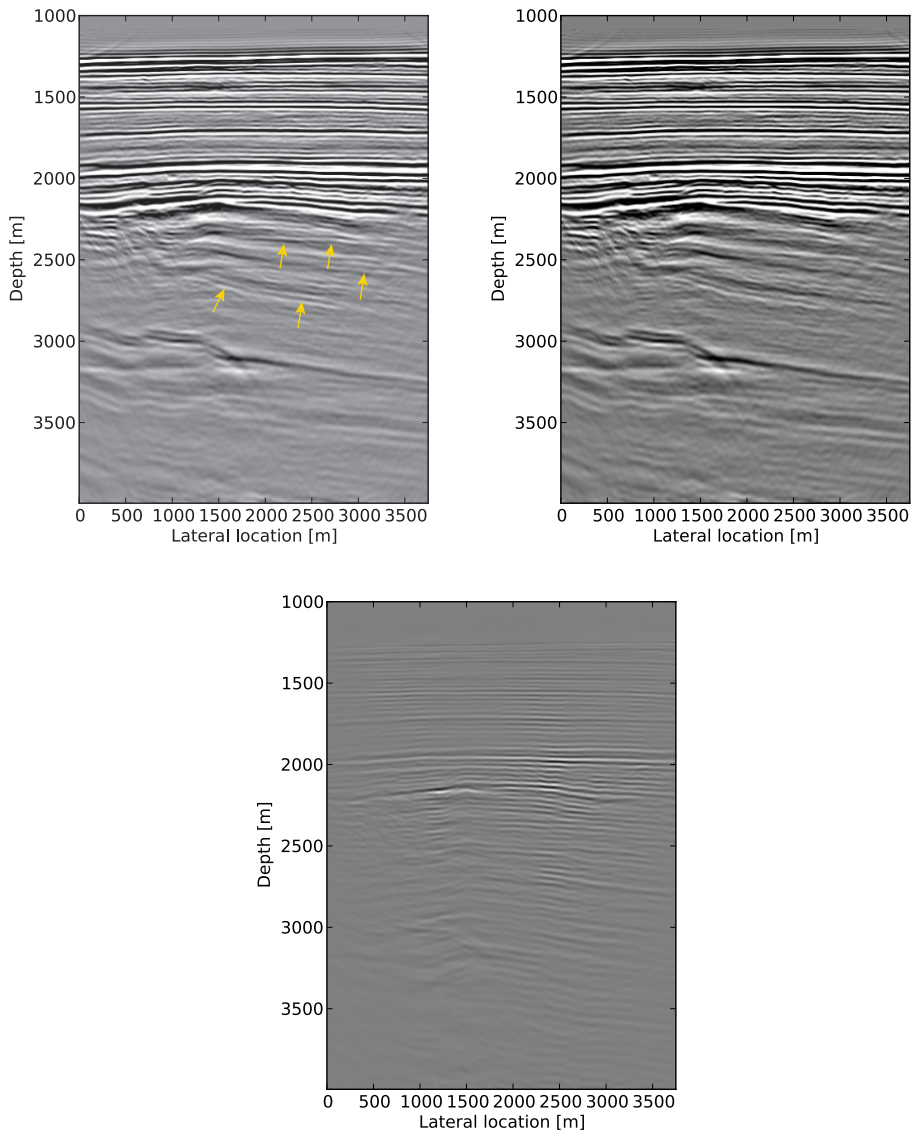


Figure 6.10: (a) Conventional least-squares migration image or PWM image; b) FWM image (note the suppressed crosstalk from internal multiples that was indicated with yellow arrows in a that was indicated with yellow arrows in a)); (c) Difference between (b) and (a).

inconsistencies in amplitude and phase in the residual. Ideally, FWM should fully reject them, as they are not physically consistent. These lateral inconsistencies are most probably acquisition-related and can be considered as noise in the input data.

6.4 Pre-processing and events prediction

The following set of examples demonstrates the interpolation and data prediction that can be obtained using FWMod, as discussed in the previous chapter. Examples will be based on the Vøring dataset, which was already used in the previous section.

The first example shows the potential of FWM to reconstruct missing traces. The fully sampled data has 25m trace sampling. For this experiment we keep only 1 out of 5 traces. The original data with missing traces is shown in Figure 6.11a. As discussed in the previous chapter, FWMod can be applied to the current FWM image obtained by incomplete data. After FWM imaging has been applied, next the FWMod modelled traces were infilled in the missing traces of the original dataset,

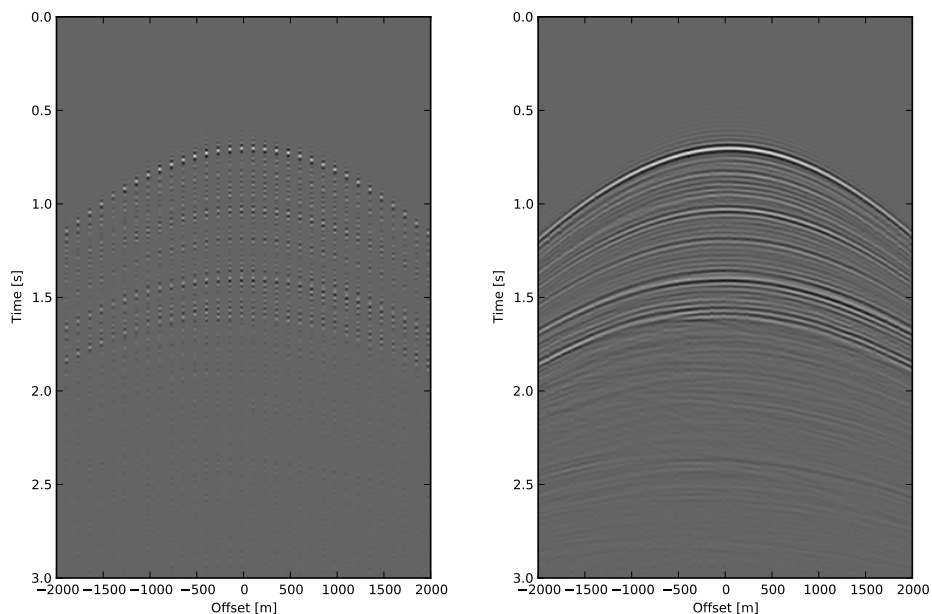


Figure 6.11: Data reconstruction example where 1:5 trace decimation was applied. Shot record before (a) and after (b) interpolation via FWM.

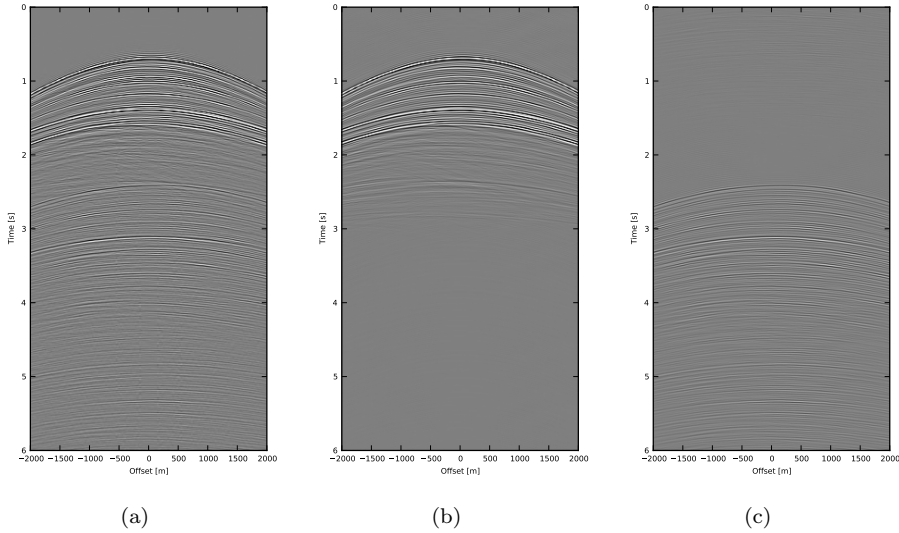


Figure 6.12: Event prediction example: (a) Total data, (b) modelled primaries and (c) modelled surface multiples.

thus creating a consistent result (Figure 6.11b).

Next, a brief example is shown for the primary/multiple separation on this field data (Figure 6.9). Figure 6.12a shows the original, total data. Figure 6.12b shows the modelled primaries using the estimated reflectivity from FWM and the given velocity model. Figure 6.12c shows the modelled surface multiples that were computed simply by using the re-injected total data instead of using the wavelet as a source-side wavefield. Note that the predicted wavefields can be (adaptively) subtracted from the total data in order to obtain more accurate primaries and surface multiples.

6.5 Discussion

Before concluding this chapter, some observations from the with field data examples will be discussed.

The examples in Section 6.2 show an expected behaviour of surface multiples. It was shown that multiples allow to get an image with extended illumination compared to primaries in case of imperfect acquisition design. However, it is also observable that the primaries provide better S/N ratio, due to their stronger amplitudes, and for deeper parts of the subsurface their illumination is as good as surface multiples, or even better.

Another issue that was encountered in the 2D examples is the geometrical spread-

ing that is not properly modeled in the 2D version of FWM when applied to field data. Ignoring this effect in the forward modelling leads to amplitude errors in the estimated reflectivity. As the amplitude decays with distance from the source, the deeper the reflector the more underestimated its amplitude will be. This situation becomes more complex in case of imaging of surface multiples combined with imaging of primaries (total wavefield imaging). In this case the estimated reflectivity will be a compromise between two unbalanced wavefields, which will lead to a relatively large residual and bad convergence of the algorithm. An approach to overcome this issue is proposed in Appendix B. Of course, full 3D FWM applied to 3D data will not have this problems.

6.6 Conclusions

In this chapter the FWM algorithm and its applications has been applied to field data. First, for imaging surface multiples it was shown that their contribution mostly lie in the area around the water bottom. Next, the application on sparse 3D OBN data showed the great advantage of using surface multiples. The effect of correct handling of internal multiples has been demonstrated on a dataset with a deep water scenario.

In the shallow water cases it was found out that geometrical spreading can affect proper estimation of the reflectivities when applying 2D FWM to field data. Therefore, either the data has to be corrected (3D to 2D conversion) or a more accurate way would be to modify 2D propagation operator such that amplitude attenuation due to the 3D geometrical spreading will be corrected (see Appendix B).

In addition, applications of FWM like source wavefield estimation (based on imaging of surface multiples) and data prediction has been sufficiently demonstrated on field data as well.

7

Conclusions and Recommendations

This thesis describes the methodology and applications of full wavefield migration (FWM).

7.1 Conclusions

As a main conclusion, it was demonstrated that the proposed FWM algorithm properly handles complex scattering effects and allows them to contribute to the imaging process without creating so-called multiples crosstalk. Actually, FWM can be considered as a least-squares migration process that is based on a more correct physical model compared to current approaches.

The involved closed-loop (inversion) concept is based on two major steps: imaging and modelling. The modelling – full wavefield modelling (FWMod) – allows to predict all reflection events with a non-linear physical model for which, given the migration velocity model, the subsurface reflectivities are the only parameters. It is based on the Bremmer series and involves an iterative computation of the downgoing and upgoing wavefields. These wavefields include all the complexities (multiple coda and transmission effects) that constructively contribute (in terms of illumination) to the imaging when such wavefields are used in the imaging process.

As any imaging algorithm, FWM requires a migration velocity model that should be decently accurate. It follows the same requirements as any other least-squares migration algorithm, which is flatness of the resulting common image gathers in angle domain.

The data to be imaged (receiver-side wavefield) should contain either the total set of reflection events or separated primaries (and their internal multiples) or separated surface multiples (and their internal multiples). Depending on this choice of the input data a corresponding source-side wavefield should be used such that after applying the forward model, it will only match events that are present at the receiver-side. For imaging the primaries the correct source wavelet is required. It is important to use the source with correct amplitudes in order to estimate the reflectivity in a 'true-amplitude' sense, which in turn is extremely critical for generating the non-linear events (internal multiples). In chapter 5 it was discussed that the source estimation can be achieved using FWMod in adjoint mode.

An appealing feature of FWM is that it can correctly address the multiples even using the data with asymmetric source/receiver sampling. The latter can be the case for a coarse shooting, ocean bottom node and some 3D geometries. In Chapter 5 it was shown that FWM can also be used as a data reconstruction method, where a modeled wavefield can be inserted in the missing traces of the measured data.

Furthermore, in Chapter 5 it was discussed that FWM can serve not only for estimating the proper image, but it can also provide the wavefields at every grid-point, which means that FWMod can be used not only for data reconstruction, as mentioned before, but also for deblending simultaneous shot records as well as primaries/surface multiples prediction. The last option can be a good alternative for standard multiple elimination techniques in case of coarse receiver sampling (VSP, OBN surveys).

Thus, it can be concluded that FWM is a viable approach in which multiples play a crucial role in the imaging of the subsurface, especially in those cases where the acquisition is sparse. Because seismic acquisition will never be dense in all spatial directions, methodologies like FWM are essential for properly handling all complex scattering effects, such that 'noise' is transformed into usable signal.

7.2 Recommendations for further research

This section considers some aspects of the method that still require some more research. The reader is also invited to read the appendices.

7.2.1 Using the estimated wavefields

The FWM approach can be considered not only from the reflectivity estimation point of view. We need to realize that the method estimates wavefields in the subsurface first by estimating the reflectivities. Given the estimated wavefields many applications become available. In this thesis some of the applications were shown in Chapter 5 (i.e. data reconstruction, prediction of surface multiples, primaries and unblended shot records). More applications can be developed given the wavefields provided by FWM.

7.2.2 More accurate and complete FWMod

Because the forward model of the method is based on the (generalized) Bremmer series approach, the propagation has a preferred direction (usually up and down) and, therefore, has a limitation in terms of the involved propagation angles. In Chapter 4 we proposed to use a pragmatic approach of using not only downgoing/upgoing wavefields but also adding to them separate leftgoing/rightgoing wavefields, where the preferred direction is horizontal. Two pairs of these wavefields can intercommunicate with each other using the common scattering term. However, the more correct approach is discussed in Wapenaar and Grimbergen (1996) and Grimbergen et al. (1998), where it is mentioned that, within the generalized Bremmer series theory, lateral variations of the medium are taken into account in the propagation operator.

In the discussion of Chapter 4 we also realized that it is possible to capture vertical structures by imaging the additive transmission coefficients $\delta\mathbf{T}$. Note that actually the sum of propagation operator \mathbf{W} and additive transmission $\delta\mathbf{T}$ operator probably can result into the operator discussed in Wapenaar and Grimbergen (1996). This proposal, together with proper incorporating of diving waves (discussed in Chapter 4), requires more research.

7.2.3 Geometrical spreading in 2D FWM

Another major issue mentioned in Chapter 6 is related to geometrical spreading that is not properly handled when applying 2D FWM to a 2D line of 3D field data. It was observed that the more shallow the sea bottom, the more difficulties this effect creates. For deep water data the geometrical spreading effect can be neglected and a single correction, like scaling the data with \sqrt{t} , is sufficient. However, datasets with a water bottom of 200m depth or shallower this issue was significantly present. For such datasets a brute-force approach for dealing with it is to apply gain correction to the data by guessing the most optimal damping parameter. Another approach is to take into account the geometrical spreading in 2D propagation, as discussed in Appendix B.

7.2.4 Complex-valued angle-dependent reflectivity

Angle-dependent reflectivity allows to model reflected events more correctly in terms of AVO variations. However, real-valued angle-dependent reflection coefficient may be not sufficient as reflection beyond critical angles also implies a phase-change. In Appendix A it is also shown how complex-valued angle-dependent reflectivity can be parameterized. However more research need to be done to find optimal strategies for bringing this in the FWM process (see also Appendix A).

7.2.5 Extension to 3D

The FWM approach in 3D becomes very expensive. Especially in the case of angle-dependent reflectivity parameterisation. More careful performance optimization should be carried out in order to achieve field data results with reasonable calculation times. Pre calculating wavefields and storing them on disk can be an example. Additionally, it would be beneficial to save wavefields only at the specific grid-points where corresponding reflectivity value is higher than a certain threshold, which can optimize memory usage and still allows keeping the wavefields in memory that are used for the modelling of the multiple scattering. Appendix C shows some computation aspects for the three-dimensional case.

Using surface multiples in 3D becomes even more important because they can drastically reduce the number of shot-records. This was also show in the OBN example in Chapter 6.

7.2.6 Transmission effects

FWM includes also the transmission effects. However, as described in more detail in Appendix A1 and A2, the FWM process needs a dense enough sampling in the depth domain in order to properly represent reflection properties. On the other hand, for arriving at physically correct transmission effects, reflection information should be concentrated as much as possible. Therefore, more research is required in including e.g. sparsity constants for reflectivity, especially for correct inclusion of transmission effects.

7.2.7 Elastic case and other effects

Generally if some phenomena is missing in the forward model and its effect is clearly present in the data, its misexplanation by the forward model will leak in one or another parameter (same as crosstalk for multiples, which was extensively discussed in this thesis).

Therefore, in the 'acoustic' implementation of FWM all converted waves will be imaged as noise, such that its presence in the model space will explain the data as much as possible. To include them properly, the current FWM model needs to be extended to include converted waves as well. Some indications are described by Berkhout (2014a). Derivation of the forward model and obtaining the gradients for this extension is subject to future research, although it is clear that the PS, and SS coefficient of the reflectivity from below should be easily accessible which is not yet trivial for the transmission operators and reflectivities from below.

Other effects, such as anisotropy and attenuation can be included by modifying the propagation operator. In this sense, the forward model of FWM is very flexible and allows to include such 'modules' of complexities quite easily, for instance, only in the areas of interest without implementing those boundaries conditions elsewhere

in the model. Note that this is not easily accomplished in other modeling methods, such as finite difference or finite elements methods.

Appendices



Practical observations

This section contains some practical observations that were made during the research. In this appendix we would like to address convergence issues, model space parameters, parameterisation itself and the staring model issue.

A.1 Model sampling

This section shows the effect of the model space sampling. The motivation is that for a closed-loop algorithm it is important that the model space is sampled such that the original surface data can be reconstructed. For this test FWM was performed on the input data shown in Figure 1.4 with three different sampling intervals across the depth direction. Note that the input data was modeled with a depth sampling of 5m.

Figure A.1 shows the energy (normalized to one) of the residuals versus iteration number for three different depth samplings: 10, 5 and 2.5 meters. As can be observed the best data matching (between observed and the modeled data) happens in the case of a depth sampling of 5 meters (green curve). Poorer results were obtained when the image depth sampling was 10 meters (blue curve), which can be explained by a lack of parameters, which resulted in under-sampling (depth aliasing) of the model space. However, using more samples does not provide a better result – as is visible in the red convergence plot, which represents the case of a 2.5 m sampling. This case can be explained in a way that too many model samples were 'competing' to explain the same sample in the data domain, which slows down the convergence.

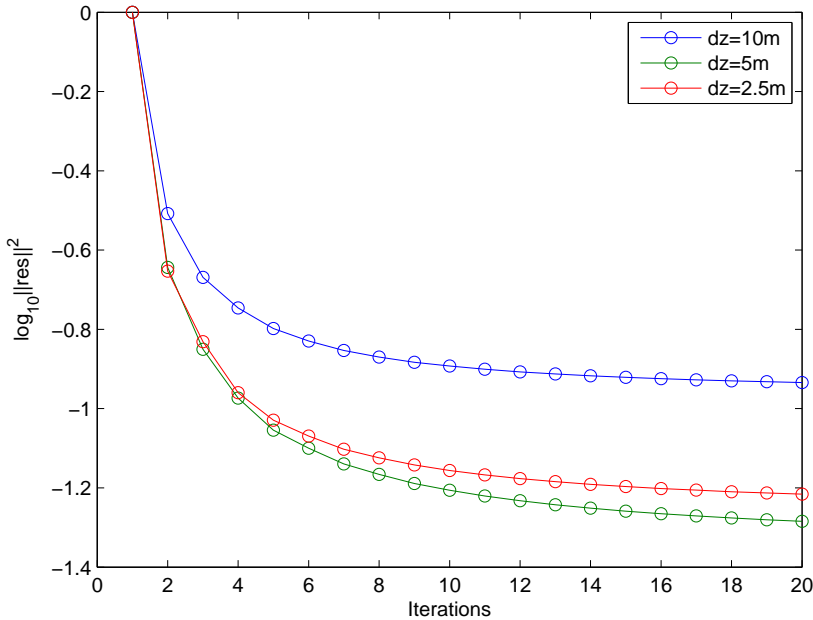


Figure A.1: Convergence plot for three different depth sampling cases: 10m (blue), 5m (green) and 2.5m (red).

A.2 Transmission effects

Due to the band-limited frequency range of the measured data, the reflectivity (image) can only be estimated in a band-limited way. In this section we would like to demonstrate that such band limitation of the reflectivity can affect the forward modeling.

Every grid-point of the subsurface can generate the scattering with a 'strength' proportional to the reflectivity value at this point. Therefore, in case a single reflector is imaged with side-lobes, spurious internal multiples can be generated by this reflector (as it covers a few samples along the depth axis). Side-lobes can also affect the transmission effects, as transmission will happen not only at the peak of the reflector (as it should be), but also at the side lobes that can have a polarity opposite to the main peak, thus biasing the total transmission effect. The effect of band-limitation for the reflectivity creates smaller problems than for the transmission, because reflectivity estimation is driven by the criteria of matching the modeled data with the observed data. However, there is no direct criterion for the effect of

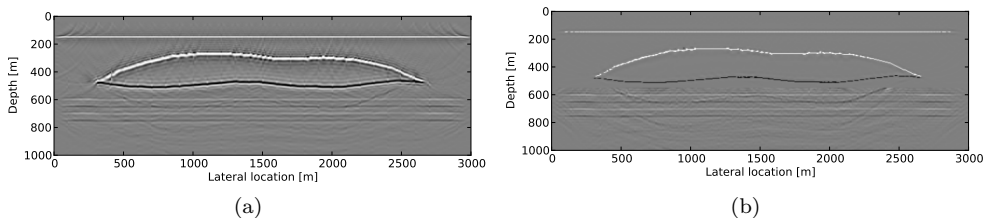


Figure A.2: FWM image obtained without (a) and with (b) sparsity constraint.

transmitted data.

Biased transmission effects mean that the secondary sources have incorrect amplitudes. Therefore, the amplitude of the deeper reflectors are consequently affected. This is similar to the situation when the data is imaged by using the source wavelet with an incorrect amplitude: reflectors that mainly generate internal multiples are estimated with wrong amplitudes and, thereby, it will lead to inefficient crosstalk suppression.

The aforementioned effect means that obtaining a high-resolution image without strong side-lobes is important for obtaining accurate results for transmission effects and internal multiple prediction. Therefore, the imaging of data that is as broadband as possible is preferred. If not accessible, an alternative is to imply a constraint by adding an additional penalty function that promotes sparsity for the estimated reflectivity (i.e., a L1 or Cauchy constraint). Another solution can be applying data deconvolution (frequency spectrum equalizing) as preprocessing, which can result in the data to be more 'spiky'.

Figure A.2 shows two reflectivity images obtained with and without a sparsity constraint. The sparsity constraint was applied only to the area of the salt body in order to make its reflectivity sharper.

Figure A.3 shows the effect of the reflectivity sharpness on the transmission effect. In Figure A.3 it demonstrated that in/ case of using constrained reflectivity of Figure A.2b, both transmitted and reflected parts of the wavefield are modeled accurately and the result is very close to the reference finite-difference modelling result shown in Figure A.3a. However, when a band-limited image is used (Figure A.2a) it is visible that, although the reflected component is modeled adequately, the transmitted part of the wavefield is about two times weaker than the result of finite-difference modelling (see Figure A.3c).

The aforementioned example demonstrates that for correct modeling of transmission effects it is very important to estimate reflector reflectivity as sharp as possible. When the frequency content of the data does not allow us to estimate such reflector it is possible to apply the Cauchy constraint in the inversion process. However this constraint can also distort the amplitude ratio of weak reflectors (Schouten, 2012). Therefore, it is possible to consider FWM not only to estimate the reflectivities but also the wavefields. Hence one can perform FWM with a sparsity constraint in order

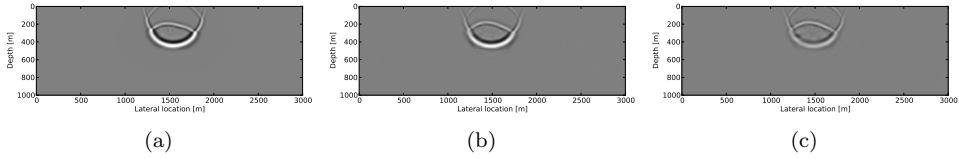


Figure A.3: Snapshots of: (a) data modeled by finite-difference (reference), (b) one FWM roundtrip using a sparse reflectivity image and (c) one FWM roundtrip using the reflectivity obtained without additional constraints.

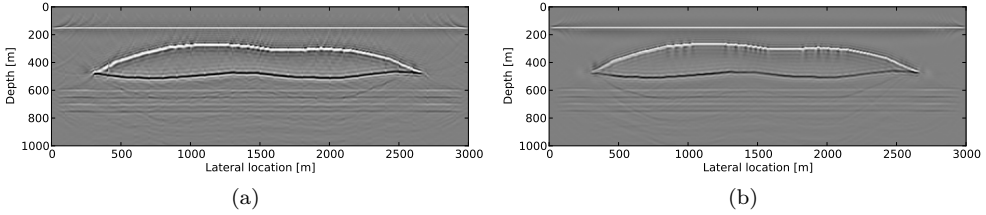


Figure A.4: a) Standard FWM image and b) FWM image obtained in a two-step approach where firstly wavefields are obtained by estimated sparse reflectivity image and then given the wavefields the image is re-estimated.

to obtain wavefields with properly modelled transmission effects. Next, given the modeled wavefields, a closed-loop inversion can be performed where the wavefields are fixed since they are physically correct and only reflectivities are updated. Figure A.4 shows a comparison of the standard FWM image with image obtained via the described two-step. In this case the Cauchy constraint, as described in Chapter 3, was used for the sparseness penalty.

A.3 Starting model

Angle-dependent parameterisation means that every grid-point is represented by a vector containing reflection coefficients versus angle. This allows to explain the data with a large freedom in the model-space. Scenarios are possible when the crosstalk from the multiples is still present but the data is already explained, meaning that the current residual does not contain any valuable information for a further reflectivity update.

To avoid such undesired null-space solutions is to start angle-dependent FWM from a proper starting reflectivity model. A logical proposal is a starting image obtained from angle-independent FWM (structural imaging represented by only one reflectivity scalar per grid-point) where the input data was a subset with reduced offsets, such that AVO effects in the sub-selected data are not strong.

The structural image can be translated to the angle-dependent version simply

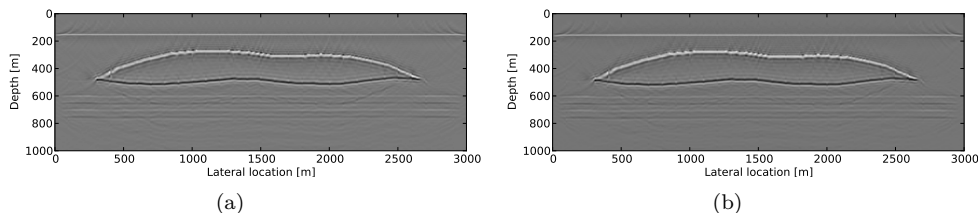


Figure A.5: a) FWM image from small-offset data and b) averaged angle-dependent reflectivity.

by copying the image at all angles (ray parameters). Thus, it can be interpreted as a constant function versus angle or a spike-function in terms of the spatial local offset (similar to using a diagonal reflectivity matrix in the angle-independent parameterization).

The following numerical example demonstrates the usage of the starting model. Figure A.5a shows the image obtained by angle-independent FWM for data with offsets limited up to 300 meters. Such short range allowed to perfectly explain the data using the simplest parameterisation and suppresses the crosstalk from internal multiples. Figure A.5b demonstrates the FWM image as obtained in the angle-dependent mode (this is a sum of all angles, representing average), using the starting model shown in Figure A.5a but using all offsets available (up to 3000 meters). The stacked image obtained by angle-dependent FWM is slightly improved over the structural one: note the difference of the top salt expressed by the mitigated side lobe and a reduction of cross-talk in the deeper part.

Figure A.6a shows the image gather (lateral location slice at $x=1500\text{m}$) of FWM in the angle-dependent mode obtained without any starting model. Figure A.6b shows the result of the angle-dependent mode but when the angle-independent starting model was used. It is visible that some (non-flat) crosstalk events are better suppressed. Note that the imprint of the starting model is clearly visible. It is also visible that the area between the dashed curves is the area covered by the reflection and, therefore, is sensitive to updates of the angle-dependent approach.

Both estimated parameters explain the data sufficiently good when used in the forward model. This indicates that the angle-dependent version of the method is overcomplete and the final result depends on the starting model.

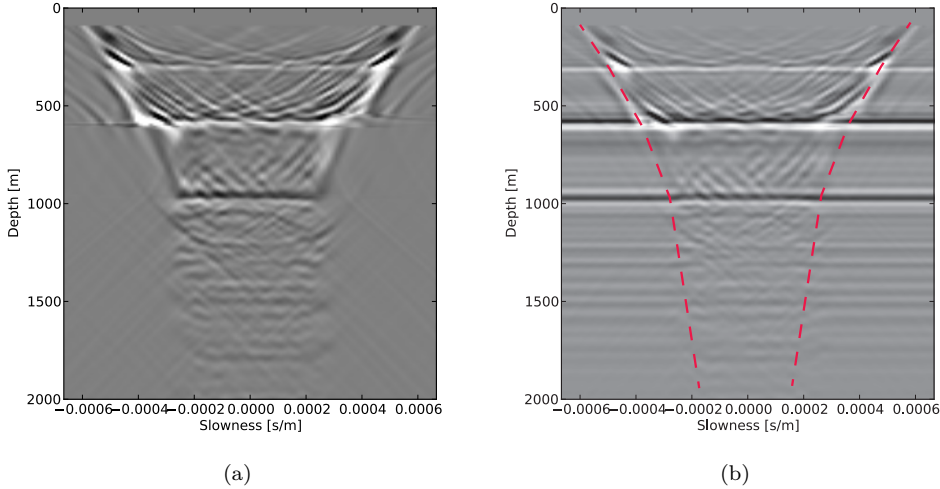


Figure A.6: Image gather at the location $x=1500\text{m}$ after 10 iterations starting from scratch (a) and starting from angle-independent image (b).

A.4 Complex-valued angle-dependent reflectivity estimation

In this section we focus on the special case of angle-dependent FWM. As described in Chapter 3, estimation of angle-dependent reflection coefficients is performed via calculation of the so-called AVP function that represents the zero-time selection of the Radon-transformed reflectivity gradient. In the described case the estimated AVP function is real-valued, which means that post-critical effects will not be modeled accurately.

The real-valued AVP function is computed as follows:

$$\Delta \mathbf{A}(z_n) = 2\text{Re}(\sum_{\omega} \mathbf{L}^H \{[\Delta \mathbf{P}(z_n)]^- [\mathbf{P}^+(z_n)]^H\}). \quad (\text{A.1})$$

In order to make AVP function complex-valued we extend the imaging condition as follows:

$$\begin{aligned} \Delta \mathbf{A}_r(z_n) &= 2\text{Re}(\sum_{\omega} \mathbf{L}^H \{[\Delta \mathbf{P}(z_n)]^- [\mathbf{P}^+(z_n)]^H\}) \\ \Delta \mathbf{A}_i(z_n) &= 2\text{Re}(\sum_{\omega} \mathbf{L}^H \{[-i\Delta \mathbf{P}(z_n)]^- [\mathbf{P}^+(z_n)]^H\}), \end{aligned} \quad (\text{A.2})$$

such that $\Delta \mathbf{A} = \Delta \mathbf{A}_r + i\Delta \mathbf{A}_i$. In this way we allow the reflected wavefield to have a phase different from the incident one as is required for correct description of post-critical reflection.

In the next numerical example (shown in Figure A.7) we consider the observed data for a simple model of one horizontal reflector at 100 meters with a velocity

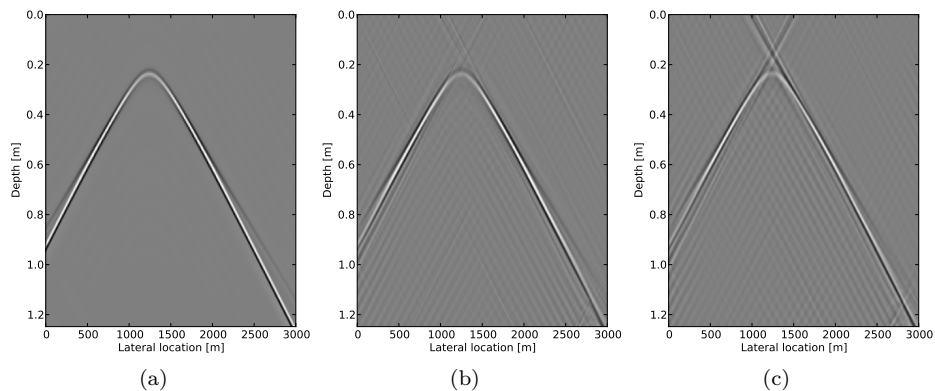


Figure A.7: a) Observed data from a horizontal velocity contrast reflector at a depth of 100 meters; b) Modeled data by angle-dependent FWMod using a complex-valued AVP function; c) Modeled data by angle-dependent FWMod using a real-valued AVP function.

change from 1500 m/s to 1800 m/s. We compare it with the data modeled by complex-valued reflectivity (Figure A.7b) and with the data modeled by an estimated real-valued reflectivity (Figure A.7c). We allowed to estimate the reflectivity only at the depth level of the actual reflector in order to avoid parameter leakage. It is visible that FWM based on complex-valued reflectivity does a more accurate job than the FWM version based on the real-valued reflectivity. Note that the head wave is more accurately modeled as well as phase rotation of the event in the complex-valued case.

B

Theoretical observations

This appendix considers the main components of FWM (propagation and scattering operators) from the perspective of the acoustic wave equation. The possibility of including 3D geometrical spreading effects in 2D propagation operator using a so-called 2.5D wave equation is demonstrated in the second half of this appendix.

B.1 Link with one-way wave equation

Let's consider the acoustic 2D wave equation in a homogeneous medium specified by velocity c :

$$(\partial_{xx} + \partial_{zz} + \frac{\omega^2}{c^2})U(x, z, \omega) = 0. \quad (\text{B.1})$$

In the wavenumber-frequency domain this equation takes the following form:

$$(\partial_{zz} - k_x^2 + k^2)\tilde{U}(k_x, z, \omega) = 0, \quad (\text{B.2})$$

where $k = \omega c^{-1}$. Equation B.2 can be factorized as follows:

$$(\partial_z - ik_z)(\partial_z + ik_z)\tilde{U}(k_x, z, \omega) = 0, \quad (\text{B.3})$$

where $k_z = \sqrt{k^2 - k_x^2}$. Equation B.2 can be decoupled into two one-way wave equations:

$$\begin{aligned} (\partial_z - ik_z)\tilde{U}(k_x, z, \omega) &= 0 \\ (\partial_z + ik_z)\tilde{U}(k_x, z, \omega) &= 0, \end{aligned} \quad (\text{B.4})$$

which, respectively, have two following solutions:

$$\begin{aligned}\tilde{U}(k_x, z, \omega) &= \tilde{U}_0(k_x, \omega)e^{-ik_z z} \\ \tilde{U}(k_x, z, \omega) &= \tilde{U}_0(k_x, \omega)e^{ik_z z}.\end{aligned}\tag{B.5}$$

Therefore, if the wavefield is known at some depth level $z = 0$ it can be extrapolated to $z = \Delta z$ as:

$$\tilde{P}(k_x, \Delta z, \omega) = \tilde{P}(k_x, 0, \omega)e^{\mp ik_z \Delta z}.\tag{B.6}$$

In more details, in case of $\Delta z > 0$ the first solution (written in Equation B.5) is responsible for forward-in-time and downward-in-space wavefield extrapolation and in case of $\Delta z < 0$ it extrapolates the wavefield backward-in-time and upward-in-space. In its turn, in case of $\Delta z > 0$ the second solution in Equation B.5 performs forward-in-time upward-in-space and in case of $\Delta z < 0$ it extrapolates the wavefield backward-in-time and downward-in-space.

In order to perform one-way wavefield extrapolation one need to multiply the wavefield $\tilde{P}(k_x, 0, \omega)$ by the phase-shift operator $e^{\pm ik_z \Delta z}$. As it can also be seen from Equation B.6 it produces phase-shift extrapolation but it does not affect amplitudes, except on the evanescent part ($k_z^2 < 0$) when k_z becomes complex and, hence, the whole exponent argument becomes real-valued, which leads to amplitude decay.

It is clear that an imaging algorithm based on wavefield extrapolation described by Equations B.5 will be quite naive in case of dealing with complex inhomogeneous media. At least two problems arise: no horizontal variations of the propagation velocity $c(x)$ and no scattering effects due to inhomogeneities are taken into account.

To overcome the first problem, propagation operator \mathbf{W} can approximately include lateral variations by changing the convolution operator according to the local velocity values (Thorbecke et al., 2004). However, this procedure assumes that lateral velocity variations are mild.

The more accurate, but on the another hand more computationally demanding solution, is to consider discretized Helmholtz operator \mathbf{H}_2 (being based on the left-hand side of the Equation B.1), which can be written as follows:

$$\mathbf{H}_2 = \begin{bmatrix} k_1^2 & 0 & 0 & \dots & 0 \\ 0 & k_2^2 & 0 & \dots & 0 \\ \dots & \dots & \dots & \dots & \dots \\ 0 & 0 & 0 & \dots & k_n^2 \end{bmatrix} + \frac{1}{\Delta x^2} \begin{bmatrix} -2 & 1 & 0 & \dots & 0 \\ 1 & -2 & 1 & \dots & 0 \\ \dots & \dots & \dots & \dots & \dots \\ 0 & 0 & 0 & \dots & -2 \end{bmatrix}.\tag{B.7}$$

In analogy to Equations B.2 and B.4 the wave equation can be written as:

$$\mathbf{H}_2 \mathbf{u} = \mathbf{H}_1 \mathbf{H}_1 \mathbf{u} = 0,\tag{B.8}$$

where \mathbf{u} is a discretized wavefield vector and \mathbf{H}_1 is a square-root operator of \mathbf{H}_2 . In Grimbergen et al. (1998) it was shown that propagation operator \mathbf{W}_1 can be constructed, roughly speaking, as follows:

$$\mathbf{W}_1 = e^{-i\mathbf{H}_1 \Delta z}. \quad (\text{B.9})$$

Operator computed by Equation B.9 can properly include lateral velocity variations. This operator, also mentioned as in (Wapenaar and Grimbergen, 1996), is not only in charge for wavefield extrapolation in an arbitrary inhomogeneous medium, but it also generates the scattering due to the horizontal variations. However, such operators still assume that the velocity model is vertically homogeneous between the neighboring depth levels.

With regards to the vertical inhomogeneities, the one-way wave equation also neglects it. In Zhang et al. (2003) it was discussed that one-way wave equation does not yield correct amplitudes as the two-way wave equation. In that paper the authors introduced a special real-valued term (proportional to the vertical derivative of the propagation velocity $\partial_z c$) that can be added to the argument of the exponent from Equation B.4 such that the amplitude of the propagated wavefields will be compensated. However, besides the amplitudes, this approach does not take into account scattering effects - internal multiples and transmission. Wapenaar and Grimbergen (1996) discuss that vertical scattering can be incorporated as a generalized Bremmer series (Corones, 1975). In FWMod, being based on Bremmer series approach, such vertical variations are compensated differently - via vertical scattering term (mentioned as in Wapenaar and Grimbergen (1996) or denoted as $\delta\vec{S}$ in this thesis), which involves reflection and transmission of the wavefields modeled in a one-way manner. It is interesting to mention that reflectivity is also proportional to the vertical variations of propagation velocity. But on top of that $\delta\vec{S}$ includes also vertical variations of densities.

Returning back to the horizontal inhomogeneities, usually such variation are not known in advance (as they are detected mainly at the imaging step and usually not so detailed migration velocity models are provided). Therefore, during the inversion process it is convenient to consider pure propagation operators, whereas horizontal scattering can be included via a separate orthogonal propagation process or in the estimated additive transmission operators $\delta\mathbf{T}$, as was shown in Chapter 4.

B.2 Including geometrical spreading

Whereas 3D FWM automatically considers geometrical spreading effects, the 2D version of the algorithm is based on two-dimensional wavefield extrapolation. Therefore, when a 2D subset of field data is imaged, FWM will calculate underestimated reflection coefficients as the amplitude of the modeled wavefields do not represent the observed geometrical spreading, hence the incident wavefield will be stronger than it should be. In this subsection we try to modify the propagation operator such that it will take this effect into account.

We consider the so-called 2.5D (two-way) wave equation derived by Liner (1991):

$$(\partial_{xx} + \partial_{zz} + \frac{\omega^2}{c^2} + i\omega\frac{c}{r} + \frac{1}{r^2})U(x, z, \omega) = 0. \quad (\text{B.10})$$

This equation is similar to Equation B.1 but it contains two additional terms that mimic the three-dimensional Green's function for the two-dimensional case. The last two terms can be introduced in the numerical implementation as a diagonal matrix containing $\text{diag}(\frac{ik(x)}{r(x)} + \frac{1}{r^2(x)})$, where $r(x) = \sqrt{(x - x_s)^2 - z_r}$ is a distance from the source located at the surface at x_s to the subsurface grid-point with coordinates (x, z_r) . Note that the 2.5D one-way propagation operator can be specified only for one shot (because it contains $r(x)$ that is different from one shot record to another), which does not allow to 'sink' all shot records using one \mathbf{W} operator. For modelling the downgoing wavefield from one source, we consider the new \mathbf{H}_2 operator as a matrix (including additional terms) as discussed previously (see Equation B.9). The new \mathbf{H}_2 handling 2.5D propagation effects looks as follows:

$$\mathbf{H}_2 = \begin{bmatrix} k_1^2 + \frac{i\omega c_1}{r_1} + \frac{1}{r_1^2} & 0 & 0 & \dots & 0 \\ 0 & k_2^2 + \frac{i\omega c_1}{r_1} + \frac{1}{r_1^2} & 0 & \dots & 0 \\ \dots & \dots & \dots & \dots & \dots \\ 0 & 0 & 0 & \dots & k_n^2 + \frac{i\omega c_1}{r_1} + \frac{1}{r_1^2} \end{bmatrix} + \frac{1}{\Delta x \Delta z} \mathbf{D}_2, \quad (\text{B.11})$$

where \mathbf{D}_2 is a spatial second derivative matrix (same as in Equation B.7).

In this manner it is possible to compute 2.5D one-way recursive propagation operators. Note, that at some depth the terms containing $r(x)$ will vanish and therefore after some point it is convenient to consider the conventional propagation operator again.

The aforementioned is demonstrated on the following example. The three layer velocity model – with velocities 1500 m/s for the first layer, 2000 m/s for the second one and 3000 m/s for the last one (see Figure B.1a) – is used for propagation of the source wavelet injected at the surface at the lateral location of $x = 1500\text{m}$. The snapshot of the recursively propagated wavefield based on the conventional 2D \mathbf{W}

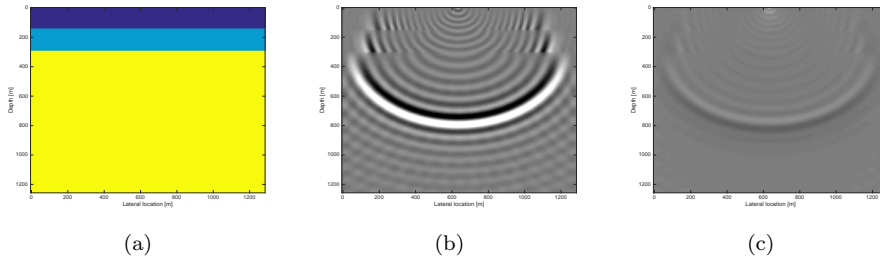


Figure B.1: (a) Velocity model, (b) snapshot of the 2D propagated wavefield and (c) snapshot of the 2.5D propagated wavefield.

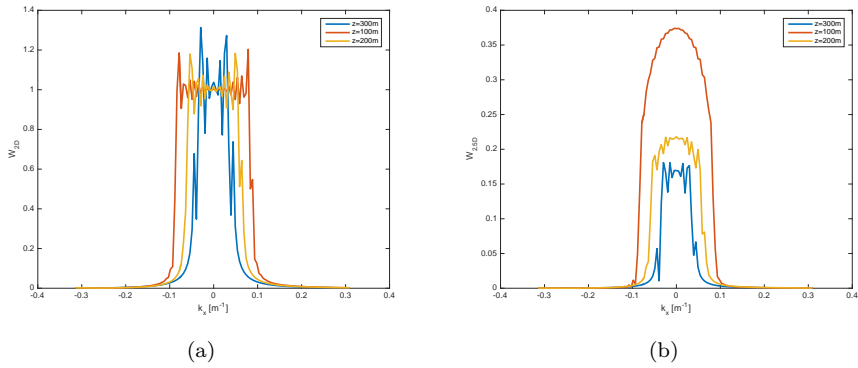


Figure B.2: FK-spectra of 2D propagated wavefield (a) and 2.5D propagated wavefield (b).

operators is shown in Figure B.1b. The result for using the described 2.5D operator is shown in Figure B.1c and it is visible that amplitudes of this wavefield are more attenuated.

Moreover, Figure B.2 compares the FK spectra of these two wavefields at different depth levels. It is visible that the spectrum of the 2D modeled wavefield, neglecting some numerical artifacts, is close to 1 at each depth level, as expected (Figure B.2a), whereas two-and-half-dimensional wavefield (Figure B.2b) has an angle-dependency of the spectra, which complies with the spectra of the wavefield propagated in 3D media when selected along one spatial coordinate.

C

3D implementation

In this appendix an extension of the presented FWM methodology to the third spatial dimension is studied. In general, the method as described in Chapters 2 and 3 remains the same, as all matrix equations can be interpreted in a full 3D sense, as was already mentioned in Chapter 2. However, the extra dimension forces to reconsider the implementation due to the high computational costs.

It is visible in Figure C.1 that the 3D FWM approach is based on the same flow as the 2D version. The FWMod algorithm (pseudo code) is shown in Algorithm 1. Although the algorithm looks identical to the already introduced 2D version, pitfalls are hidden in the first and in the third step of the algorithm: estimating the angle-dependent reflection coefficients and the wavefield propagation. Besides that the requirement of storing the up- and downgoing wavefields in 3D can already be challenging for one physical experiment. Therefore, keeping all the shots in RAM might not be suitable and parallelization and/or disk storage should be taken into consideration. Hence, each shot in 3D most probably has to be processed separately. The whole algorithm can be easily parallelized (parallel blocks are displayed in Figure C.1) as wavefields can be computed independently for each frequency and shot experiment, while the only shared variable that should be computed from all wavefields is the reflectivity. Therefore, the gradient computation and reflectivity updating blocks serve as a barrier in the computational flow. For every iteration of FWM parallel segments should be synchronized at least twice: when computing the gradient, as it requires contribution from the complete data, as well as when updating the reflectivity.

Algorithm 1 FWMod roundtrip

```

for each shot  $k$  do
  for each frequency  $\omega$  do
    go down (+) and then up (-)
    for each depth level  $z_n$  do
      1. calculate the scattering:
       $\delta\vec{S}(z_n) \leftarrow \delta\mathbf{T}^\pm(z_n)\vec{P}_k^\pm(z_n) + \mathbf{R}^\mp(z_n)\vec{P}_k^\mp(z_n)$ 
      2. include the scattering:
       $\vec{Q}^\pm(z_n) \leftarrow \vec{P}_k^\pm(z_n) + \delta\vec{S}_k(z_n)$ 
      3. propagate and save the wavefield:
       $\vec{P}_k^\pm(z_{n\pm 1}) \leftarrow \mathbf{W}\vec{Q}_k^\pm(z_n)$ 
    end for
  end for
end for

```

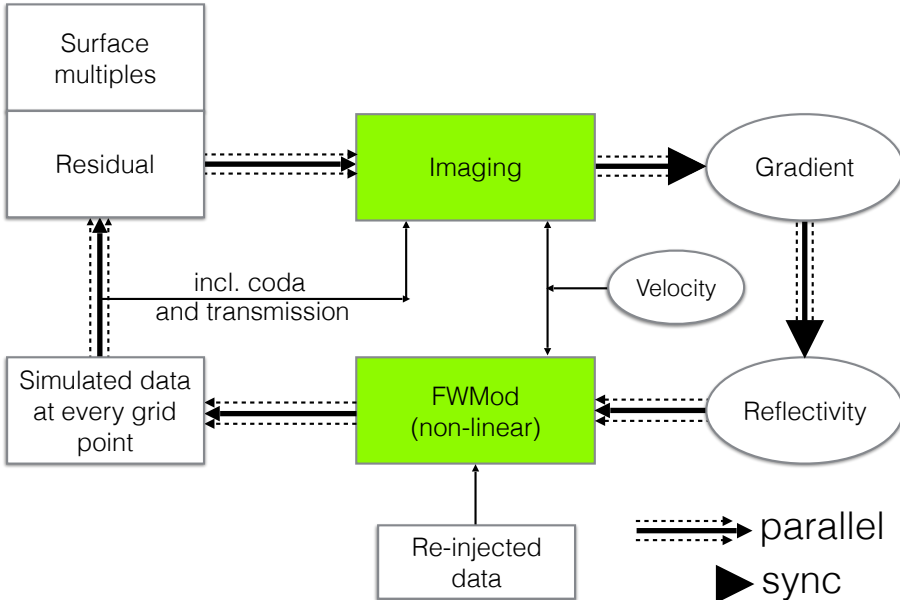


Figure C.1: The FWM closed-loop process and its possibility to compute it in parallel. Almost all blocks can be computed independently in parallel, but have to be synchronized for computing the gradient and updating the reflectivity, because the last two procedures require to gather the contributions from all shots and all frequency slices.

C.1 Propagation operators in 3D

Lateral inhomogeneities in two dimensions were easily handled by considering \mathbf{W} as a laterally varying spatial convolution operator kernel that depends on the local velocity. In the three-dimensional case, using the same approach, it becomes a 2D convolution operator. Note that for 3D wavefield propagation it might be more attractive to use the approach called 'phase-shift plus interpolation' (PSPI) (Gazdag and Sguazzero, 1984) that is based on several extrapolations within few homogeneous layers defined by a few reference velocities, followed by interpolation of those results according to the actual local velocity. For each reference velocity the extrapolation is efficiently calculated via the double wavenumber domain. The number of reference velocities can vary at each level, depending on the velocity complexity of the depth slice.

C.2 Reflectivity operator

It was already discussed in Chapter 3 that reflection at each depth level can be described in two modes: angle-dependent and angle-independent. The most simple way is to consider the reflectivity that is parameterized by one scalar coefficient per grid-point. In this way the reflectivity operator also serves as point-by-point multiplication of the wavefield with the corresponding reflectivity scalar value at the specific location. Computation of such scalar is described in the simple Algorithm 2. This means that the reflectivity matrix for the 3D case still remains a diagonal matrix.

For more accurate, angle-dependent modeling, the procedure also becomes a two-dimensional convolution process. In order to calculate such 2D convolution kernel, a 2D angle gather should be computed in the first place. Computation of such gathers is done by applying the so-called 2D extended imaging condition (i.e. imaging condition with spatial lags h_x and h_y with respect to two opposite wavefields). This step is introduced as step one in the Algorithm 3 and is also illustrated in Figure C.2. For every lateral location, indicated by the blue point in Figure C.2, the downgoing wavefield at this location $P_k^+(x, y, z_n, \omega)$ is cross-correlated with the back-propagated residual but slightly shifted in space by a 2D spatial lag $\Delta P(x - h_x, y - h_y, z_n, \omega)$. In this way the spatial lag brings the angle information: zero-lag captures the information from (close to) normal incidence, while larger lags capture information from the larger angles.

After that, a 2D Radon transform is applied to each $\Delta \mathbf{R}(x, y, \omega)$ matrix that maps the spatial lags (h_x, h_y) to ray-parameters (p_x, p_y) and stacks them over all frequencies. This results in the 3D angle gathers $A(p_x, p_y, x, y, z_m)$ or $\mathbf{A}(x, y, z_m)$.

The \mathbf{R} operator describes the 2D convolution using the kernel that can be constructed from the just described 3D angle gathers \mathbf{A} . It can be done by applying the inverse 2D Radon transform for each frequency slice of interest. In this way,

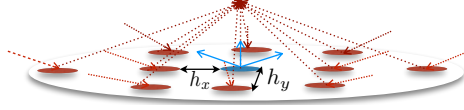


Figure C.2: Schematic illustration of the extended imaging condition in 3D.

the process is very similar to the procedure developed in 2D. Such procedure is also described in Algorithm 4. For example, the reflected upgoing wavefield can be described as:

$$P_k^-(x, y, z_n, \omega) = \sum_{h_x} \sum_{h_y} R(h_x, h_y, x, y, z_n, \omega) P_k^+(x + h_x, y + h_y, z_n, \omega), \quad (\text{C.1})$$

which in vector form can be written as:

$$\vec{P}_k^-(z_n) = \mathbf{R}(z_n) \vec{P}_k^+(z_n). \quad (\text{C.2})$$

Such computations become very expensive. When the angle-independent approach is used, the estimation of the reflectivity can be done by only one imaging condition. In the 2D angle-dependent mode, the number of imaging conditions is given by n_{h_x} imaging conditions per grid point and the following Radon transform it increases to $n_{h_x} n_{h_y}$ imaging conditions followed by 2D Radon transforms for each frequency. In addition, it applies to $n_x n_y$ locations per depth level. Such expensive estimation of angle gathers for 3D data might be a bottle-neck for the algorithm and further optimization of the scheme (such as investigating the symmetry of the convolution operator) is recommended.

Algorithm 2 Angle-independent imaging

```

for each  $x$  location do
  for each  $y$  location do
    1. apply imaging condition:
       $\Delta R(x, y, z_n) \stackrel{\pm}{\leftarrow} [\Delta P_k(x, y, z_n, \omega)] [P_k^+(x, y, z_n, \omega)]^*$ 
    end for
  end for

```

C.3 Numerical example

The following example demonstrates the application of FWM in 3D. First, the angle-independent case is considered. Density and velocity models are shown in Figure C.3a,b respectively. The data was generated using 3D finite-difference modelling without surface multiples. The image at the first iteration is shown in Figure C.3c. The PWM image (Figure C.3d) shows the improved image in terms of resolution and

Algorithm 3 Angle-dependent imaging

```

for each  $x$  location do
  for each  $y$  location do
    1. apply extended imaging condition:
    for each  $h_x$  spatial lag do
      for each  $h_y$  spatial lag do
         $\Delta R(h_x, h_y, x, y, z_n, \omega) \stackrel{\pm}{\leftarrow} [\Delta P_k(x - h_x, y - h_y, z_n, \omega)][P_k^+(x, y, z_n, \omega)]^*$ 
      end for
    end for
    2. apply 2d Radon transform and sum over the frequencies:
     $\Delta \mathbf{A}(x, y, z_n) \stackrel{\pm}{\leftarrow} [\mathbf{L}_{h_x} [\mathbf{L}_{h_y} \Delta \mathbf{R}(x, y, z_n, \omega)]^T]^T$ 
  end for
end for

```

Algorithm 4 Angle-dependent reflectivity operator

```

for each  $x$  location do
  for each  $y$  location do
    1. apply extended imaging condition:
    for each  $h_x$  spatial lag do
      for each  $h_y$  spatial lag do
         $\mathbf{R}(x, y, \omega) \leftarrow [\mathbf{L}_{h_x}^* [\mathbf{L}_{h_y}^* \mathbf{A}(x, y, \omega)]^T]^T$ 
      end for
    end for
  end for
end for

```

extended lateral coverage, however, it still contains the internal multiple crosstalk that can be removed by the FWM approach (Figure C.3e). It is also demonstrated in the horizontal slices shown at the top of each cube in Figures C.3b,c,d that the crosstalk is suppressed in all lateral locations (both cross-line and in-line).

The next example demonstrates the angle-dependent parameterisation in 3D. Figure C.4a contains the input data that was imaged (used as a receiver-side dataset). As a subsurface model, one horizontal reflector at $z = 250m$ with a density and a velocity contrast was used.

Figure C.4b shows the modeled data using structural imaging only. Note, that some of the AVO effects are included in the data, that can be explained by the fact that only one shot has been imaged. The modeled data in the angle-dependent mode (shown in Figure C.4c) contains accurate AVO effects due to the angle-dependent parameterisation.

Note that when angle-dependent imaging is applied the reflectivity becomes a five-dimensional array: 2 illumination angles (ray-parameters) at every grid-point defined by three spatial coordinates.

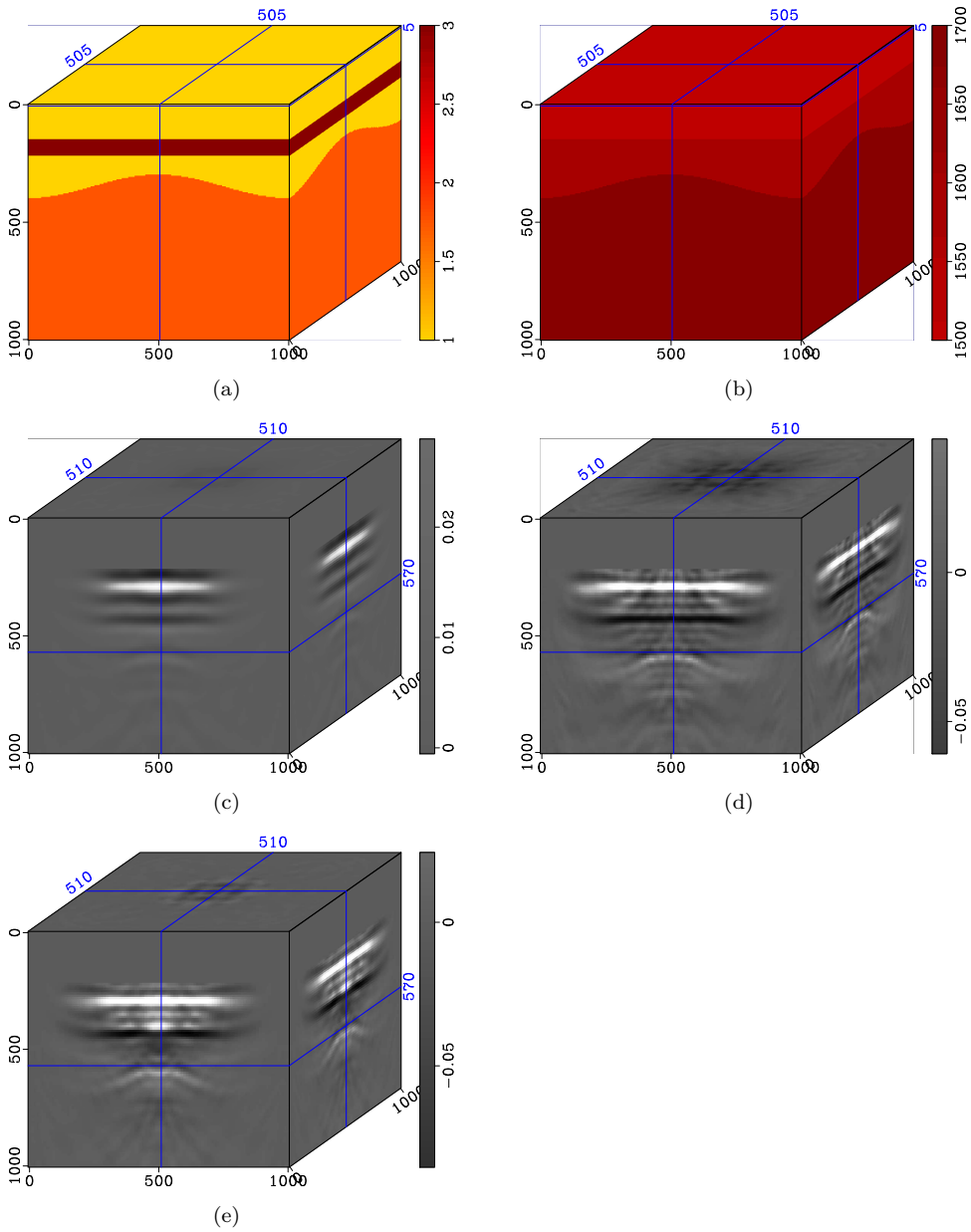


Figure C.3: Angle-independent FWM in 3D. a) Density model; b) Velocity model; c) Image at the first iteration; d) The PWM image after 20 iterations; e) The FWM image after 20 iterations.

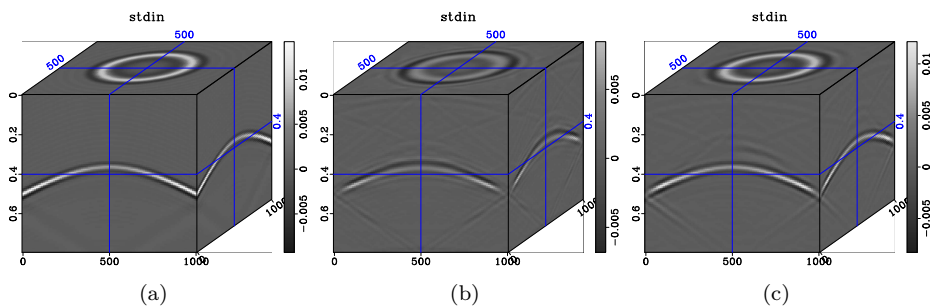


Figure C.4: Angle-dependent FWM in 3D. a) Input data; b) Angle-independent modelling; c) Angle-dependent modelling.

Figure C.5 shows this five-dimensional array in different perspectives. Figure C.5a shows the AVP plot across the one of the lateral directions versus ray parameter across that direction. Note that orthogonal directions will display a similar plot, because of the symmetry of the model. Figures C.5b,c show which ray parameters (angles) illuminate the points $(x=500\text{m}, y=500\text{m}, z=250\text{m})$ and $(x=300\text{m}, y=400\text{m}, z=250\text{m})$ respectively. Note that such parameterization also makes it possible to study which points will illuminate the given ray parameters at the given depth $z=250\text{m}$ (see Figure C.5d,e for two angles of illumination). Note that because this reflectivity operator was calculated from one shot record, it is very sparsely filled.

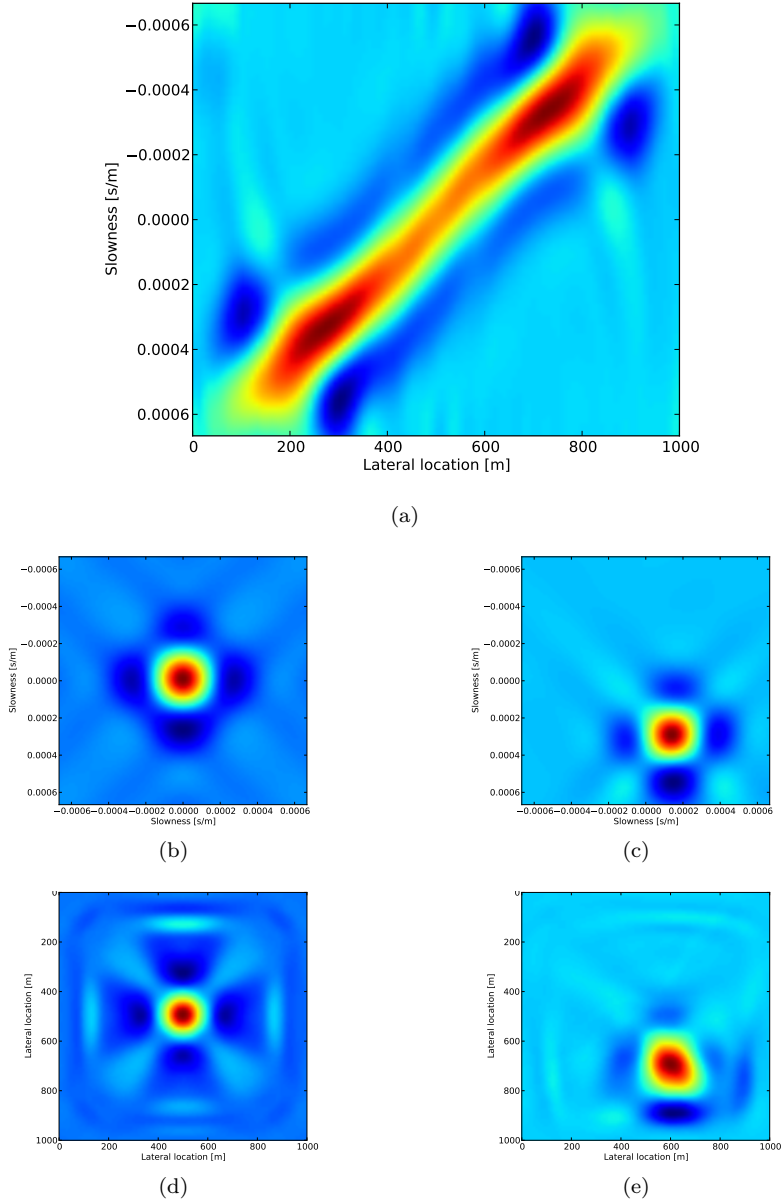


Figure C.5: Angle-dependent FWM in 3D. a) AVP function along x location (y is fixed) b) AVP function at a given grid point ($x=500\text{m}$, $y=500\text{m}$, $z=250$), c) AVP function at a given grid point ($x=300\text{m}$, $y=400\text{m}$, $z=250$) d) Illumination map for normal incidence ray, e) Illumination map for the non-vertical ray.

Bibliography

- Alshuhail, A., Staal, X., Verschuur, D., et al. (2014). Incorporating anisotropy in joint migration inversion. In *2014 SEG Annual Meeting*. Society of Exploration Geophysicists.
- Aminzadeh, F., Burkhard, J. M., Nicoletis, L., Rocca, F., and Wyatt, K. (1994). SEG/EAGE 3-D modeling project: 2nd update. *The Leading Edge*, 13(9):949–952.
- Araujo, F. V., Weglein, A. B., Carvalho, P. M., and Stolt, R. H. (1994). Inverse scattering series for multiple attenuation: an example with surface and internal multiples. pages 1039–1041.
- Baysal, E., Kosloff, D. D., and Sherwood, J. W. (1983). Reverse time migration. *Geophysics*, 48(11):1514–1524.
- Bednar, J. B. (2005). A brief history of seismic migration. *Geophysics*, 70(3):3MJ–20MJ.
- Berkhout, A. J. (1982). *Seismic migration, imaging of acoustic energy by wave field extrapolation, A: theoretical aspects*. Elsevier (second edition). ISBN:0-444-41904-7.
- Berkhout, A. J. (1997). Pushing the limits of seismic imaging, part II: integration of prestack migration, velocity estimation and AVO analysis. *Geophysics*, 62(3):954–969.
- Berkhout, A. J. (2008). Changing the mindset in seismic acquisition. *The Leading Edge*, 27(7):924–938.
- Berkhout, A. J. (2012). Combining full wavefield migration and full waveform inversion, a glance into the future of seismic imaging. *Geophysics*, 77(2):S43–S50.
- Berkhout, A. J. (2014a). Review paper: An outlook on the future of seismic imaging, part I: forward and reverse modelling. *Geophysical Prospecting*, 62(5):911–930.
- Berkhout, A. J. (2014b). Review paper: An outlook on the future of seismic imaging, part II: Full-wavefield migration. *Geophysical Prospecting*, 62(5):931–949.
- Berkhout, A. J. (2014c). Review paper: An outlook on the future of seismic imaging, part III: Joint migration inversion. *Geophysical Prospecting*, 62(5):950–971.

- Berkhout, A. J. and Verschuur, D. J. (1997). Estimation of multiple scattering by iterative inversion, part I: theoretical considerations. *Geophysics*, 62(5):1586–1595.
- Berkhout, A. J. and Verschuur, D. J. (2005). Removal of internal multiples with the common-focus-point (CFP) approach: Part 1 - Explanation of the theory. *Geophysics*, 70(3):V45–V60.
- Berryhill, J. R. and Kim, Y. C. (1986). Deep-water peg legs and multiples: Emulation and suppression. *Geophysics*, 51(12):2177–2184.
- Bialas, J., Klaucke, I., and Mögeltönder, J. (2013). Rv sonne fahrt-bericht/cruise report so226-chrimp chatham rise methane pockmarks, 07.01.-06.02. 2013/auckland-lyttelton, 07.02.-01.03. 2013/lyttelton-wellington.
- Billette, F. and Brandsberg-Dahl, S. (2005). The 2004 bp velocity benchmark. In *67th EAGE Conference & Exhibition*.
- Biondi, B. and Shan, G. (2002). Prestack imaging of overturned reflections by reverse time migration. *Soc. Expl. Geophys., Expanded abstracts*, pages 1284–1287.
- Bremmer, H. (1951). The WKB approximation as the first term of a geometric-optical series. *Communications on pure and applied mathematics*, 4(1):105–115.
- Broggini, F., Snieder, R., and Wapenaar, K. (2013). Data-driven Green’s function retrieval and imaging with multidimensional deconvolution: Numerical examples for reflection data with internal multiples. *SEG Technical Program Expanded Abstracts 2013*, pages 4156–4161.
- Brown, M. P. and Guitton, A. (2005). Least-squares joint imaging of multiples and primaries. *Geophysics*, 70(5):S79.
- Carcione, J. M., Herman, G. C., and Ten Kroode, A. (2002). Seismic modeling. *Geophysics*, 67(4):1304–1325.
- Claerbout, J. F. (1971). Toward a unified theory of reflector mapping. *Geophysics*, 36(3):467–481.
- Corones, J. (1975). Bremmer series that correct parabolic approximations. *Journal of Mathematical Analysis and Applications*, 50(2):361–372.
- Davydenko, M., Staal, X., and Verschuur, D. (2012). Full wavefield migration in multi-dimensional media, examples. *SEG Technical Program Expanded Abstracts 2012*, pages 1–5.
- de Bruin, C. G. M., Wapenaar, C. P. A., and Berkhout, A. J. (1990). Angle-dependent reflectivity by means of prestack migration. *Geophysics*, 55(9):1223–1234.
- De Hoop, A. T. (2008). Handbook of radiation and scattering of waves: acoustic waves in fluids, elastic waves in solids, electromagnetic waves: with corrections.

- de Hoop, M. V., Rousseau, J. H. L., and Wu, R.-S. (2000). Generalization of the phase-screen approximation for the scattering of acoustic waves. *Wave Motion*, 31(1):43 – 70.
- El-Marhoul, B. and Verschuur, D. J. (2014). 3D joint full wavefield migration of surface and vsp data. *SEG Technical Program Expanded Abstracts 2014*, pages 5070–5074.
- Fleury, C. and Snieder, R. (2012). Increasing Illumination and Sensitivity of Reverse-time Migration with Internal Multiples. *74th Annual Conference and Exhibition, EAGE, Expanded Abstracts, X042.*, pages 4–7.
- Fuchs, K. and Müller, G. (1971). Computation of synthetic seismograms with the reflectivity method and comparison with observations. *Geophysical Journal International*, 23(4):417–433.
- Gazdag, J. and Sguazzero, P. (1984). Migration of seismic data by phase shift plus interpolation. *Geophysics*, 49(2):124–131.
- Gray, S. H. (1983). On the convergence of the time-domain bremsler series. *Wave Motion*, 5(3):249 – 255.
- Grimbergen, J. L., Dessing, F. J., and Wapenaar, K. (1998). Modal expansion of one-way operators in laterally varying media. *Geophysics*, 63(3):995–1005.
- Guitton, A. (2002). Shot-profile migration of multiple reflections. *72nd Ann. Internat. Mtg.*, pages 1296–1299.
- Guitton, A. and Cambois, G. (1999). Multiple elimination using a pattern-recognition technique. *The Leading Edge*, 18(1):92–98.
- Hagedoorn, J. G. (1954). A process of seismic reflection interpretation. *Geophysical Prospecting*, 2(2):85–127.
- Jakubowicz, H. (1998). Wave equation prediction and removal of interbed multiples. pages Session:1–28.
- Kennett, B. (2009). *Seismic wave propagation in stratified media*. ANU E Press.
- Kinney, N. K., Budejicky, V., Wapenaar, C. P. A., and Berkhout, A. J. (1989). Efficient 2D and 3D shot record redatuming. *Geophys. Prosp.*, 37(5):493–530.
- Kontakis, A. and Verschuur, D. J. (2014). Deblending via sparsity-constrained inversion in the focal domain. In *76th EAGE Conference and Exhibition 2014*.
- Kutscha, H. and Verschuur, D. J. (2012). Data reconstruction via sparse double focal transformation: An overview. *Signal Processing Magazine, IEEE*, 29(4):53–60.
- Lecerf, D., Hodges, E., Lu, S., Valenciano, A., Chemingui, N., Johann, P., and Thedy, E. (2015). Imaging primaries and high-order multiples for permanent reservoir monitoring: Application to jubarte field. *The Leading Edge*, 34(7):824–828.

- Leveille, J. P., Jones, I. F., Zhou, Z.-Z., Wang, B., and Liu, F. (2011). Subsalt imaging for exploration, production, and development: A review. *Geophysics*, 76(5):WB3–WB20.
- Liner, C. L. (1991). Theory of a 2.5-d acoustic wave equation for constant density media. *Geophysics*, 56(12):2114–2117.
- Lopez, G. A. and Verschuur, D. J. (2015). Closed-loop SRME with data-reconstruction. In *77th EAGE Conference and Exhibition 2015*.
- Lu, S., Whitmore, D., Valenciano, A., and Chemingui, N. (2014a). Enhanced subsurface illumination from separated wavefield imaging. *First Break*, 32(11):87–92.
- Lu, S., Whitmore, D., Valenciano, A., and Chemingui, N. (2014b). Enhanced subsurface illumination from separated wavefield imaging. *First Break*, 32(11):87–92.
- Malcolm, A. E., Ursin, B. r., and de Hoop, M. V. (2009). Seismic imaging and illumination with internal multiples. *Geophysical Journal International*, 176(3):847–864.
- Marmalyevskyy, N., Roganov, Y., Gornyak, Z., Kostyukevych, A., and Mershchiiy, V. (2005). Migration of duplex waves. *Soc. Expl. Geophys., Expanded abstracts*, pages 2025–2028.
- Mitchell, S., Ray, C., Marc, E., Hays, D., and Craft, K. (2010). Fairfieldnodal’s excellent nodal adventure: 80th annual international meeting, seg, expanded abstracts, 740–3745.
- N. Marmalevskiy, Y. Roganov, A. K. V. R. (2007). Marmalevskiy, N., Link,. *69th Annual Conference and Exhibition, EAGE, Expanded Abstracts, P283*.
- Nemeth, T., Wu, C., and Schuster, G. T. (1999). Least-squares migration of incomplete reflection data. *Geophysics*, 64(1):208–221.
- Pacal, E. E., Stewart, R. R., Baysal, E., Yilmaz, O., et al. (2015). Seismic imaging with ocean-bottom nodes (obn): Mirror migration technique. In *2015 SEG Annual Meeting*. Society of Exploration Geophysicists.
- Petersen, K. B., Pedersen, M. S., et al. (2008). The matrix cookbook. *Technical University of Denmark*, 7:15.
- Robinson, E. A. (1957). Predictive decomposition of seismic traces. *Geophysics*, 22(4):767–778.
- Robinson, W. (1958). The need for seismic dip migration. *The Shale Shaker Digest II*, pages 297–300.
- Sacchi, M., Wang, J., and Kuehl, H. (2006). Regularized migration/inversion: New generation of seismic imaging algorithms.
- Sava, P. and Fomel, S. (2005). Riemannian wavefield extrapolation. *Geophysics*, 70(3):T45–T56.

- Sava, P. C. and Fomel, S. (2003). Angle-domain common-image gathers by wavefield continuation methods. *Geophysics*, 68(3):1065–1074.
- Schouten, J. (2012). Sparseness-constrained, least-squares migration of blended seismic data, including surface multiples. Master’s thesis, Delft University of Technology.
- Schuster, G. T. et al. (1993). Least-squares cross-well migration. In *63rd Annual International Meeting, SEG, Expanded Abstracts*, volume 12, pages 110–113.
- Staal, X., Verschuur, D., and Berkhout, A. (2014). Robust velocity estimation by joint migration inversion. In *76th EAGE Conference and Exhibition 2014*.
- Stolt, R. (1978). Migration by fourier transform. *Geophysics*, 43(1):23–48.
- Tang, Y., Biondi, B., et al. (2009). Least-squares migration/inversion of blended data. 28(1):2859–2863.
- Tarantola, A. (1987). *Inverse problem theory, methods for data fitting and model parameter estimation*. Elsevier Science Publ. Co., Inc.
- Thorbecke, J. W., Wapenaar, K., and Swinnen, G. (2004). Design of one-way wavefield extrapolation operators, using smooth functions in WLSQ optimization. *Geophysics*, 69(4):1037–1045.
- Tu, N. and Herrmann, F. J. (2015). Fast imaging with surface-related multiples by sparse inversion. *Geophysical Journal International*, 201(1):304–317.
- van den Berg, P. M., Van Broekhoven, A., and Abubakar, A. (1999). Extended contrast source inversion. *Inverse problems*, 15(5):1325.
- Van Groenestijn, G. (2010). *Estimation of primaries and multiples by sparse inversion*. TU Delft, Delft University of Technology.
- Verschuur, D. J. and Berkhout, A. J. (1994). Multiple technology, part 1: Estimation of multiple reflections. *64th Ann. Internat. Mtg.*, pages 1493–1496.
- Verschuur, D. J. and Berkhout, A. J. (1997). Estimation of multiple scattering by iterative inversion, part II: practical aspects and examples. *Geophysics*, 62(5):1596–1611.
- Verschuur, D. J. and Berkhout, A. J. (2011). Seismic migration of blended shot records with surface-related multiple scattering. *Geophysics*, 76(1):A7–A13.
- Verschuur, D. J., Berkhout, A. J., and Wapenaar, C. P. A. (1992). Adaptive surface-related multiple elimination. *Geophysics*, 57(9):1166–1177.
- Virieux, J. and Operto, S. (2009). An overview of full-waveform inversion in exploration geophysics. *Geophysics*, 74(6):WCC1–WCC26.

- Wang, J. and Sacchi, M. D. (2007). High-resolution wave-equation amplitude-variation-with-ray-parameter (AVP) imaging with sparseness constraints. *Geophysics*, 72(1):S11–S18.
- Wang, S., Chen, F., Zhang, H., Shen, Y., et al. (2013). Reflection-based full waveform inversion (rfwi) in the frequency domain.
- Wapenaar, C. (1996). One-way representations of seismic data. *Geophysical Journal International*, 127(1):178–188.
- Wapenaar, C. and Grimbergen, J. (1996). Reciprocity theorems for one-way wavefields. *Geophysical Journal International*, 127(1):169–177.
- Wapenaar, K., Broggini, F., Slob, E., and Snieder, R. (2013). Three-Dimensional Single-Sided Marchenko Inverse Scattering, Data-Driven Focusing, Green’s Function Retrieval, and their Mutual Relations. *Physical Review Letters*, 110:084301.
- Weglein, A. B., Gasparotto, F. A., Carvalho, P. M., and Stolt, R. H. (1997). An inverse scattering series method for attenuating multiples in seismic reflection data. *Geophysics*, 62:1975–1989.
- Whitmore, N. et al. (1983). Iterative depth migration by backward time propagation. In *1983 SEG Annual Meeting*. Society of Exploration Geophysicists.
- Whitmore, N. D., Valenciano, A. A., and Sollner, W. (2010). Imaging of primaries and multiples using a dual-sensor towed streamer. *Soc. Expl. Geophys., Expanded abstracts*, pages 3187–3192.
- Wong, M., Biondi, B., and Ronen, S. (2014). Imaging with multiples using least-squares reverse time migration. *The Leading Edge*, 33(9):970–976.
- Wong, M., Ronen, S., Biondi, B., et al. (2012). Joint imaging with streamer and obn data. In *2012 SEG Annual Meeting*. Society of Exploration Geophysicists.
- Xu, S. and Jin, S. (2007). An orthogonal one-return wave-equation migration. *Soc. Expl. Geophys., Expanded abstracts*, pages 2325–2329.
- Zhang, D. and Schuster, G. T. (2013). Least-squares reverse time migration of multiples. *Geophysics*, 79(1):S11–S21.
- Zhang, J. and Wapenaar, K. (2002). Wavefield extrapolation and prestack depth migration in anelastic inhomogeneous media. *Geophysical prospecting*, 50(6):629–643.
- Zhang, Y., Xu, S., and Zhang, G. (2006). Imaging complex salt bodies with turning-wave one-way wave equation. *SEG Technical Program Expanded Abstracts 2006*, pages 2323–2327.
- Zhang, Y., Zhang, G., and Bleistein, N. (2003). True amplitude wave equation migration arising from true amplitude one-way wave equations. *Inverse Problems*, 19(5):1113.

Summary

Seismic imaging aims at revealing the structural information of the subsurface using the reflected wavefields captured by sensors usually located at the surface. Wave propagation is a complex phenomenon and the measured data contain a set of back-scattered events including not only primary reflections, but also surface-related and interbed multiples. Additionally, transmission effects also play an important role in the wave propagation. However, most of the current imaging algorithms, being based on single scattering assumptions, can handle only primary reflections and all other effects are treated as noise that produces false structures (crosstalk) in the resulting image. To avoid this, data used by conventional imaging algorithms is usually preprocessed in a such way that primaries are separated from the rest of the arrivals. However, imaging only the first category of events excludes the available information contained by multiple scattering. Furthermore, as a perfect multiple removal process is a challenge, residual crosstalk is often visible in the final image.

The main topic of this thesis is to develop an imaging algorithm that can correctly handle such complex scattering effects. The main motivation is aimed at extracting complete information from the reflection data by using the multiples and, thereby, avoiding their elimination as a preprocessing step. The problem is solved by considering the imaging process as an inverse problem, where the measured data forms the data space and the unknown reflectivities constitute the model space.

Solving of the inverse problem requires forward modeling and computing the gradient. The former is based on the modelling approach where amplitudes of the modeled data are driven exclusively by the reflectivity model (to be estimated), whereas travel times are dependent only on the provided migration velocity model. Moreover, because the forward model is based on a recursive scheme (the Bremmer series) it is also possible to efficiently simulate data with any combination of multiple scattering. Therefore, by minimising the misfit between the observed and the modeled data the crosstalk from multiples in the estimated reflectivity model is suppressed, because the process of fitting the data is not based anymore on the single scattering assumption. An important component in the inversion process is extracting a model update for the reflectivities from the data misfit. It is also important to mention that complex wavefields are involved in the 'imaging condition' step, which clearly shows the contribution of the complex scattering.

Therefore, the final inversion-based imaging process is called Full Wavefield Mi-

gration (FWM) and it is especially suited for situations where primaries provide a limited illumination of the subsurface, which can be compensated by the multiples. Furthermore, extensions of the method have been proposed as well, like primary/multiple separation, source field estimation, deblending and missing data reconstruction. The virtues of FWM are successfully demonstrated on several numerical and field data examples.

Samenvatting

Seismische beeldvorming is gericht op het onthullen van structurele informatie van de ondergrond, door middel van gereflecteerde golfvelden, gemeten door sensoren die meestal aan het oppervlak zijn geplaatst. De propagatie van golven in de ondergrond is een complex fenomeen, en de gemeten data bevat verschillende soorten reflecties: primaire of enkelvoudige reflecties, maar ook oppervlak gerelateerde reflecties en meervoudige reflecties ontstaan binnen lagen onder het oppervlak. Daarnaast spelen ook transmissie effecten een belangrijke rol in de propagatie van golven. Desondanks zijn de meeste huidige algoritmen voor beeldvorming gebaseerd op de aanname van enkelvoudige verstrooiing, en kunnen alleen primaire reflecties worden verwerkt. Alle andere effecten worden behandeld als ruis, wat onechte structuren ('cross-talk') oplevert. Om dit te voorkomen wordt de gemeten data voor het toepassen van conventionele beeldvorming meestal zo voorbereid dat primaire reflecties zijn gescheiden van de rest. Maar bij het afbeelden van alleen de primaire reflecties wordt beschikbare informatie die verborgen zit in de meervoudige reflecties niet gebruikt. Bovendien, omdat een perfecte eliminatie van meervoudige reflecties een uitdaging is, zijn er vaak residuen zichtbaar in het uiteindelijke afbeeldingsresultaat.

Het hoofdonderwerp van dit proefschrift is om een beeldvorming algoritme te ontwikkelen dat correct deze complexe verstrooiingen aankan. De belangrijkste motivatie ligt in het gebruik van alle informatie van de data door ook meervoudige reflecties te gebruiken in beeldvorming, in plaats van deze te elimineren via een apart proces. Door het beeldvorming proces als een inverse probleem te beschouwen wordt dit probleem opgelost. De data die wordt gemeten vormt het datadomein en de onbekende reflectiviteit van de ondergrond vormt het modeldomein. Om het inverse probleem op te lossen moet er voorwaarts gemodelleerd worden en ook moet een gradient worden berekend. In het gebruikte voorwaartse model worden amplitudes van de gemodelleerde data bepaald door het geschatte model voor reflectiviteit en propagatietijden worden bepaald door het gegeven migratie snelheidsmodel. Omdat het voorwaartse model is gebaseerd op een recursieve reeks (de zogenaamde Bremmer reeks) is het ook mogelijk om data efficiënt te simuleren met elke combinatie van meervoudige verstrooiing. Door het minimaliseren van het verschil tussen de gemeten en gemodelleerde data wordt de cross-talk van meervoudige reflecties in het geschatte reflectiviteitsmodel onderdrukt. Een belangrijk onderdeel in het inversieproces is het berekenen van een update voor het reflectiviteit model uitgaande van het verschil tussen de gemeten en gemodelleerde data. Het is ook belangrijk om

te noemen dat complexe golfvelden worden gebruikt in de stap van ‘de imaging conditie’, dat duidelijk de bijdrage van meervoudige verstrooiing demonstreert.

Daarom wordt het uiteindelijke beeldvormingsproces, gebaseerd op inversie, ‘Full Wavefield Migration’ (FWM) genoemd, en het is vooral geschikt voor situaties waar primaire reflecties een beperkte belichting van de ondergrond bieden, welke gecompenseerd kan worden door de meervoudige reflecties. Daarnaast worden er uitbreidingen van de methode voorgesteld, zoals het scheiden van primaire/meervoudige scheiding reflecties, het schatten van het directe veld van de bron, het zogenaamde ‘deblenden’ en het reconstrueren van ontbrekende data. De gunstige eigenschappen van FWM zijn in de thesis gedemonstreerd op verschillende numerieke en echte datavoorbeelden.

Acknowledgements

I am very grateful to many people who contributed in their own way to make this thesis possible.

Firstly, I would like to thank my teachers – my supervisor Dr. D.J. Verschuur and Prof. A.J. Berkhout who also directed my progress during these years. I have learned indescribably a lot and I am very thankful for their guidance and advices they gave me and for their great school, which went far beyond the boundaries of geophysics. During these years I had a great opportunity to see the world, visit many places and meet the geophysical community during a number of EAGE and SEG conferences and workshops. Without their enthusiasm this thesis would hardly be possible. I highly appreciate their care and time spent on special FWM meetings, making better my presentations, papers, conference abstracts and this thesis. I would like to thank my teachers for a chance given to me and for many positive and helpful discussions and for the help in difficult moments. I am very grateful for that.

Additionally I would like to thank Prof. A. Gisolf for his feedback to my presentations during the dry runs. I am also grateful to Dr. Gerrit Blacquiere for the opportunity of getting to know the Delphi consortium.

I would like to thank Prof L.J. van Vliet for valuable discussions of the thesis and propositions. I highly appreciate the suggestions made by Prof. C.P.A. Wapenaar to this thesis and his useful references that helped me to solve one of the issues in this work.

I would like to acknowledge all the sponsors of the Delphi consortium for fruitful discussions as well as for their positive feedback, remarks and suggestions during the meetings and certainly for their interest in FWM.

It is important to mention a period of my studies during which I saw the professional industry at PGS offices located in Leiden and Houston. First of all, big thanks to Gert-Jan van Groenestijn for his interest and making this internship possible. It would have been difficult without professional advice from Gert-Jan van Groenestijn, Roald van Borselen and Rob Hegge and certainly colleagues from Houston: Dan Whitmore, Shaoping Lu, Alexandro Valenciano and Nizar Chemingui. I would also like to thank Rolf Baardman, Martijn Frijlink, Dorit Koenitz, Sergey Frolov and Elena Klochikhina. Furthermore I would like to thank PGS for the permission to use field data in my thesis and in various conference abstracts.

I would like to thank Dr. Gerald Eisenberg and TEEC GmbH for fruitful collaboration and permission of using the OBN field data.

I would also like to thank Dr. Ahmad Riza Ghazali and PETRONAS for a big interest in the method and I am also looking forward for further collaboration.

I would like to thank all colleagues from the research group of Acoustic Wavefield Imaging for the great work environment and for interesting joint seismic and medical imaging seminars. I would like to thank colleagues from the side of Medical Imaging: Prof. Nico de Jong, Dr. Martin Verweij, Dr. Koen van Dongen, Gerrit van Dijk, Dr. Rinus Boone, Dr. Shreyas Ranghunathan and Dr. Verva Daeichin.

I would like to thank Margaret van Fessem for the tremendous help with organizing our trips and for making very nice social events in our group and also for inviting us at home for PhD dinners.

I would like to thank Edo Bergsma and Henry den Bok for the really great help and for making the best IT environment I have ever worked with before. I also enjoyed with nice discussions.

There was a really great time with my friends and colleagues with whom I shared my PhD studies period. It was a big pleasure to be one team and have a great time inside as well as outside the university. Special thanks to Gabriel Lopez, Apostolos Kontakis, Abdulrahman Alshuhail, Ayush Garg, Bouchaib El Marhfoul, Hussain Hammad, Jan-Willem Vrolijk, Amarjeet Kumar, Sixue Wu, Aparajita Nath, Tomohide Ishiyama, Matteo Caporal, Shan Qu, Gabrio Rizzuti, Siddarth Sharma, Runhai Feng, Shogo Masaya, Xander Staal, Alok Soni, Peter Haffinger, Hannes Kutscha, Panos Doulgeris, Silvian Bendsorp, Araz Mahdad, Khalid Chougrani, Libertario Demi, Maysam Shabanimotlagh, Susanne Leinders, Neslihan Özmen and Erwin Alles. I would also like to thank Dr. Mikhail Belonosov and Dr. Jewoo Woo from Aramco Overseas who also often and greatly accompanied us.

I have also enjoyed being a daily supervisor not only by providing help to students but also learning a lot from them. Here I would like to mention Karlien Sambell, Selwyn Rosenstand and Daniel Ammeraal for their thesis and projects.

Finally a big thank you goes out to colleagues from CITG department and students from D.O.G.S. for organizing interesting geophysical talks, workshops and various events.

Также я хотел бы поблагодарить моих научных руководителей в Новосибирске В.В. Карстена и С.Б. Горшкалёва за первые знания и за вызванный интерес в области сейсморазведки.

После переезда, моя жизнь в Делфте была бы не такой яркой без моих новых друзей, с которыми меня объединил университет. Спасибо Владимиру Корзинову, Анне Кроговой, Николаю Гайко, Михаилу Белоносову, Татьяне Козловой, Татьяне Старченко, Евгении Бобковой, Марии Рудневой, Михаилу Алёхину, Наталье Втюриной, Максиму Насалевичу, Глебу Полевому.

Также, огромное спасибо моим старым друзьям из Академгородка, общение с

которыми, меня очень радовало. Спасибо Дмитрию Пещерову, Михаилу Максиму, Алексею Горбатенко, Ивану Суслову, Андрею Астафьеву, Александру Шалагинову, Александру Губину и его братьям Андрею и Петру, Михаилу Павлову, Дмитрию Перекресту и Алексею Калашникову.

Я хотел бы выразить огромную благодарность семье и передать привет всем своим родным в духе передачи Поле Чудес. Для меня все очень важны и поэтому очень хочется перечислить многих.

В первую очередь спасибо моим родителям. Мама и Папа, большое спасибо за вашу любовь и поддержку, которую я всегда ощущаю, несмотря на все расстояния. Я очень благодарен вам за всё то, что вы мне дали! Большое спасибо моей любимой сестре Наташе, которая до недавнего переезда, жила очень рядом в Германии и я всегда был рад навестить её и также провести время с моими племянницами Викторией и Софией. Спасибо её мужу Якобу за очень полезные советы. Tack sa musket, Jakob! Мне также всегда было очень радостно встретиться с моим тётями в Копенгагене. Катя и Вика, спасибо вам за регулярные встречи и за отличные выходные. Также, привет их детям, моим двоюродным братьям Максиму, Маттиасу и сестре Юле. Я также хочу передать большой привет моей любимой бабушке, с которой я бы хотел видеться намного чаще. Привет моему двоюродному брату Ивану и его родителям Зое и Анатолию Давыденко, моему дяде. Спасибо моему дедушке за очень интересные и яркие истории в его жизни, которые он навсегда оставил в моей памяти. Я был бы очень рад показать ему эту работу.

Я хочу отдельно поблагодарить мою любимую жену Александру за любовь, заботу, дружбу и поддержку, которая перевернула в лучшую сторону многое в моей жизни. Огромное спасибо, Саша!

Curriculum Vitae

Mikhail Davydenko was born in Novosibirsk, Russia on 15th of January, 1988. He studied Geophysics in Novosibirsk State University, Faculty of Geology and Geophysics, in 2005–2011. Both Bachelor and Master theses were combined with a research assistance employment in the Trofimuk Institute of Petroleum Geology and Geophysics at the Siberian Branch of the Russian Academy of Sciences.

After obtaining his Master Degree, Mikhail started his PhD studies at Delft University of Technology, Faculty of Applied Sciences, in 2011. The research was part of the Delphi consortium and involved close collaboration with oil & gas related companies. During this period Mikhail conducted research visits to PGS in Leiden and Houston. At the graduation time, 1 journal paper and 11 conference abstracts have been published.



Publications

Journal paper

- Davydenko, M., and D. J. Verschuur. Full Wavefield Migration: using surface and internal multiples in imaging. *Geophysical prospecting* (in print, 2017)

Conference abstracts

- Davydenko, M. and D. J. Verschuur. Optimal imaging of OBN data using all multiples. *SEG Technical Program Expanded Abstracts 2016*: pp. 4230-4234.
- Davydenko, M., D. J. Verschuur. "Imaging primaries, multiples or both?" 78th EAGE Conference and Exhibition 2015.
- M. Davydenko and D.J. Verschuur (2015) Full wavefield migration for sparsely sampled 3D data. *SEG Technical Program Expanded Abstracts 2015*: pp. 4206-4210.
- Davydenko, M., D. J. Verschuur, and G. J. A. van Groenestijn. "Full Wavefield Migration Applied to Field Data." 77th EAGE Conference and Exhibition 2015.
- Davydenko, M., and D. J. Verschuur. "Full wavefield migration in three dimensions." *SEG, Soc. Expl. Geophys., Expanded abstracts 2014*: 3935-3940.
- Davydenko, M., D. J. Verschuur, and A. J. Berkhout. "Omnidirectional extension of full wavefield migration." 76th EAGE Conference and Exhibition 2014.
- Davydenko, M., and D. J. Verschuur. "Full wavefield migration, using internal multiples for undershooting." *SEG Technical Program Expanded Abstracts 2013*.
- Davydenko, M., and D. J. Verschuur. "Full wavefield migration without dip limitation-using duplex waves in the Imaging with multiples." 75th EAGE Conference and Exhibition incorporating SPE EUROPEC 2013.

- Davydenko, M. V., X. R. Staal, and D. J. Verschuur. "Full wavefield migration in multi-dimensional media, examples." 2012 SEG Annual Meeting. Society of Exploration Geophysicists, 2012.
- Davydenko, M., and D. J. Verschuur. "Demonstration of full wavefield migration in 2D subsurface models." 74th EAGE Conference and Exhibition. 2012.